

Effect of Impurities on Physicochemical Properties of Nonpolar GaN Nanowires

By

AVINASH PATSHA

Enrolment No: PHYS02201004003

**Indira Gandhi Centre for Atomic Research, Kalpakkam,
Tamil Nadu, India 603102**

*A thesis submitted to the
Board of Studies in Physical Sciences
In partial fulfillment of requirements
for the Degree of*

DOCTOR OF PHILOSOPHY

of

HOMI BHABHA NATIONAL INSTITUTE

Mumbai, India



August, 2015

Homi Bhabha National Institute

Recommendations of the Viva Voce Committee

As members of the Viva Voce Committee, we certify that we have read the dissertation prepared by **Avinash Patsha** entitled “**Effect of Impurities on Physicochemical Properties of Nonpolar GaN Nanowires**” and recommend that it may be accepted as fulfilling the thesis requirement for the award of Degree of Doctor of Philosophy.

Chairman- **Dr. A. K. Tyagi**

Date:

Guide/Convener- **Dr. S. K. Dhara**

Date:

Examiner -

Date:

Member 1- **Dr. Sharat Chandra**

Date:

Member 2- **Dr. T. R. Ravindran**

Date:

Final approval and acceptance of this thesis is contingent upon the candidate's submission of the final copies of the thesis to HBNI.

I hereby certify that I have read this thesis prepared under my direction and recommend that it may be accepted as fulfilling the thesis requirement.

Date:

Place:

Dr. S. K. Dhara

(Guide)

STATEMENT BY AUTHOR

This dissertation has been submitted in partial fulfillment of requirements for an advanced degree at Homi Bhabha National Institute (HBNI) and is deposited in the Library to be made available to borrowers under rules of the HBNI.

Brief quotations from this dissertation are allowable without special permission, provided that accurate acknowledgement of source is made. Requests for permission for extended quotation from or reproduction of this manuscript in whole or in part may be granted by the Competent Authority of HBNI when in his or her judgment the proposed use of the material is in the interests of scholarship. In all other instances, however, permission must be obtained from the author.

Kalpakkam

August, 2015

(AVINASH PATSHA)

DECLARATION

I, hereby declare that the investigation presented in the thesis has been carried out by me. The work is original and has not been submitted earlier as a whole or in part for a degree / diploma at this or any other Institution / University.

Kalpakkam

August, 2015

(AVINASH PATSHA)

List of Publications Arising from the Thesis

1. “Localized Charge Transfer Process and Surface Band Bending in Methane Sensing by GaN Nanowires”, **Avinash Patsha**, P. Sahoo, S. AmirthaPandian, A. K. Prasad, A. Das, A. K. Tyagi, Monica A. Cotta, S. Dhara, *J. Phys. Chem. C*, **2015**, *119*, 21251-21260.
2. “Localized Tip Enhanced Raman Spectroscopic Study of Impurity Incorporated Single GaN Nanowire in the Sub-Diffraction Limit”, **Avinash Patsha**, S. Dhara, A.K. Tyagi, *Appl. Phys. Lett.*, **2015**, *107*, 123108-4.
3. “Nonpolar *p*-GaN/*n*-Si Heterojunction Diode Characteristics: A Comparison between Ensemble and Single Nanowire Devices”, **Avinash Patsha**, R. Pandian, S. Dhara, and A. K. Tyagi, *J. Phys. D: Appl. Phys.*, **2015**, *48*, 395102-7.
4. “Direct Evidence of Mg Incorporation Pathway in Vapor–Liquid–Solid Grown *p*-type Nonpolar GaN Nanowires”, **Avinash Patsha**, S. Amirthapandian, R. Pandian, S. Bera, A. Bhattacharya, S. Dhara, *J. Phys. Chem. C*, **2014**, *118*, 24165-24172.
5. “Influence of Oxygen in Architecting Large Scale Nonpolar GaN Nanowires”, **Avinash Patsha**, S. Amirthapandian, R. Pandian, S. Dhara, *J. Mater. Chem. C*, **2013**, *1*, 8086-8093.
6. “Probing Crystallographic Orientation of a Single GaN Nanotube Using Polarized Raman Imaging”, **Avinash Patsha**, P. Sahoo, S. Dhara, S. Amirthapandian, A.K. Tyagi, *J. Raman Spectrosc.* **2013**, *44*, 651-654.
7. “Raman Spectral Mapping of III–V Nitride and Graphene Nanostructures”, **Avinash Patsha**, K. K. Madapu, S. Dhara, *MAPAN-JMSI*, **2013**, *28*, 279-283.
8. “Raman Imaging on High-Quality Graphene Grown by Hot-Filament Chemical Vapor Deposition”, S. Kataria, **Avinash Patsha**, S. Dhara, A.K. Tyagi, H.C. Barshilia, *J. Raman Spectrosc.* **2012**, *43*, 1864-1867.

Communicated/ in preparation

9. “Modulation of Interband Transitions as Intense Source of Light in Nonopolar GaN Nanowire Optical Waveguide”, **Avinash Patsha**, S. Dhara, *Optt. Lett.*, **2015** (*Under Review*).

10. “Optoelectronic properties of single and array of 1-D III-nitride nanostructures: An approach to light-driven device and energy resourcing”(Invited Review Article), **Avinash Patsha**, S. Dhara, A. K. Tyagi, S. Chattopadhyay, K. H. Chen, L. C. Chen, *Prog. Mater. Sci. (In Preparation)*.

Conference Proceedings:

1. “Optical Properties of Mg Doped *p*-type GaN Nanowires”, **Avinash Patsha**, R.Pandian, S. Dhara and A.K. Tyagi, *AIP Conf. Proc.*, **2014**, 1665, 050051 1-2.
2. “Self-catalyzed Anisotropic Growth of GaN Spirals”, **Avinash Patsha**, P. Sahoo, S. Dhara, and A. K. Tyagi, *AIP Conf. Proc.*, **2012**, 1447, 1289-1290.
3. Growth of GaN Nanostructures on Graphene”, **Avinash Patsha**, P. Sahoo, Kishore K. Madapu, S. Dhara, and A. K. Tyagi, *IEEE Xplore, Proc.*, **2011**, p. 553-555.

Conference Presentations:

1. “Nonpolar GaN Nanowire as Optical Waveguide and Photodetector”, **Avinash Patsha**, S. Dhara, A. K. Tyagi, *DAE-BRNS National Conference on Current Trends in Advanced Materials (CTMAT, November 19-21, 2014)* Kolkata, India.
2. “Single GaN Nanowire Field Effect Transistor: Surface Architecture Dependent Transport and Sensory Properties”, **Avinash Patsha**, R. Pandian and S. Dhara, *International Conference on Nano Science and Technology (ICONSAT, March 3-5, 2014)* Chandigarh, India.
3. “Influence of Oxygen on Group III Nitride Nanowires” (*Contributory Presentation*), **Avinash Patsha**, S. Amirthapandian, R. Pandian, and S. Dhara, *International Union of Material Research Society – International Conference in Asia (IUMRS-ICS, December 16-20, 2013)* Bangalore, India.
4. “Raman Imaging of Single Nanostructures: Vision with Spectral Eye” (*Invited Talk*) **Avinash Patsha**, *India-Brazil-South Africa Nanotechnology (IBSA, March 17-21, 2013)*, South Africa.
5. “1-D GaN Nanostructures for Sensor Applications”, **Avinash Patsha**, *Indo-South Africa workshop on Green Chemistry (March 23-24, 2013)*, South Africa.

6. "Tuning Size and Morphology of GaN Nanowires", **Avinash Patsha**, S. Dhara, R. Pandian and S. Amirthapandian, *Materials Research Society of India-AGM (MRSI-AGM, January 11-15, 2013)*, Kalpakkam, India.
7. "Probing Crystallographic Orientation of GaN Nanotube by Polarized Raman Spectroscopy", **Avinash Patsha**, P. Sahoo, S. Dhara and A. K. Tyagi, *International Conference on Raman Spectroscopy (August 12-17, 2012)*, Bangalore, India.

Other Publications (Not Included in the Thesis):

1. "Optical Properties of Monodispersed AlGaIn Nanowires in the Single-Prong Growth Mechanism" A. K. Sivadasan, **Avinash Patsha**, S. Polaki, S. Amirthapandian, S. Dhara, A. Bhattacharya, B.K. Panigrahi, A.K. Tyagi, *Cryst. Growth Des.*, **2015**, *15*,1311-1318.
2. "Optically Confined Polarized Resonance Raman studies in Identifying Crystalline Orientation of Sub-Diffraction Limited AlGaIn Nanostructure", A. K. Sivadasan, **Avinash Patsha**, S. Dhara, *Appl. Phys. Lett.*, **2015**, *106*, 173107 1-4.
3. "Effect of substrate heating and microwave attenuation on the catalyst free growth and field emission of carbon nanotubes", R. Kar, S. Sarkar, C. Basak, **Avinash Patsha**, S. Dhara, C. Ghosh, D. Ramachandran, N. Chand, S. Chopade, D. Patil, *Carbon* **2015**, *94*, 256-265.
4. "Catalysis Free Growth of GaN Nanostructures", P. Sahoo, S. Dhara, **Avinash Patsha**, S. Dash, M. Kamruddin, and A. K. Tyagi, *AIP Conf. Proc.*, **2012**, *1447*, 449-450.

Kalpakkam

August, 2015

(AVINASH PATSHA)

Dedicated to

My Parents, Teachers, Friends

&

Life on the Earth

ACKNOWLEDGEMENTS

It would not have been possible for me to prepare my doctoral thesis without the help and support of a number of wonderful people, who shaped my ideas and helped in my research during the tenure of Doctor of Philosophy.

I am immensely indebted to my research supervisor Dr Sandip K. Dhara for the stimulating discussions, constructive criticisms, and tutelage that put me always on my toes. The passion for fine research kindled by him would be commemorated forever.

I would like to thank the former directors of Indira Gandhi Centre for Atomic Research, Dr. Baldev Raj and Shri. S. C. Chetal and the present Director, Dr. P. R. Vasudeva Rao for allowing me to pursue research work at IGCAR. I thank the former and present directors of Materials Science Group for facilitating the research activities. I am grateful to Dr. M. Sai Baba, the Associate Director, RMG, IGCAR for his support and facilitating a nice and enjoyable stay in JRF enclave. I also thank the Department of Atomic Energy for financial aid to carryout my research work.

My sincere thanks to the doctoral committee chairman Dr. A.K. Tyagi and members Dr. Sharat Chandra, and Dr. T. R. Ravindran for the time to time evaluation, constant encouragement and useful suggestions throughout my research work. I convey my deep gratitude to our coloborators Dr. S. Amirthapandian, Dr. Ramanathaswamy Pandian, Dr. Santanu Bera of IGCAR, Prof. Neil Coville, Univ. of Witwatersrand, South Africa and Prof. Monica A. Cotta, Univ. of Campinas, Brazil for their expertise contribution and discussions towards my research work. I would like to thank the reviewers of my manuscripts for their valuable comments and suggestions which helped in fine tuning the ideas for my research.

I deeply express my heartfull thanks to all of my seniors and colleagues Dr. A. Das, Dr. A.K. Prasad, Mr. M. Kishore Kumar, Mr. B.V. Ramana, Mr. Subrata Ghosh, Mr. A.K. Sivadasan, Mr. S. Parida for the valuable discussions and sharing our scientific adventures. I owe a big thanks to my heartfelt senior Dr. Prasana Kumar Sahoo for his memorable companionship and sharing phylosophical thoughts, in the early stage of my research career.

I owe a deep gratitude to my parents Satyanarayana and Nagalakashmi, elder brother Vinay Kumar, younger sister Sindhuri and all friends of my career for their adoration, afiinity, and inspiration which drive me throught my journey of life.

CONTENTS

	Page No.
SYNOPSIS	i
LIST OF FIGURES	vi
LIST OF TABLES	xii
LIST OF ABBREVIATIONS	xii
CHAPTER 1 INTRODUCTION	
1.1 Group-III Nitrides	1
1.1.1 Gallium Nitride (GaN)	1
1.1.2 Polar and Nonpolar Surfaces	2
1.1.3 Polarization Effects	2
1.1.4 Properties and Applications	3
1.1.5 The Issues in Growth, Property and Applications of GaN	4
1.2 GaN Nanowires	5
1.3 Nanowire Growth	6
1.3.1 Vapor-Liquid-Solid (VLS) Process	7
1.3.2 Vapor-Solid (VS) Process	8
1.4 Impurities in GaN	8
1.4.1 Intentional and Unintentional Impurities	8
1.4.2 Impurity Incorporation Pathways in GaN Nanowires	9
1.5 Role of Impurities in Properties and Devices of GaN	10
1.6 Motivation of the Thesis	12
1.7 Objective and Over View of the Thesis	13
1.8 References	16
CHAPTER 2 EXPERIMENTAL TECHNIQUES	
2.1 Introduction	20
2.2 Growth Techniques	20
2.2.1 Vacuum Thermal Evaporation System	20
2.2.2 Atmospheric Pressure Chemical Vapor Deposition (APCVD) System	22

2.3	Morphological Characterization	24
2.3.1	Field-Emission Scanning Electron Microscope (FESEM)	24
2.4	Structural and Elemental Characterization	25
2.4.1	Transmission Electron Microscope (TEM)	25
2.4.2	Electron Energy Loss Spectroscopy (EELS) and Energy Filtered TEM (EFTEM)	27
2.4.3	X-Ray Photoelectron Spectroscopy (XPS)	29
2.5	Optical Characterization	30
2.5.1	Raman Spectroscopy	30
2.5.2	Photoluminescence Spectroscopy (PL)	33
2.6	Electrical Characterization	34
2.6.1	Dual-Beam (Electron and Focused Ion Beam) Deposition System	34
2.6.2	Electrical Probe Station and Source-Measurement Units	36
2.7	Scanning Probe Microscope Coupled with Light	37
2.7.1	Atomic Force Microscopy (AFM)	37
2.7.2	Scanning Kelvin Probe Microscopy (SKPM)	38
2.7.3	Tip-Enhanced Raman Spectroscopy (TERS)	40
2.8	Exposure Facility for Gas Sensor Testing System (EFGS)	41
2.9	Summary	42
2.10	References	43

CHAPTER 3 EFFECT OF OXYGEN IMPURITY ON MORPHOLOGICAL, STRUCTURAL AND OPTICAL CHARACTERISTICS OF NONPOLAR GaN NANOWIRES

3.1	Introduction	44
3.2	Growth of GaN Nanowires in the VLS Process Using APCVD	47
3.2.1	Tuning the Au Catalyst Particle Size and Shape	47
3.2.2	Optimized Parameters for Growth of GaN Nanowires	51
3.2.3	Role of Substrate	52
3.3	Influence of Oxygen Impurity on GaN Nanowires	55
3.3.1	Morphological Variations	55
3.3.2	Structural and Compositional Variations	58

3.4	Optical Characteristics	64
3.4.1	Raman Spectroscopic Study	64
3.4.2	Photoluminescence Study	67
3.5	Waveguide Property	69
3.6	Summary	70
3.7	References	71
CHAPTER 4	EFFECT OF Mg DOPING ON NONPOLAR GaN NANOWIRES	
4.1	Introduction	73
4.2	Growth of Mg Doped GaN Nanowires in VLS Process Using APCVD	75
4.3	Study on Dopant Pathway in VLS Grown Mg Doped GaN Nanowires	76
4.3.1	Morphological Study	76
4.3.2	Compositional and Structural Study	77
4.3.3	Dopant Pathway study	80
4.4	Optical Properties	84
4.4.1	Raman Spectroscopic Study	84
4.4.2	Photoluminescence Study	86
4.5	Summary	90
4.6	References	91
CHAPTER 5	ROLE OF OXYGEN IMPURITY ON GAS SENSING PROPERTIES OF GaN NANOWIRES	
5.1	Introduction	94
5.2	Nanowires Synthesis and Characterization	96
5.2.1	Nanowire Synthesis	96
5.2.2	Morphological and Structural Characteristics	96
5.3	Oxygen Defects Analysis by EELS Studies: Experiment and Simulation	99
5.4	Nanowires Device Fabrication, Electrical and Gas Sensing properties	102
5.4.1	Device Fabrication	102
5.4.2	Current–Voltage (<i>I-V</i>) Characteristics	102
5.4.3	Gas Sensing Properties	103

5.5	SKPM Studies on Nanowires	106
5.5.1	Surface Potential Measurements of As-Grown Nanowires	106
5.5.2	<i>in situ</i> SKPM Measurements Under Gas Exposure	109
5.6	Charge Transfer and Surface Band Bending in Gas Sensing	116
5.7	Summary	117
5.8	References	119
CHAPTER 6 ROLE OF Mg DOPANTS IN PHOTORESPONSE OF <i>p</i>-GaN NANOWIRES		
6.1	Introduction	122
6.2	Nanowire Synthesis, Characterization and Device Fabrication of Ensemble and Single <i>p</i> -GaN Nanowire and their Heterojunctions with <i>n</i> -Si	123
6.2.1	Mg Doped <i>p</i> -GaN Nanowires Synthesis	123
6.2.2	Morphological and Photoluminescence Characterizations of <i>p</i> -GaN Nanowires	124
6.2.3	Ensemble and Single Nanowire Device Fabrication	125
6.3	Electrical Characteristics of Nanowire Devices	127
6.3.1	Electrodes to <i>n</i> -Si, Ensemble and Single <i>P</i> -GaN Nanowire	127
6.3.2	Ensemble <i>p</i> -GaN NW/ <i>n</i> -Si Heterojunction Device	128
6.3.3	Single <i>p</i> -GaN NW/ <i>n</i> -Si Heterojunction Device	130
6.4	Photoresponse Properties of Nanowire Devices	132
6.4.1	Photodiode Characteristics of Ensemble <i>p</i> -GaN NW/ <i>n</i> -Si Heterojunction Device	132
6.4.2	Photodiode Characteristics of Single <i>p</i> -GaN NW/ <i>n</i> -Si Heterojunction Device	134
6.5	Summary	136
6.6	References	137
CHAPTER 7 BRIEF SUMMARY OF THESIS AND SCOPE FOR FUTURE WORK		
		139

SYNOPSIS

Gallium nitride (GaN) based Group-III nitride nanowires (NWs) have emerged as potential building blocks for nanoscale electronic and optoelectronic devices such as light emitting diodes (LEDs), lasers, high electron mobility transistors (HEMTs), logic gates, photodetectors, solar cells and gas sensors. Apart from the usual advantages of being 1-D nanostructure with large surface-to-volume ratio, ultra high aspect ratio, ease in the electrical contact formation and unidirectional conduction channels, reduction of extended defects like dislocations is the vital advantage in case of GaN. Controlled diameter and surface architecture of GaN NWs play crucial role in defining physicochemical properties for large scale production of the devices. In the conventional polar GaN (*c*-axis oriented), strain induced piezoelectric and spontaneous polarizations have intense effects on device structures such as LEDs and photodetectors. Whereas, the nonpolar GaN (*m*-axis and *a*-axis oriented) have attracted intense research interest due to the absence of polarization induced electric fields. The objective of the present thesis is to understand the effects of intentional (Mg) and unintentional (O) impurities on the physicochemical properties in consequences of variations in size, surface morphology, and structure of nonpolar GaN NWs.

The effects of dopants and impurities either on the defect formation or on the evolution of surface morphology are critical issues in the device performance and have been well studied in the case of thin films of GaN samples. While a material is scaled down to nano-dimensions, particularly in a bottom-up approach, it is vital to preserve the surface architecture of nanostructures in the entire sample. The most studied ubiquitous inevitable impurity in III- nitrides is oxygen which impoverishes the nitride phase and alters the electrical, optical and electromechanical properties. The degree of oxygen contamination depends on the growth technique. However, the extent over which unintentional

incorporation of oxygen affects the GaN NWs is unexplored. This thesis reports the effect of oxygen impurity on morphological, structural and optical characteristics of nonpolar GaN NWs grown in the atmospheric pressure chemical vapor deposition (APCVD) technique.

The functionality of nanoscale electronic and optoelectronic devices made of compound semiconductor NWs like III-nitrides relies on the complex process of doping. Doping of III-nitride NWs, in particular *p*-type doping, is a difficult process compared to that for the thin films, as the dopant incorporation and distribution depend on N/III ratio and incorporation pathways, respectively. Depending on the dopant type and growth technique the incorporation pathways can alter in NWs. Understanding of the dopant incorporation pathway in NWs can help in tuning the dopant distribution over a precise location along the NW which is crucial for aforementioned NW devices. Mg is the most successful *p*-dopant in III-nitrides, which paves the way for realizing III-nitride based electronic and optoelectronic devices. Optimization of Mg doping in GaN is also a necessary and challenging process owing to the issues concerning low hole density, pyramidal defects, and stacking faults. This thesis reports the study on Mg dopant incorporation pathways in *p*-GaN NWs and the structural and optical characteristics of the doped NWs.

Understanding the physicochemical processes at the surfaces of semiconductor nanostructures is of paramount importance for developing nanostructures based energy and sensor devices. The key physical and chemical processes involved in the aforementioned device operations are absorption of photons or adsorption of gaseous molecules, charge transfer and charge transport on semiconductor surfaces. However, owing to the high surface to volume ratio in nanostructures, complex behavior of semiconducting surfaces strongly influences the above three fundamental processes and alters the device performances. The active sites responsible for charge transfer on the surface can be governed by intrinsic and extrinsic defects in semiconductors, metal-semiconductor Schottky junctions or some

functional groups attached to the surface. Thermally stable and chemically inert pure nitride semiconducting surfaces (such as GaN and AlGaN) utilize the Schottky junction with metal or heterojunctions with other semiconducting surfaces as active sites in the sensing process. Extensive studies on unintentional oxygen impurity in III-nitrides showed a strong influence of surface oxides on the sensing parameters of nitride devices. However, the underlying mechanism has not been well understood. Detailed studies conducted on the role of oxygen impurity on gas sensing properties of nonpolar GaN NWs are reported in this thesis with possible mechanisms involved in sensing process.

Combining with other III-nitrides, GaN-based single and ensemble NW photoconductors and photodiodes paved the way for realizing photoresponse for wide wavelength range. Besides, the absence of polarization-related electric fields in nonpolar III- nitride based nanostructures provides a wider range of absorption wavelengths along with higher absorption probability compared to polar components. Further improvements on the functionalities of the NW devices can be achieved by forming heterojunctions with other electronic and optoelectronic materials. However, electrical and optical characteristics of such heterojunction devices can be influenced by several device processing parameters which enhance the complexity of integration. Integration of GaN with Si is carried out by forming Mg doped *p*-GaN NW/*n*-Si heterojunctions and the results are reported in this thesis. Role of Mg dopants on the electrical and the photoresponse characteristics of *p*-GaN NW devices and their heterojunctions with *n*-Si are studied.

The thesis is organized in to seven chapters and the contents of each chapter are outlined as follows,

The Chapter 1 gives a brief introduction about GaN, impurities and their role in GaN growth, properties and device performances. The NW growth processes and applications of GaN NWs are briefed. The Chapter 2 briefly describes the principle and basic parts of the

experimental techniques used for growth and characterization of GaN NWs studied in the present thesis work.

In the Chapter 3, general growth process of GaN NWs carried out using APCVD technique in the vapor-liquid-solid (VLS) process and the optimized growth parameters including tuning of the catalyst particle's size and the role of substrate are discussed. The effect of unintentional incorporation of oxygen on the nonpolar GaN NWs is investigated with the possible mechanism. NW size, surface morphology, growth rate and the reproducibility are strongly affected by oxygen impurity. The study showed that the excessive incorporation of oxygen into the GaN during the NW synthesis could lead to the uncontrollable growth rate and inhomogeneous surface morphologies of NWs having nonuniform sizes. Size-selective growth of uniform morphology of GaN NWs is achieved, in the oxygen reduced condition, using different catalyst sizes. The structural and the optical characteristics including Raman scattering and photoluminescence (PL) studies along with waveguide properties of the NWs are reported in this chapter. The study showed that the crystalline and optical qualities are devastated for the oxygen rich GaN NWs.

Detailed growth process of Mg doped GaN NWs using the CVD technique via VLS process is discussed in the Chapter 4. Effect of Mg dopants at the liquid/solid interface (Au-Ga/GaN) is studied in the axial growth of GaN NWs to find the pathway of the Mg incorporation. Morphological and structural studies showed the profound effects on Mg doped GaN NWs. Mg incorporation is confirmed using X-ray and electron spectroscopy measurements along with localized tip enhanced Raman spectroscopy study on single NWs. Transmission electron microscopic studies are used for finding the Mg incorporation pathway in the GaN NWs. The Study shows the direct evidence of incorporation of the Mg atoms through the Au-Ga/GaN interface. Local distortion and twining of atomic planes between catalyst particle and the NW confirm the interface as Mg incorporation pathway. The PL

studies on different concentrations of Mg doped GaN NWs confirm the activation of Mg atoms as *p*-type dopants in nonpolar GaN NWs.

Role of oxygen defect complexes in nonpolar GaN NWs on methane (CH₄) sensing is reported in chapter 5. Experimental and DFT based simulations of EELS studies are performed to understand the type of possible oxygen defects present in the NWs. The EELS studies on oxygen rich GaN NWs confirmed the possible presence of 2(O_N) and V_{Ga}-3O_N defect complexes. A global resistive response for sensor devices of ensemble NWs and a localized charge transfer process in single GaN NWs by *in situ* scanning Kelvin probe microscopy (SKPM) are studied towards CH₄ sensing. A localized charge transfer process, involving V_{Ga}-3O_N defect complex on NW surface is attributed to controlling the global gas sensing behavior of the oxygen rich ensemble GaN NWs.

Device fabrication of ensemble and single *p*-GaN NW and their heterojunctions with *n*-Si are discussed in the Chapter 6. Electrical and photoresponse characteristics of the individual *p*-GaN NW devices and heterojunction devices with *n*-Si are studied. Photovoltaic and photoconducting mode characteristics of the heterojunction devices are analyzed and the key parameters including ideality factors, fill factors and responsivity of ensemble and single *p*-GaN NW/*n*-Si heterojunction devices are estimated and compared. The study showed that the presence of defect states due to deep-levels and inhomogeneity in Mg dopants in *p*-GaN NWs enhanced the ideality factor of the ensemble *p*-GaN NW/*n*-Si device. Photovoltaic mode of ensemble NW device showed an improvement in the fill-factors up to 60 % over the single NW device with fill-factors up to 30 %. The enhanced photoresponse of the single NW device also confirmed the photoconduction due to the presence of sub-bandgap states in *p*-GaN NWs.

The Chapter 7 summarizes the major findings of the studies on GaN NWs carried out and the directions for future work.

LIST OF FIGURES

Figure No.	Title of the Figure	Page No.
1.1	(a) Schematic view of the wurtzite GaN structure and (b) different crystallographic planes.	1
1.2	Schematic view of the vapor-liquid-solid process.	7
1.3	Schematic view of the different types of impurity incorporation pathways during the VLS process shown by dotted arrows.	10
1.4	(a) Schematic view of intrinsic and extrinsic optical transitions in GaN. (b) Radiative transitions associated with major impurities in GaN.	11
2.1	Schematic view of the vacuum thermal evaporation system.	22
2.2	Schematic view of the APCVD system used for growth of GaN NWs.	23
2.3	(a) Schematic view of the several interactions occurs in a material due to the incidence of high energy electron beam. (b) Block diagram of a FESEM showing the major parts of the system.	25
2.4	Ray-diagram of a TEM showing the diffraction mode operation (left side) and standard imaging mode operation (right side) with the major components of the system.	26
2.5	(a) Ray-diagram of a magnetic prism in a plane perpendicular to the magnetic field. Solid lines represent zero-loss electrons ($E = 0$); dashed lines represent those have lost energy during transmission through the specimen. (b) Block diagram of a TEM-EELS system having in-column second order corrected omega energy filter.	28
2.6	(a) Schematic view of the X-ray induced photoelectron emission process. (b) Block diagram of the XPS setup with major components.	30
2.7	Schematic view of the elastic and inelastic processes in a material with incidence of light.	31
2.8	Block diagram of the Raman setup with major parts, used for the present studies.	32
2.9	Schematic view of the PL process in a direct bandgap semiconductor.	33
2.10	(a) Block diagram of the FIB column. (b) Schematic view of the dual-beam deposition system.	36
2.11	(a) Interaction force Vs distance between tip and sample. (b) Block diagram of general SPM system with major components.	37
2.12	(a) The schematic view of the energy level diagrams of the tip and sample surface, when they are separated, electrically contacted and in biasing condition. (b) Block diagram of the SKPM setup.	39
2.13	The block diagram of the exposure facility for gas sensor (EFGS) testing system.	42
3.1	FESEM micrograph of GaN spirals grown in the VS process on alumina boat. Inset shows the magnified image of a single spiral of diameter $\sim 20 \mu\text{m}$ and a single sphere of GaN.	45
3.2	FESEM micrographs of GaN nanostructures grown in the VS process on	46

	the substrates (a) mechanically exfoliated FLG template from HOPG transferred on to SiO ₂ , (b)-(d) GaN nanostructures grown on COOH-functionalized FLG powder dispersed on SiO ₂ substrates. Inset shows the magnified images of the nanostructures.	
3.3	Effect of annealing process: an Au film of recorded thickness 1 nm on Si substrate (a) before and (b) after annealing at 900 °C for 15 min.	49
3.4	Effect of annealing temperature: an Au film of recorded thickness 2 nm on Si substrate annealed for 15 min at temperatures (a) 800 °C and (b) 900 °C.	49
3.5	Dependence of annealing time on film thickness: an Au film of recorded thickness 5 nm on Si substrate annealed at temperatures 900 °C for (a) 15 min and (b) 30 min.	50
3.6	FESEM micrographs of Au nanoparticles of different sizes (a) 20(±5) nm (b) 30(±5) nm, (c) 55(+10) nm, and d) 105(+40) nm.	50
3.7	Temperature Vs time plot for the VLS growth of GaN NWs.	51
3.8	FESEM micrographs of GaN NWs of sizes (a) 40(±5) nm, and (b) 60(±5) nm grown under optimized growth parameters in the VLS process. Insets show the high magnification micrographs of GaN NWs with catalyst particles (doted circles) at the tips of NWs.	52
3.9	FESEM micrographs at 54° tilt view of GaN NWs grown on substrates (a) Si(100), and (b) Si(111). Insets show the high magnification micrographs of triangular shaped GaN NWs with catalyst particles at the tips.	53
3.10	FESEM micrographs of GaN NWs grown on substrates (a) <i>c</i> -Al ₂ O ₃ , and (b) AlN(60nm)/Si(111). Insets show the high magnification micrographs of triangular shaped GaN NWs with catalyst particles at the tips.	53
3.11	FESEM micrographs of GaN NWs grown on substrates (a) Graphene/SiO ₂ (300nm)/Si, and (b) SiO ₂ (300nm)/Si. Insets show the high magnification micrographs of triangular shaped GaN NWs with catalyst particles at the tips.	54
3.12	Typical FESEM images of GaN NWs. (a and b) NWs of sample R1 showing (insets) quite rough and nonuniform surface morphology in the respective high magnification images. (c) NWs of sample R2 shows smooth but nonuniform morphology in the respective high magnification image. (d) NWs of sample R3 having uniform diameter and surface morphology along the wire shown in the high magnification image (inset). Inset, nanoparticles at the tip of the NWs are clearly seen.	56
3.13	Typical FESEM images of GaN NWs grown in oxygen reduced conditions (sample R4). Inset shows the high magnification image of NWs with uniform shape, surface morphology and size distribution of 55(±5) nm.	57
3.14	Typical NW grown in O rich condition (sample R1) shows (a) an irregular surface morphology. FFT diffraction spots corresponding to the TEM micrograph (outset) reveal the presence of phases of GaN and Ga ₂ O ₃ . (b and c) HRTEM images of NWs. (d) A typical NW grown in O reduced conditions (sample R2) with SAED pattern (outset), indexed to wurtzite GaN of the zone axis along [0001]. (e and f) HRTEM image of the NW (Fig. 3.14d) having nonpolar planes (10 $\bar{1}$ 0) and the growth direction along [11 $\bar{2}$ 0].	58
3.15	(a) Low magnification TEM micrograph of a typical GaN NW grown in oxygen reduced conditions (sample R3). (b) SAED pattern of the NW, indexed to wurtzite GaN with zone axis along [0001]. (c) HRTEM image	60

	collected near the tip of the NW having Au nanoparticle. (d) Magnified view of the HRTEM image shows the NW having nonpolar planes (10 $\bar{1}$ 0) and the growth direction along [11 $\bar{2}$ 0].	
3.16	Schematic view of the possible O incorporation pathways, along with Ga and N during the VLS growth of GaN NW.	61
3.17	EELS spectra of GaN NWs of the samples R1 and R2, R3 grown in O rich and O reduced conditions, respectively. (a) Background subtracted N- <i>k</i> edge of NWs. (b) Corresponding O- <i>k</i> edge of NWs of the samples R1, R2 and R3.	62
3.18	(a) EELS spectra of background subtracted <i>K</i> -edges of N and O obtained from the position 1 (middle region of the NW with thin and rough morphology) and position 2 (tip region of the NW with thick and rough morphology) on the NW of the sample R1 grown in O rich conditions. (b) EELS spectra of background subtracted <i>K</i> -edges of N and O obtained from the position 1 (middle region of the NW) and position 2 (close to one end of the NW) on the NW of the sample R3 grown in O reduced conditions.	63
3.19	(a) Schematic view of the atomic vibrations in wurtzite GaN for zone centre phonons. ^[21] Arrow marks indicate the direction of vibrations. (b) A typical Raman spectrum of single GaN NW of sample R3 with low O concentration. Inset shows the optical image of a single NW (encircled) on Cu(100) substrate (c) Raman spectra of ensemble and a single GaN NW of O rich sample R1. (d) TERS spectra of a single GaN NW of sample R1 with and without TERS tip. AFM image of the NW is shown in the inset. The peak pointed out by star mark (*) corresponds to GaO _x N _y phase.	66
3.20	Typical PL spectra of GaN NWs of the samples R1, R2 and R3, collected in the energy range 2.0 - 3.8 eV, at 80 K.	68
3.21	Typical optical images of far field bright violet emission spots at 300 and 80 K on the NWs of sample (a) R3 and (b) R4. Emission spots are coming out of the ends of the NWs through the available open space while other ends are at the excitation with laser light.	69
4.1	Schematic representation of the proposed bond center and anti-bonding site incorporation of H in GaN and its passivation of Mg during growth of GaN.	74
4.2	Typical FESEM images of GaN NWs. (a) Undoped NWs having uniform diameter along with the Au catalyst particle (encircled) at the tip of the wire (inset). (b) GaN:Mg-I and (c) GaN:Mg-II are Mg doped GaN NWs. The sample GaN:Mg-I is less doped compared to that of the sample GaN:Mg-II. All the NWs are grown with Au catalyst particle (encircled) at the tip (insets b, c).	76
4.3	XPS spectra from Mg doped GaN NWs of the samples GaN:Mg-I and GaN:Mg-II: (a) Ga 3 <i>d</i> (b) N 1 <i>s</i> and (c) Ga 2 <i>s</i> + Mg 1 <i>s</i> . Ga 2 <i>s</i> peak recorded from undoped sample is plotted in (c) for comparison. Solid lines are experimental data, and discontinuous lines are fitted data.	77
4.4	(a) Low magnification TEM image of a typical undoped GaN NW. SAED pattern of the NW, indexed to wurtzite GaN with zone axis along [0001]. HRTEM collected near the tip of the NW having growth direction along [10 $\bar{1}$ 0] and a sharp interface between Au and GaN is seen (inset). (b) GaN NW doped with Mg (GaN:Mg-I). SAED of the NW collected along the zone axis [01 $\bar{1}$ 0] of wurtzite phase. An interface separating the NW and	79

	distorted portion of the tip region with Au nanoparticle is seen in HRTEM. Inset shows the contrast variation in the tip region. (c) GaN NW doped with increased Mg concentration (GaN:Mg-II). SAED pattern of the NW collected along the zone axis $[01\bar{1}0]$ of wurtzite phase. Clear interface is visible in the HRTEM collected near the tip region and NW having growth direction along $[10\bar{1}0]$. Inset shows lattice fringes of $(10\bar{1}0)$ planes at the interface.	
4.5	Typical EELS spectra corresponding to (a) N <i>K</i> -edge collected from the NWs of three samples, and Mg <i>K</i> -edges collected from single GaN NWs of Mg doped samples (b) GaN:Mg-I and (c) GaN:Mg-II. Comparison of EELS spectra corresponding to (d) Ga- <i>L</i> edge and (e) Mg- <i>K</i> edges collected from single GaN NWs of the undoped and Mg doped sample (top). Mg- <i>K</i> edge is also compared with that of MgO reference sample (bottom) showing similar fine feature as observed in the Mg doped GaN NWs.	81
4.6	EFTEM micrographs generated from the NW for each Mg doped sample (a) GaN:Mg-I and (b) GaN:Mg-II correspond to zero-loss energy (grey color), Ga- <i>L</i> (red color), N- <i>K</i> (green color) and Mg- <i>K</i> (yellow color). These are pseudocolors chosen for describing presence of different elemental species in the NW.	82
4.7	(a) EFTEM micrographs collected from the undoped NW (b) Comparison of the EFTEM micrographs generated from the Mg <i>K</i> -edge region, collected from doped and undoped NWs. Au catalyst particle appears dark in the doped NW in the absence of Mg at the tip. Whereas in case of undoped sample, uniform contrast is observed including the catalyst particle due to the extended features of Ga <i>L</i> -edge. (c) Schematic view of the incorporation pathways of different elements during the VLS growth of NW.	83
4.8	(a) Typical Raman spectra of ensemble and single GaN NW of sample GaN:Mg-II (b) AFM images of single NW of undoped and doped (GaN:Mg-II) samples. TERS spectra of a single NW of (c) GaN:Mg-II and (d) undoped samples collected with and without TERS tip. Spectrum of undoped sample collected without tip is vertically shifted down to avoid the overlap.	86
4.9	Typical PL spectra of GaN NWs of the samples (a) undoped, (b and c) Mg doped in increased concentration, GaN:Mg-I and GaN:Mg-II respectively, collected at the temperatures 300 and 80 K. (d) DAP1 peak at 4 K for the NWs of Mg doped samples GaN:Mg-I and GaN:Mg-II. Discontinuous lines are fitted data corresponding to the individual peaks.	87
4.10	Typical PL spectra of GaN NWs of the as-grown and annealed samples GaN:Mg-I, collected at the temperature 80 K.	89
5.1	Typical FESEM micrographs of GaN NWs grown under different oxygen concentrations of (a) $\sim 10^5$ ppm; sample R1, (b) $\sim 10^3$ ppm; sample R2. Both show quite rough and nonuniform surface morphology. (c) NWs grown under oxygen concentrations of $\sim 10^2$ ppm; sample R3 and (d) < 2 ppm; sample R4, having the uniform diameter and surface morphology along the NWs. Nanoparticles at the tip of the NWs are clearly observed.	97
5.2	Structural studies of the NWs: Sample R1; (a) Typical low magnification TEM image of NWs shows an irregular surface morphology, (b) HRTEM image of the NW with non-uniform contrast along the wire. Inset shows	98

	FFT image corresponding to HRTEM micrograph of the NW. (c) Magnified view of the HRTEM image of the NW with lattice fringes corresponding to $\{10\bar{1}0\}$ planes of GaN phase. Sample R4; d) Low magnification TEM image of a typical NW, (e) HRTEM image collected near the tip of the NW having Au nanoparticle. Inset shows SAED pattern of the NW, indexed to wurtzite GaN with zone axis along $[0001]$ (f) Magnified view of HRTEM image shows the NW having nonpolar planes ($10\bar{1}0$).	
5.3	Experimental and simulated EELS spectra of GaN NWs. (a) Right side; a simulated pure GaN structure, projected along Z-axis $\parallel (0001)$ and Left side; the corresponding core loss N K -edge spectrum compared with that of the experimental spectrum collected from the NWs of sample R4. (b) Top; A simulated GaN lattice with $2(O_N)$ oxygen defect configuration, Middle and Bottom; simulated core loss N K -edge and O K -edge spectra, respectively, are compared with that of the experimental spectra collected from the NWs of sample R3. (c) Top; A simulated GaN lattice with $V_{Ga}-3(O_N)$ oxygen defect configuration, Middle and Bottom; simulated core loss N K -edge and O K -edge spectra, respectively, are compared with that of the experimental spectra collected from the NWs of sample R1.	101
5.4	The current-voltage characteristics of the four devices made of samples R1, R2, R3, and R4 measured under ± 2 V bias showing the contacts are Ohmic in nature and the increase in resistance for the samples R1 to R4.	103
5.5	Temporal responses of CH_4 sensing by four devices made of NW samples (a) R1, (b) R2, (c) R3, and (d) R4 at different gas concentrations at $125^\circ C$.	104
5.6	The sensor response over a concentration range of 50 – 500 ppm of CH_4 for the device (a) R1, (b) R2, and (c) R3.	105
5.7	Temperature dependent CH_4 sensing response by the devices of samples R1, R2 and R3 showing the increase in response with increasing temperature.	105
5.8	Typical SKPM micrographs of NW samples (a) R4, (b) R3, (c) R2, and (d) R1. In all images, Left side; topography maps and Right side; SP maps. (e) NW diameter dependent SP values extracted from the SKPM maps of sample R4 and (f) SP plot of NWs samples R1, R2, R3, and R4 with different oxygen impurity.	108
5.9	(a) Optical image of the aligned two probes used for the <i>in situ</i> SKPM measurements under gas exposure. Cantilever based Au coated Si probe (dashed arrow line) with beam-bounce feedback is used for the SKPM measurements on NWs dispersed on Au film. Non-optical normal-force feedback is used for the tuning fork based nano-pipette gas delivery probe (solid arrow line). (b) Schematic view of the SKPM study with the <i>in situ</i> gas exposure multiprobe setup.	110
5.10	SKPM measurements on standard Au film for calibration of Au coated Si tip at $100^\circ C$ under 10^{-2} mbar. (a) Topography maps; the RMS roughness is ~ 1.5 nm. SP maps (b) before and (c) during the CH_4 exposure; RMS values (CPD_{RMS}) before and during the gas exposure are ~ 28 mV and ~ 25 mV, respectively.	110
5.11	Typical SKPM micrographs of NWs of sample R4 (Left side) and sample R1 (Right side) acquired at $100^\circ C$ and 10^{-2} mbar. Topography maps of samples (a) R4 and (d) R1. Typical SP maps of samples (b) R4 and (e) R1 before CH_4 exposure. Typical SP maps of samples (c) R4 and (f) R1 during	112

	the CH ₄ exposure. (g) and (h) NW diameter dependent SP values extracted from the SKPM maps of sample R4 and sample R1 respectively, before (green in colour) and during the CH ₄ exposure.	
5.12	NW diameter dependent (a) SBB (Φ_B), (b) depletion width (W) and (c) surface charge density (n_s) values extracted from the SKPM maps of sample R1, before (Green) and during (Red) the CH ₄ exposure. Horizontal dashed lines indicate the mean saturation values in all the plots. (d) Schematic view of the band diagram of GaN NWs showing SBB (Φ_B) and charge transfer process during chemisorption of CH ₄ .	114
5.13	Diameter distribution of NWs sample R1 grown under oxygen rich condition. A large number of NWs having the diameter less than 60 nm are present.	115
6.1	FESEM image of Mg-doped <i>p</i> -GaN NWs on <i>n</i> -Si(111) substrate. Inset shows Au catalyst particles (encircled) at the tip of the wire.	124
6.2	PL spectra of ensemble <i>p</i> -GaN NWs recorded at different locations on the sample at 80 K.	125
6.3	(a) Cross-sectional and (b) 3D schematic views of the heterojunction device of <i>p</i> -GaN/ <i>n</i> -Si in forward bias configuration	126
6.4	FESEM micrograph of single <i>p</i> -GaN NW/ <i>n</i> -Si heterojunction device. Inset shows the magnified view of <i>p</i> -GaN NW with electron beam deposited Pt (primary layer) electrodes.	126
6.5	<i>I-V</i> characteristics of (a) GaIn/ <i>n</i> -Si/GaIn, (b) AuNi/ <i>p</i> -GaN/NiAu and (c) Pt/ <i>p</i> -GaN/Pt under dark at 300 K showing Ohmic nature of the contacts.	127
6.6	Typical <i>I-V</i> characteristics undoped GaN NWs on <i>n</i> -type Si (<i>i</i> -GaN/ <i>n</i> -Si) heterojunction device under dark.	128
6.7	A schematic band diagram for heterojunction between <i>p</i> -GaN NWs and <i>n</i> -Si.	129
6.8	(a) <i>I-V</i> characteristics of ensemble NW of <i>p</i> -GaN/ <i>n</i> -Si heterojunction device under dark condition. (b) Temperature dependent forward bias <i>I-V</i> characteristics of the device under dark.	129
6.9	A schematic cross-sectional side-view (along the NW) of a single NW <i>p</i> -GaN/ <i>n</i> -Si heterojunction device in the forward bias configuration. Inset shows the cross-sectional (across the NW) front-view of the device.	131
6.10	(a) <i>I-V</i> characteristics of a single <i>p</i> -GaN NW/ <i>n</i> -Si heterojunction device under dark condition. (b) Temperature dependent forward bias <i>I-V</i> characteristics of the device under dark.	131
6.11	(a) <i>I-V</i> characteristics of ensemble NW of <i>p</i> -GaN/ <i>n</i> -Si heterojunction device under dark and illumination of different wavelengths. (b) Temporal photoresponse of the ensemble NW device under the illumination of 470 and 530 nm with light ON and OFF.	133
6.12	(a) <i>I-V</i> characteristics of single <i>p</i> -GaN NW/ <i>n</i> -Si heterojunction device under dark and illumination of different wavelengths. (b) Temporal photoresponse of the device under illumination of 470 and 530 nm wavelengths.	134

LIST OF TABLES

Table No.	Title of Table	Page No.
1.1	Comparison of basic physical properties between GaN and other III-nitride binary semiconductors.	3
6.1	Comparison of electrical and photodiode characteristics of ensemble and single <i>p</i> -GaN NW/ <i>n</i> -Si heterojunctions.	135

LIST OF ABBREVIATIONS

NW	Nanowire	SPM	Scanning probe microscopy
LED	Light-Emitting-Diode	AFM	Atomic Force Microscopy
HFET	High Power Field Effect Transistors	SKPM	Scanning Kelvin Probe Microscopy
HEMT	High-Electron Mobility Transistor	TERS	Tip Enhanced Raman Spectroscopy
HVPE	Hydride Vapor Phase Epitaxy	PVD	Physical Vapor Deposition
OMVPE	Organometallic Vapor Phase Epitaxy	EFGS	Exposure Facility For Gas Sensor Testing System
MBE	Molecular Beam Epitaxy	SAED	Selected Area Electron Diffraction
LEEBI	Low Energy Electron Beam Irradiation	FFT	Fast Fourier Transform
1D	One Dimensional	ELNES	Energy-Loss Near-Edge Structure
UV	Ultraviolet	EXELFS	Extended Energy-Loss Fine Structure
CVD	Chemical Vapor Deposition	CPD	Contact Potential Difference
MOCVD	Metalorganic Chemical Vapor Deposition	SP	Surface Potential
APCVD	Atmospheric Pressure Chemical Vapor Deposition	CCD	Charged Coupled Device
LPCVD	Low Pressure Chemical Vapor Deposition	LVM	Local Vibration Mode
VLS	Vapor-Liquid-Solid	FLG	Few Layer Graphene

VS	vapor -solid	SLG	Single Layer Graphene
FESEM	Field Emission Scanning Electron Microscope	UHP	Ultra High Pure
HRTEM	High Resolution Transmission Electron Microscope	DAP	Donor-Acceptor-Pair
EFTEM	Energy Filtered Transmission Electron Microscopy	SBB	Surface Band Bending
FIB	Focused Ion Beam	DFT	Density Functional Theory
EELS	Electron Energy Loss Spectroscopy	CASTEP	Cambridge Sequential Total Energy Package
XPS	X-Ray Photoelectron Spectroscopy	GGA	Generalized Gradient Approximation
PL	Photoluminescence	PAW	Projector Augmented Wave
RMS	Root Mean Square	PMMA	Poly(methyl methacrylate)
YL	Yellow Luminescence	RL	Red Luminescence
BL	Blue Luminescence	UVL	Ultraviolet Luminescence
TO	Transverse Optical	LO	Longitudinal Optical
ZB	Zone Boundary	SO	Surface Optical
DBE	Donor Bound Exciton	FE	Free Exciton

CHAPTER 1

INTRODUCTION

1.1 Group-III Nitrides

1.1.1 Gallium Nitride (GaN):

GaN, as a central and parent compound for the family of all group-III nitride devices, is considered as one of the most important semiconductors after Si. The unique properties of direct and wide bandgap GaN and its family of III-nitrides lead to a range of applications from optoelectronic devices to high-power electronics. The intrinsic tendency of III-nitrides is to form a thermodynamically stable wurtzite structure with a hexagonal symmetry ($P6_3mc$ or C_{6v}^4). The wurtzite structure (Fig. 1.1a) consists of two interpenetrating hexagonal close-packed ($h c p$) sublattices, each with one type of atom, offset along the c -axis by $5/8$ of the cell height ($5c/8$). The unit cell of wurtzite structure contains six group III metal atoms and six nitrogen atoms tetrahedrally coordinated, in the stacking of $ABABAB$ type sequence along c -axis, $[0001]$.^[1]

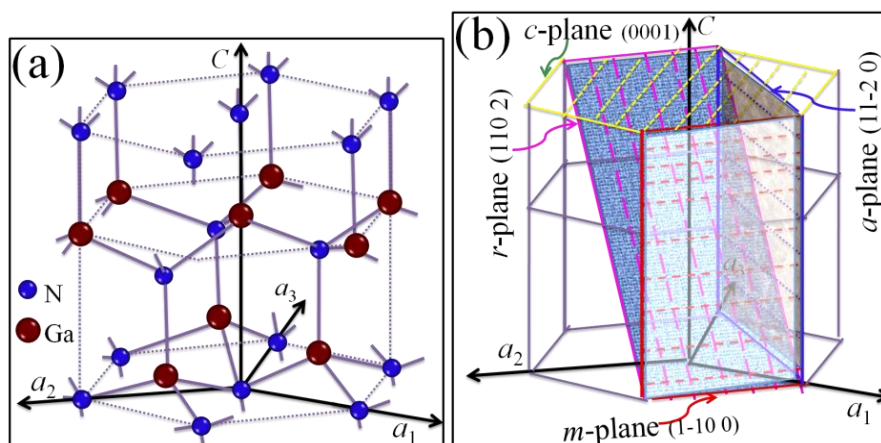


Fig. 1.1 (a) schematic view of the wurtzite GaN structure and (b) different crystallographic planes.

1.1.2 Polar and Nonpolar Surfaces:

Different crystallographic planes and their nomenclatures of wurtzite GaN are shown in Fig. 1.1b. The three crystallographic planes of GaN which have special importance are (0001); *c*-plane, (1-100); *m*-plane and (11-20); *a*-plane. Due to the lack of centre of inversion symmetry (inversion plane perpendicular to the *c*-axis), the wurtzite crystal grown along the *c*-axis has the surface atoms either Ga (Ga-polarity; [0001]) or N (N-polarity; [000-1]). Therefore, the (0001) and (000-1) surface are termed as polar surfaces. Whereas, the (1-100) and (11-20) surface have an equal number of threefold-coordinated Ga and N atoms in the top surface layer which allows the charge neutrality without changes in stoichiometry or reconstruction. Hence these surfaces are termed as nonpolar.^[1]

1.1.3 Polarization Effects:

III-nitrides exhibit highly pronounced polarization effects. There are two kinds of polarizations (spontaneous and piezoelectric) exist in these wurtzite crystals. The lattice parameters in a real wurtzite crystal deviate from the theoretical ratio ($c/a = \sqrt{8/3}$). Therefore the dipole moments which do not cancel each other along the *c*-axis due to the lack of centre of inversion symmetry are induced and consequently give rise to the spontaneous polarization. In addition, when strained along the *c*-axis wurtzite crystal exhibits a polarization called piezoelectric polarization. The strain can be because of lattice mismatch or caused by the thermal expansion coefficient difference between the substrate and the epitaxial layers. Both the strains result in piezoelectric polarizations. The spontaneous and piezoelectric polarizations compete each other depending on the surface and interface polarities and affect the band diagram of heterostructures of III-nitrides influencing their device properties. Due to the nonpolar nature, however (1-100) and (11-20) surfaces do not show any of these polarizations.^[1]

1.1.4 Properties and Applications:

GaN is intrinsically an *n*-type semiconductor due to non-stoichiometry produced by the nitrogen vacancies resulting in large background electron concentration and posses a direct bandgap of ~3.51 eV at 0 K.^[2-4] The bandgap of the GaN can be tuned by suitable alloying with other group III elements. Thus, it is possible to get access to entire visible spectrum and a large part of the ultraviolet (UV) region which makes it a very exciting optoelectronic material system.^[5,6] Owing to the high chemical stability and significant hardness at elevated temperatures, GaN is an attractive material for protective coatings. In addition to high chemical stability, its wide energy bandgap allows the GaN to be an excellent candidate for device operation at high temperatures and caustic environments. The major properties of GaN are compared with other III-nitride materials in the table 1.1.^[1-3]

Table 1.1 Comparison of basic physical properties between GaN and other III-nitride binary semiconductors.

Property	GaN	InN	AlN
Energy gap (eV) (at 0 K)	3.51	0.7	6.25
Exciton binding energy (meV)	23	9	57
Bohr radius (nm)	2.4	8	1.4
Transition <i>n</i> -type (10^7 V cm^{-1})	direct	direct	direct
Breakdown field (MV.cm^{-1}) (at 300 K)	3.0	2.0	1.8
Saturation electron Velocity ($\times 10^7 \text{ cm.s}^{-1}$)	2.5	4.2	2.0
Electron Mobility ($\text{cm}^2.\text{V}^{-1}.\text{s}^{-1}$) (at 300 K)	1,400	4,000	--
Thermal conductivity ($\text{W.cm}^{-1}.\text{K}^{-1}$) (at 300 K)	2.3	0.8	2.9
Relative dielectric constant, (ϵ_r)	8.9	15	8.5
Refractive index	2.7 for 353 nm	2.56 for 1000 nm	2.58 for 220 nm

The non-centrosymmetric structure of wurtzite GaN and related III-nitrides results in intrinsic nonlinear and anisotropic optical properties. The anisotropy results in uniaxial birefringence, that is, two different refractive indices for polarizations parallel and perpendicular to the *c*-axis.^[7] These refractive indices influence the waveguide property of III-nitrides. The excellent optical and electrical properties of GaN and its family of III-nitrides made them ideal materials for applications in light-emitting diodes (LED), lasers (blue/UV lasers), photodetectors which eventually led to recognition of III-nitrides with Nobel prize (2014).^[8] In addition to thermal and optoelectronic properties of III-nitrides, the electrical properties including the low dielectric constant, high breakdown voltage, inherently high transconductance, and high cut-off frequencies allowed a lot of advances in the area of high power, high-frequency power transistors, high power field effect transistors (HFET) and high-electron mobility transistor (HEMT) for RF transmission and mobile wireless communication applications.^[9]

1.1.5 The Issues in Growth, Property and Applications of GaN:

One of the major issues in the growth and technological development of GaN till today is the lack of commercial native substrates.^[1] Although, the thin films of GaN with improved quality are grown on foreign substrate by hydride vapor phase epitaxy (HVPE), organometallic vapor phase epitaxy (OMVPE), and molecular beam epitaxy (MBE) techniques, the issues of low nitrogen incorporation in Ga and finding a substrate which is thermally and lattice matched with GaN have been existed for several years. At present, GaN is commercially grown on sapphire and SiC, both of which are lattice-mismatched substrates. Lattice-mismatched substrates lead to a substantial density of misfit and threading dislocations (in the range of 10^8 to 10^{10} cm⁻²) which eventually affect almost all the electronic and optoelectronic properties of GaN and its device performances.^[1] Most of the GaN based electronic and optoelectronic devices are made by the growth on sapphire (*c*-Al₂O₃) which

yields in the *c*-plane oriented GaN. As discussed earlier, due to polar nature of the (0001) surfaces of GaN, the strain induced piezoelectric and spontaneous polarizations generate the internal electrostatic fields which affect the device operation, particularly, LEDs (on external quantum efficiencies), lasers,^[10] HFETs.^[11] The issue of polarization effects are overcome by using the nonpolar GaN (*m*- and *a*-axes oriented) surfaces, as they are free of the internal electric fields.^[10] However, the obtained quality of the nonpolar films on different substrates is not as good as that of the polar surfaces.^[1]

The second major challenge in the development of GaN based technology was achieving the *p*-type GaN. The issues were high background donor concentration generated by intrinsic nitrogen vacancies and the oxygen impurities which made the growth of compensated high-resistivity material a big challenge for years.^[1] Later, activation of Mg doping in high-resistivity GaN by low energy electron beam irradiation (LEEBI) method,^[12] and thermal annealing at 700 °C under an N₂ ambience,^[13] for *p*-type conductivity with hole concentration of $\sim 10^{18} \text{ cm}^{-3}$, were established. However, owing to the high binding energy (150-200 meV) of Mg in GaN and self-compensation due to donor-like defects in heavily Mg-doped GaN, achieving high-conductive (hole concentration $> 10^{18} \text{ cm}^{-3}$) *p*-type GaN is still a challenging issue.^[1] In addition, pyramidal or V-shaped defects and stacking faults as a result of heavy Mg doping is another issue in achieving useful optical properties of *p*-type GaN films.^[1] Apart from these, most of the other issues in GaN based III-nitride devices, one way or the other, are related to the growth of these materials which is lagging in commercial processing as compared to the other semiconducting materials.

1.2 GaN Nanowires

One dimensional (1D) semiconductor nanostructures, in particular nanowires (NWs), have emerged as one of the promising classes of functional materials to be used as building blocks

for nanoelectronics. Owing to their large surface to volume ratio, ultra high aspect ratio, ease in the electrical contact formation and unidirectional conduction channels, semiconductor NWs with additional functional properties are proven to be the best alternative for their 3D and 2D counter parts. As a direct and wide bandgap semiconductor material, GaN is no exception to possess all the functional properties which appear from the 1D geometry. However, the major advantage of 1D geometry of GaN NWs is that there is a reduction in the extended defects such as threading and screw dislocations, generated by the lattice and thermal mismatched substrates. In addition, since the high quality single crystalline nature with hexagonal symmetry is possible in NWs, accessing of all the anisotropic properties originating from different crystallographic planes is easier than their 2D counter parts.

GaN based III-nitride NWs have shown to be the potential building blocks for nanoscale electronic and optoelectronic devices such as LED, lasers, HEMT, logic gates, waveguides, photodetectors, solar cells and gas sensors.^[14-24]

1.3 Nanowire Growth

GaN NWs can be grown using almost all the thin film depositions techniques namely MBE, OMVPE and different types of chemical vapor deposition (CVD) methods which include metalorganic CVD (MOCVD), atmospheric pressure CVD (APCVD), low pressure CVD (LPCVD). However, each technique has their own advantages and limitations with respect to the growth of GaN NWs. The most common practice to achieve the 1D geometry into the NW morphology is to follow the growth processes either in vapor-liquid-solid (VLS) or vapor-solid (VS) mechanisms. In both VLS and VS processes, there are two modes of growth, namely axial- and radial- growth processes which compete with each other depending on the growth technique used and affect the NW geometry. Out of these two growth modes, the radial growth is undesirable for NW geometry.^[25]

1.3.1 Vapor-Liquid-Solid (VLS) Process:

The metal catalyst-assisted growth is widely known as the VLS growth. It was initially proposed for the growth of whiskers by Wagner and Ellis.^[26] The growth proceeds via the three phases of matter namely vapor, liquid and solid, and hence the process is termed as VLS. The growth is driven by a catalyst in the liquid phase, without involving in the reaction.

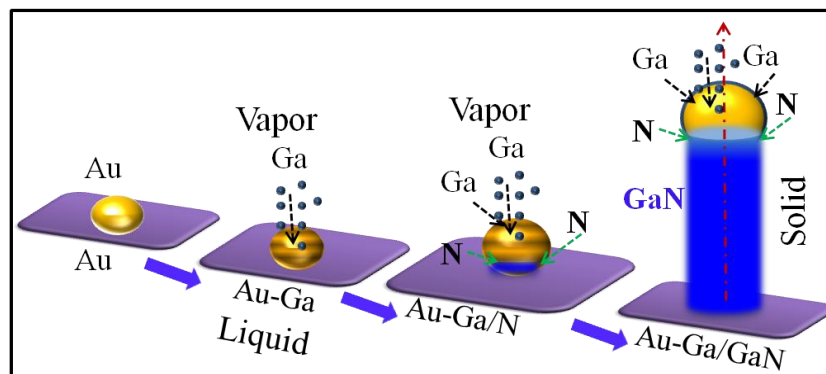


Fig. 1.2 Schematic view of the vapor-liquid-solid process.

In most cases, source materials are heated to vaporize them at elevated temperatures. At a fixed temperature, the reactants in vapor phase dissolve in the liquid catalyst and form an alloy with it. When the liquid alloy reaches its solubility limit during the continual addition of reactant species, it starts precipitating into a solid phase. As long as the reactant supply continues, the process of precipitation from supersaturated liquid is continuous leading to the formation of NWs. The NW geometry of the solid phase is driven by the catalyst particle through liquid-solid interface. For GaN NW growth, usual source materials are Ga metal as precursor and NH_3 or N_2 plasma as N source. Transition metals such as Fe, Ni, Co and Au can be used as catalyst particles. A schematic diagram of the VLS process is shown in the Fig. 1.2. MBE, MOCVD and other CVD techniques are generally used to grow the GaN NWs in the VLS process with precise size and shape controlled by the catalyst particle.

1.3.2 Vapor-Solid (VS) Process:

The VS process relies on direct crystallization of solid from a vapor or via self-catalytic process. This process excludes the inclusion of foreign atoms which sometimes observed in the catalytic VLS growth process. The VS mechanism works based on the large anisotropy with respect to Ga and N adatom diffusion along the polar and nonpolar surfaces which leads to formation of nanowires, nanorods, nanotips, and nanotubes. The NW morphology in the VS process is controlled by the incoming vapor fluxes from the evaporated sources, during the growth. Unlike the VLS process, a full control on NW morphology is highly difficult using the CVD technique via the VS process, which some time result in different morphologies namely nanotips, nanoparticles, nanotubes.^[24,27,28] However, MBE is the potential technique to achieve the NW morphology as well as the other nanostructures in the VS process by controlling the Ga and N fluxes assisted with template approach.^[29-33] Radial growth of NWs over axial growth during the VS process is, however a concern in the MBE technique.

1.4 Impurities in GaN

1.4.1 Intentional and Unintentional Impurities:

GaN is such a material system where almost all kinds of crystallographic defects can be observed. The intentional and unintentional impurities, beyond certain concentrations further enhance the crystallographic imperfections in GaN. The impurities which are most likely to be unintentionally incorporated during GaN growth are carbon (C), oxygen (O), and to some extent hydrogen (H).^[34] The intentional impurities as dopants (*n*-type, and *p*-type) in GaN are Be, Mg, Si, S, Ca, Zn, Ge, Se, and Cd. Most of the time, these intentional and unintentional impurities substitute either on Ga site or on the N site in GaN lattice depending on their formation energies. Generally, elements such as C, Si, and Ge on the Ga sites and O, S, and

Se on the N sites can potentially form shallow donors in GaN. Elements such as Be, Mg, Ca, Zn, and Cd on the Ga sites and C, Si, and Ge on the N sites have the potential of forming relatively shallow acceptors in GaN.^[1]

According to the first principle calculations of formation energies and well established experimental evidences, O is the major devastating unintentional impurity as O_N (formation energy ~33 meV) which acts as a shallow donor and responsible for large background unintended *n*-type conduction in GaN.^[1] In addition, O has large tendency to segregate at edge dislocation, screw dislocation and low energy nonpolar planes of GaN, leading to the formation of additional defects such as pinholes, nanopipes, corrugated surfaces Ga vacancies (V_{Ga}) and its complexes in thin films.^[35-37] Among the intentional impurities for *p*-type GaN, Mg is found to be the best choice which forms Mg_{Ga} shallow acceptors. Mg has low solubility in GaN and is limited by the formation of Mg₃N₂ precipitates when doping level is greater than 10²⁰ cm⁻³. Depending on the growth method, Mg doping in GaN forms precipitates, pyramidal or V-shaped defects, stacking faults.^[1]

1.4.2 Impurity Incorporation Pathways in GaN Nanowires:

Depending on the dopant type, host lattice, and crystallographic orientation, the impurity incorporation pathways can alter in NWs as well as in thin films.^[38-40] The impurity incorporation in thin films is somewhat straight forward where the incorporation path ways are surface of the thin film and interface between thin film and substrate. However, in the NWs, there are several ways an impurity can be incorporated depending on the growth technique and growth process. During the VLS process, *in situ* incorporation takes place thorough either liquid catalyst particle, liquid/solid interface between catalyst and NW, or side facets of the NW depending on the solubility, sticking and diffusion coefficients. In addition, NW/substrate interfaces can also act as impurity incorporation pathway. All these

depending the impurity type (donor or acceptor) and positions of the electronic state (shallow or deep). A schematic view describing the major optical transitions involving intentional and unintentional impurities in GaN, is shown in Figs. 1.4a,b.^[4] Although, NWs of GaN possess similar kind of optical transitions observed in thin films, the conflict over origin of transitions either due to extended defects or impurities can be avoided. Impurities also influence the vibrational properties of GaN by inducing the additional localized atomic oscillations, termed as local vibrational modes (LVM).^[41] The LVM mode frequency and its intensity depends on the impurity atom mass with respect to host lattice atom and concentration, respectively. Such kind of the LVM mode can be seen in highly Mg doped GaN around 657 cm^{-1} .^[41]

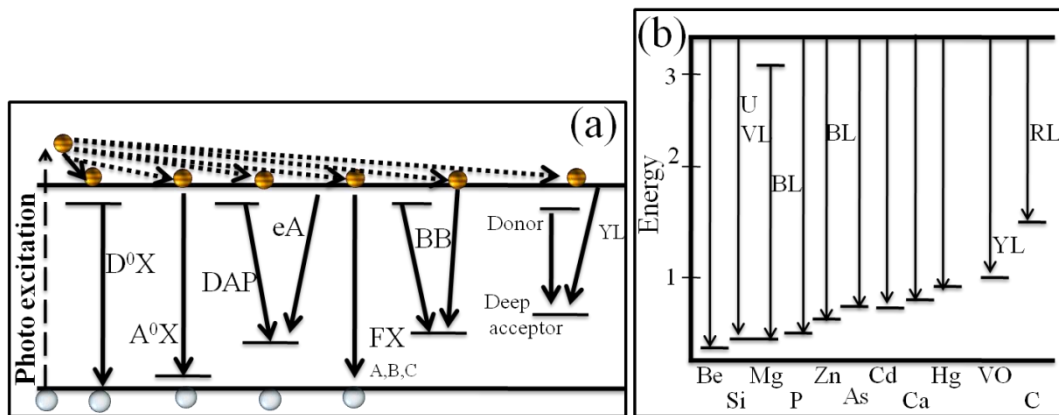


Fig. 1.4 (a) Schematic view of intrinsic and extrinsic optical transitions in GaN. (b) Radiative transitions associated with major impurities in GaN.^[4]

GaN based III-nitrides are promising candidates for photodetectors (photoconductors; PCs, photovoltaics; PVs, and metal-semiconductor-metal junction; MSM) those cover entire visible spectrum and UV wavelength band shorter than 400 nm. Improvements in the growth of III-nitride materials and detector processing have resulted in PV and PC ultraviolet detectors with progressively high responsivity.^[9] However, in case of UV photodetectors, the presence of electrically and optically active levels formed by impurities and surface imperfections cause the response to visible light below the bandgap, and affect the length of the effective conduction region, and detector decay time. The effect of impurities on

characteristics of photodetectors made of GaN NWs is much high due to the large surface-to-volume ratio.^[42] The mechanism of these effects is based on the Fermi-level pinning induced by the impurities at the surface of the NW.^[42,43]

The physicochemical processes at the surfaces of semiconductor nanostructures involved in electrochemical and sensing devices are strongly influenced by the presence of intrinsic or extrinsic defects; GaN is no exception for these effects. Usually pure GaN is chemically inert and thermally stable semiconductor as described earlier. However, the presence of impurities (both intentional and unintentional) modifies the chemical nature of the GaN surfaces. High pure GaN based III-nitride sensors can be used as chemical and bio sensors by forming the Schottky junction with metal or heterojunctions with other semiconducting surfaces.^[24,44-50] However, unintentional O impurities in III-nitrides showed a strong influence of surface oxides on the sensing parameters of nitride devices.^[51] The gas sensitivity of devices made with oxide impurity layer is enhanced by a factor of 50 as compared to that of the devices made without an oxide layer.^[51] III-nitride NWs showed sensor response even without the assistance of any metal particles, which suggested the role of unintentional impurities on the chemical nature of the surface.^[51-53]

1.6 Motivation of the Thesis

GaN NWs are proven to be the excellent candidates as building blocks for nanoscale electronic and optoelectronic applications. However, in large scale production control over the performance of such NW devices involves the issues ranging from growth to processing of their building blocks. Controlling diameter and surface morphology of GaN NWs play a crucial role in defining electrical, optical and electromechanical properties, for using such building blocks for LED, HEMT, chemical sensor and nanoelctromechnical sensor (NEMS) applications. Further improvements on the functionalities of the GaN NW devices can be

achieved by forming heterojunctions with other electronic and optoelectronic materials. The effects of dopants and impurities either on the defect formation or on the evolution of surface morphology of NW and influence on its properties, as consequences of them, are very important issues in the device performance. Understanding of the dopant incorporation paths in NWs can help in tuning the dopant distribution over a precise location along the NW, which is crucial for aforementioned NW devices. However, the extent over which the effects induced by impurity incorporations in GaN NWs, for example NW structure, surface morphology, surface reactivity and carrier transport at surface and interfaces are not explored much.

1.7 Objective and Over View of the Thesis

The prime aim of the present thesis is to understand the effects of unintentional (O) and intentional (Mg) impurities on physicochemical properties in consequence of variations in size, surface morphology, and structure of nonpolar GaN NWs. The thesis is organized in to seven chapters and the contents of each chapter are summarized as follows.

The Chapter 1 briefly introduces the general properties, applications and the issues in GaN. A progress and present status of GaN NWs and their applications are briefly introduced in this chapter. General growth techniques and growth processes of NWs are described. The different type of impurities, their incorporation pathways and the effects on the growth and physiochemical properties of GaN are discussed briefly. This chapter ends with a brief motivation and objective of the thesis.

The Chapter 2 briefly describes the principle and basic parts of the experimental techniques used for growth and characterization of GaN NWs studied in the present thesis work. Growth of GaN NWs is carried out using in-house custom built APCVD system in the VLS process. Detailed design of the APCVD system is discussed in this chapter. High

vacuum thermal evaporation technique used for deposition of catalyst nanoparticles and NW contact materials is discussed. Electron microscopy techniques utilized for morphological studies (field emission scanning electron microscope, FESEM), structural studies (high resolution transmission electron microscope, HRTEM), energy filtered transmission electron microscopy (EFTEM) and device fabrication (dual beam focused ion beam (FIB)-SEM) of the GaN NWs are briefed. Spectroscopic techniques of electron beam (electron energy loss spectroscopy, EELS) and X-Ray beam (X-Ray photoelectron spectroscopy, XPS) sources are described for the elemental analysis in NWs. For the study of optical properties of the NWs, Raman and photoluminescence (PL) spectroscopy techniques are briefly discussed. Scanning probe microscopy (SPM) techniques involving atomic force microscopy (AFM), Kelvin probe microscopy (SKPM) and tip enhanced Raman spectroscopy (TERS) are described in this chapter.

The Chapter 3 describes the general growth process of GaN NWs carried out using APCVD in the VLS process and the optimized growth parameters including the tuning of catalyst particles size and the role of substrate. The effect of unintentional incorporation of oxygen on the nonpolar GaN NWs growth, size and their surface morphology are investigated along with the possible mechanism involved. Size-selective growth of uniform NWs is also demonstrated, in the oxygen reduced condition, using different catalyst sizes. Optical properties including Raman scattering and PL studies along with waveguide properties of the NWs are studied in this chapter.

The Chapter 4 elaborates the detailed growth process of Mg doped GaN NWs using the CVD technique via the VLS process. The morphological and structural studies including the effect of Mg dopants at the liquid/solid interface (Au–Ga/GaN) in the axial growth of GaN NWs are studied in this chapter. Mg incorporation is confirmed using XPS and EELS and localized TERS measurement. The EFTEM studies are used for finding the Mg

incorporation pathway in the GaN NWs. The PL studies on different concentrations of Mg doped GaN NWs are carried out to confirm the activation of Mg atoms as *p*-type dopants in nonpolar GaN NWs.

The Chapter 5 describes the role of oxygen defect complexes, incorporated in nonpolar GaN NWs on methane (CH₄) sensing. Experiments and simulations of EELS studies are performed to understand the type of possible oxygen defects present in the NWs. The resistive sensor devices using ensemble of GaN NWs are fabricated for the sensor study. In order to understand the localized charge transfer process, *in situ* SKPM measurements are carried out on single GaN NWs under gas exposure. A localized charge transfer process, involving V_{Ga}-3O_N defect complex on NW surface is attributed to controlling the global gas sensing behavior of the oxygen rich ensemble GaN NWs.

The Chapter 6 presents the device fabrication of ensemble and single *p*-GaN NW and their heterojunctions with *n*-Si. Electrical and photoresponse characteristics of the individual *p*-GaN NW devices and heterojunction devices with *n*-Si are reported in this chapter. Photovoltaic and photoconducting mode characteristics of the heterojunction devices are analyzed and the key parameters including ideality factors, fill factors and responsivity of ensemble and single NW heterojunction devices are estimated and compared.

The Chapter 7 summarizes the major findings of the studies carried out on GaN NWs and the directions for future work.

1.8 References

- [1] H. Morkoç, *Handbook of Nitride Semiconductors and Devices, Materials Properties, Physics and Growth*, John Wiley & Sons, Vol.1, **2008**.
- [2] I. Vurgaftman, J. Meyer, *J. Appl. Phys.* **2003**, 94, 3675.
- [3] J. Wu, *J. Appl. Phys.* **2009**, 106, 011101.
- [4] M.A. Reshchikov, H. Morkoç, *J. Appl. Phys.* **2005**, 97, 061301.
- [5] T. Kiyoshi, Y. Akihiko, S. Adarsh, *Wide Bandgap Semiconductors: Fundamental Properties and Modern Photonic and Electronic Devices*, Springer, Heidelberg, **2007**.
- [6] Z.C. Feng, *III-Nitride Semiconductor Materials*, World Scientific, **2006**.
- [7] H. Morkoç, *Handbook of Nitride Semiconductors and Devices, Electronic and optical properties in nitrides*, John Wiley & Sons, Vol.2, **2008**.
- [8] E. Gibney, *Nature* **2014**, 514, 152.
- [9] H. Morkoç, *Handbook of Nitride Semiconductors and Devices, GaN based optical and electronic devices*, John Wiley & Sons, Vol.3, **2008**.
- [10] P. Waltereit, O. Brandt, A. Trampert, H. Grahn, J. Menniger, M. Ramsteiner, M. Reiche, K. Ploog, *Nature* **2000**, 406, 865.
- [11] J. Ibbetson, P. Fini, K. Ness, S. DenBaars, J. Speck, U. Mishra, *Appl. Phys. Lett.* **2000**, 77, 250.
- [12] H. Amano, M. Kito, K. Hiramatsu, I. Akasaki, *Jpn. J. Appl. Phys.* **1989**, 28, L2112.
- [13] S. Nakamura, T. Mukai, M. Senoh, *Jpn. J. Appl. Phys.* **1991**, 30, L1998.
- [14] S. Chattopadhyay, A. Ganguly, K.-H. Chen, L.-C. Chen, *Crit. Rev. Solid State Mater. Sci.* **2009**, 34, 224.
- [15] J.C. Johnson, H.-J. Choi, K.P. Knutsen, R.D. Schaller, P. Yang, R.J. Saykally, *Nat. Mater.* **2002**, 1, 106.

- [16] R. Yan, D. Gargas, P. Yang, *Nat. Photonics* **2009**, 3, 569.
- [17] M.H. Huang, S. Mao, H. Feick, H. Yan, Y. Wu, H. Kind, E. Weber, R. Russo, P. Yang, *Science* **2001**, 292, 1897.
- [18] Y.B. Tang, Z.H. Chen, H.S. Song, C.S. Lee, H.T. Cong, H.M. Cheng, W.J. Zhang, I. Bello, S.T. Lee, *Nano Lett.* **2008**, 8, 4191.
- [19] Y. Dong, B. Tian, T.J. Kempa, C.M. Lieber, *Nano Lett.* **2009**, 9, 2183.
- [20] C.-Y. Chen, G. Zhu, Y. Hu, J.-W. Yu, J. Song, K.-Y. Cheng, L.-H. Peng, L.-J. Chou, Z.L. Wang, *ACS Nano* **2012**, 6, 5687..
- [22] F. Gonzalez-Posada, R. Songmuang, M. Den Hertog, E. Monroy, *Nano Lett.* **2012**, 12, 172.
- [23] M.D. Brubaker, P.T. Blanchard, J.B. Schlager, A.W. Sanders, A. Roshko, S.M. Duff, J.M. Gray, V.M. Bright, N.A. Sanford, K.A. Bertness, *Nano Lett.* **2013**, 13, 374.
- [24] P. Sahoo, S. Dhara, S. Dash, S. Amirthapandian, A.K. Prasad, A. Tyagi, *Int. J. Hydrogen Energy* **2013**, 38, 3513.
- [25] J. Wallentin, M.T. Borgström, *J. Mater. Res.* **2011**, 26, 2142.
- [26] R. Wagner, W. Ellis, *Appl. Phys. Lett.* **1964**, 89..
- [27] P. Sahoo, S. Dhara, S. Dash, A.K. Tyagi, *Nanosci Nanotechnol-Asia* **2011**, 1, 140.
- [28] P. Sahoo, S. Dhara, S. Amirthapandian, M. Kamruddin, S. Dash, B.K. Panigrahi, A.K. Tyagi, *Cryst. Growth Des.* **2012**, 12, 2375.
- [29] S. Shetty, J. Ghatak, S. Shivaprasad, *CrystEngComm* **2014**, 16, 3076.
- [30] C. Chèze, L. Geelhaar, B. Jenichen, H. Riechert, *Appl. Phys. Lett.* **2010**, 97, 153105.
- [31] T. Gotschke, T. Schumann, F. Limbach, T. Stoica, R. Calarco, *Appl. Phys. Lett.* **2011**, 98, 103102.
- [32] V. Consonni, A. Trampert, L. Geelhaar, H. Riechert, *Appl. Phys. Lett.* **2011**, 99, 033102.

- [33] P. Lefebvre, S. Fernández-Garrido, J. Grandal, J. Ristić, M.-A. Sánchez-García, E. Calleja, *Appl. Phys. Lett.* **2011**, 98, 083104.
- [34] S.J. Pearton, J.C. Zolper, R.J. Shul, F. Ren, *J. Appl. Phys.* **1999**, 86, 1.
- [35] J.E. Northrup, *Phys. Rev. B* **2006**, 73, 115304.
- [36] J. Elsner, R. Jones, M. Haugk, R. Gutierrez, T. Frauenheim, M. Heggie, S. Oberg, P. Briddon, *Appl. Phys. Lett.* **1998**, 73, 3530.
- [37] S.C. Cruz, S. Keller, T.E. Mates, U.K. Mishra, S.P. DenBaars, *J. Cryst. Growth* **2009**, 311, 3817.
- [38] I. Arslan, N.D. Browning, *Phys. Rev. Lett.* **2003**, 91, 165501.
- [39] S. J. Pearton, J.C. Zolper, R.J. Shul, F. Ren, *J. Appl. Phys.* **1999**, 86, 1.
- [40] B. Heying, R. Averbeck, L. Chen, E. Haus, H. Riechert, J. Speck, *J. Appl. Phys.* **2000**, 88, 1855.
- [41] H. Harima, *J. Phys.: Condens. Matter* **2002**, 14, R967.
- [42] A. Cavallini, L. Polenta, M. Rossi, T. Stoica, R. Calarco, R.J. Meijers, T. Richter, H. Lüth, *Nano Lett.* **2007**, 7, 2166.
- [43] R.-S. Chen, H.-Y. Chen, C.-Y. Lu, K.-H. Chen, C.-P. Chen, L.-C. Chen, Y.-J. Yang, *Appl. Phys. Lett.* **2007**, 91, 223106.
- [44] C.P. Chen, A. Ganguly, C.Y. Lu, T.Y. Chen, C.C. Kuo, R.S. Chen, W.H. Tu, W.B. Fischer, K.H. Chen, L.C. Chen, *Anal. Chem.* **2011**, 83, 1938.
- [45] W. Lim, J.S. Wright, B.P. Gila, J.L. Johnson, A. Ural, T. Anderson, F. Ren, S.J. Pearton, *Appl. Phys. Lett.* **2008**, 93, 072109.
- [46] S. Pearton, F. Ren, *Instrumentation & Measurement Magazine, IEEE* **2012**, 15, 16.
- [47] K.H. Baik, H. Kim, S.-N. Lee, E. Lim, S. Pearton, F. Ren, S. Jang, *Appl. Phys. Lett.* **2014**, 104, 072103.

- [48] P. Sahoo, S. Suresh, S. Dhara, G. Saini, S. Rangarajan, A.K. Tyagi, *Biosens. Bioelectron.* **2013**, 44, 164.
- [49] C.F. Lo, C.Y. Chang, B.H. Chu, S.J. Pearton, A. Dabiran, P.P. Chow, F. Ren, *Appl. Phys. Lett.* **2010**, 96, 232106.
- [50] G.S. Aluri, A. Motayed, A.V. Davydov, V.P. Oleshko, K.A. Bertness, N.A. Sanford, M.V. Rao, *Nanotechnology* **2011**, 22, 295503.
- [51] O. Weidemann, M. Hermann, G. Steinhoff, H. Wingbrant, A. Lloyd Spetz, M. Stutzmann, M. Eickhoff, *Appl. Phys. Lett.* **2003**, 83, 773.
- [52] F. Yun, S. Chevtchenko, Y.-T. Moon, H. Morkoç, T.J. Fawcett, J.T. Wolan, *Appl. Phys. Lett.* **2005**, 87, 073507.
- [53] V. Popa, I. Tiginyanu, V. Ursaki, O. Volcius, H. Morkoç, *Semicond. Sci. Technol.* **2006**, 21, 1518.

CHAPTER 2

EXPERIMENTAL TECHNIQUES

2.1 Introduction

A brief description of the experimental techniques utilized for the growth of GaN NWs and their characterization for morphological, elemental, structural, optical and electrical studies are discussed in this chapter. GaN NWs were grown using APCVD system, by applying catalyst assisted VLS process. The depositions of catalyst and electrode films for NW device were carried out by physical vapor deposition (PVD) technique, using vacuum thermal evaporation system. Electron microscopy techniques such as FESEM, TEM were used for morphological and structural studies of the as grown NWs. The elemental analysis of the NWs was performed by EELS and XPS techniques.

Optical and electronic properties of the NW were studied using Raman and PL spectrometers. Further, SPM techniques involving AFM, SKPM and TERS were performed to study the surface and electronic properties the NWs. The single NW devices were fabricated by dual beam technique, electron and FIB using FIB-SEM system. The electrical properties of the single and ensemble NWs devices were studied using source-measurement units by making the electrical contacts through electrical micro-probes station. Gas sensing properties of the NW devices were studied using custom-built exposure facility for Gas sensor testing system (EFGS).

2.2 Growth Techniques

2.2.1 Vacuum Thermal Evaporation System:

Thermal evaporation is one of the techniques among the PVD methods, to deposit mostly metal films.^[1] The three major processes are involved in this technique are the generation,

transport, and condensation of vapor phase species of metals under high vacuum ($\sim 10^{-6}$ Torr). The evaporation of the metal is carried out by means of thermally heating the source material at high temperature produced by the resistive heating principle. High temperature can be generated by applying the high voltage to a heating element made of W or Mo either in the form of filament or boat. Fig. 2.1 shows the schematic diagram of a typical vacuum thermal evaporation system with necessary components.

All the catalyst and electrode metal film depositions for the studies reported in this thesis were carried out in high vacuum thermal evaporation system (HINDHIVAC Vacuum Coater-12A4D) having the multi-source evaporation and *in situ* thickness monitor facilities. For catalyst purpose, varying thickness of Au metal films and for electrodes on GaN NW devices, multilayer of Ti/Al/Ti/Au and Ni/Au films were deposited. The important components of the system are listed below.

A. Vacuum chamber: Beljar type

B. Vacuum pumping system:

- a) Rotary pump (ED-15, 250 Lit/Min)
- b) Diffusion pump (OD-114D, 280 Lit/Sec)
- c) Vacuum gauges (Pirani and Penning Gauges)
- d) Ultimate vacuum: 1×10^{-6} mbar.
- e) Primary current (Maximum) : 100 A

C. Digital thickness monitor: quartz crystal thickness monitor, 0.1A/sec resolution.

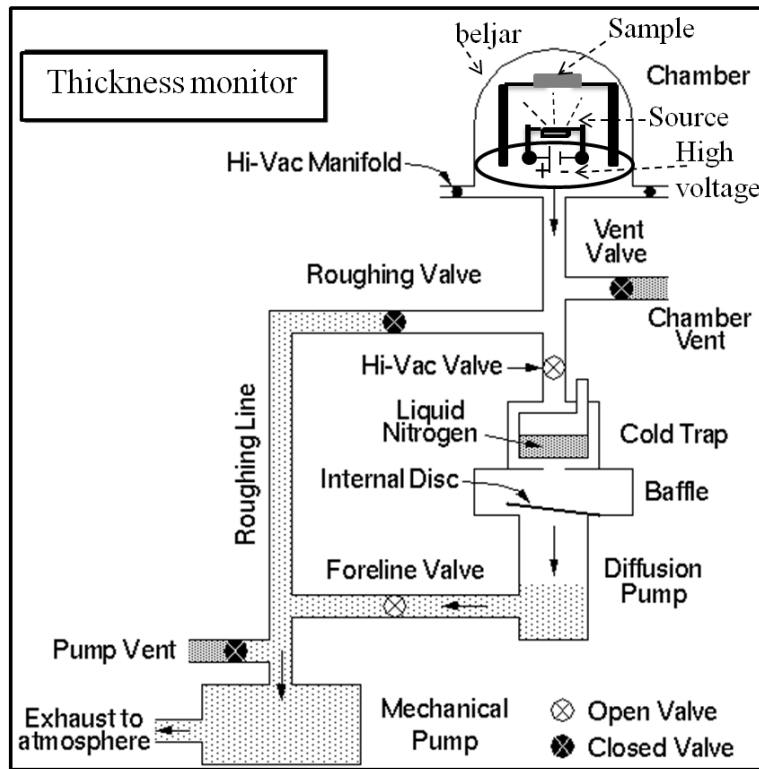


Fig. 2.1 Schematic view of the vacuum thermal evaporation system.

2.2.2 Atmospheric Pressure Chemical Vapor Deposition (APCVD) System:

The APCVD process involves the formation of a solid film on heated substrate surface by means of chemical reaction in a gas or in the vapor phase. The major difference between the physical and chemical vapor deposition methods is the pre-existence of the material to be deposited as a thin film in PVD method, while in CVD, the material forms after the chemical reaction. The major processes involved in the CVD method are the generation, transport, absorption and chemical reactions of vapor phase reactant species on the substrate surface.^[2]

The generation of the reactant vapor species is produced by the evaporation and decomposition of the gas, liquid or solid sources. The transport of vapor phase species is usually carried out by flowing a carrier gas, mostly an inert gas. A complete experimental setup of the custom-built APCVD system used for the growth of GaN NWs reported in the

present thesis is depicted schematically in the Fig. 2.2. The major components of the APCVD system are listed below.

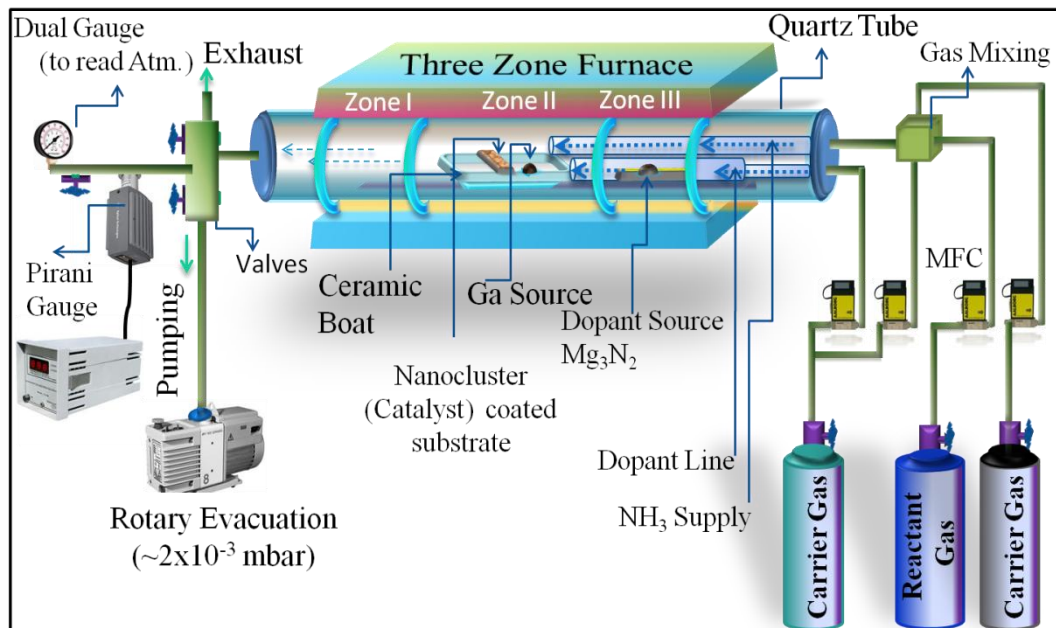


Fig. 2.2 Schematic view of the APCVD system used for growth of GaN NWs.

A. High temperature split three zone vacuum tube furnace: (MTI-OTF-1200X-III)

- a) Heating elements: Fe-Cr-Al Alloy doped by Mo
- d) Heating zone lengths: 220(Zone1), 440(zone2), 220(zone 3) in mm
- c) Max. Temperature: 1200 °C
- d) Temperature controllers: PID automatic control
- d) Temperature accuracy: $\pm 1^\circ\text{C}$

B. Vacuum pumping system:

- a) Rotary pump (Edwards, RV12)
- c) Vacuum gauges (Pirani Gauges)
- d) Max. Vacuum: 2×10^{-3} mbar.

C. Gas delivery system:

- a) Gas lines for reactant (NH₃) and carrier (N₂, Ar, Ar+H₂) gases.

b) Mass flow controllers (Aalborg, MKS)

2.3 Morphological Characterization

2.3.1 Field-Emission Scanning Electron Microscope (FESEM):

When a beam of electrons with high energy incident on a sample, electrons interact elastically and inelastically with specimen.^[3] Elastic scattering results from the deflection of the incident electron by the specimen atomic nucleus or by outer shell electrons of similar energy. The elastically scattered electrons through an angle of more than 90° are called backscattered electrons (BSE) (Fig. 2.3a). The inelastic scattering occurs through several interactions between incident electrons and specimen atoms, and results in the loss of primary beam. The excitation of the specimen electrons during the ionization of specimen atoms by incident electron beam leads to the generation of secondary electrons (SE) typically having energies of less than 50 eV and can be used to image or analyze the sample. By detecting and scanning the BSE and SE, image formation can be carried out for the topography and Z-contrast variations in the sample. The major components of a SEM (Schematic view, Fig. 2.3b) are listed below.

A. Electron gun: Thermionic (tungsten, LaB₆) or Field emission (FE) (tungsten tip)

B. Anode

C. Electromagnetic lenses: (condenser and objective lenses; CL and OL)

D. Electron detectors: (SE and BSE detectors)

E. Specimen stage

Morphological studies of the GaN NWs and catalyst particles reported in the present thesis were carried out using FESEM (SUPRA 55 Zeiss) with 30 kV source.

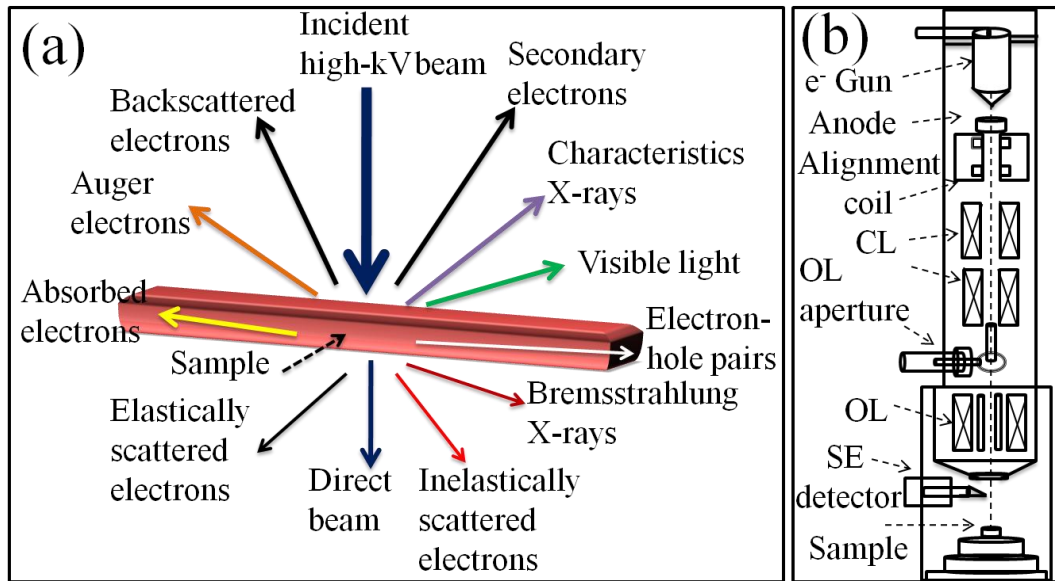


Fig. 2.3 (a) Schematic view of the several interactions occurs in a material due to the incidence of high energy electron beam. (b) Block diagram of a FESEM showing the major parts of the system.

2.4 Structural and Elemental Characterization

2.4.1 Transmission Electron Microscope (TEM):

TEM is capable of displaying magnified images of a thin specimen, typically with a magnification in the range 10^3 to 10^6 . TEM exploits three different interactions of electron beam-specimen; Unscattered electrons (transmitted/direct beam), elastically scattered electrons (diffracted beam) and inelastically scattered electrons (Fig. 2.3a).^[3] When incident electrons are transmitted through the thin specimen without any interaction occurring inside the specimen, then the beam of these electrons is called transmitted. The transmission of unscattered electrons is inversely proportional to the specimen thickness. Areas of the specimen that are thicker will have fewer transmitted unscattered electrons and so will appear darker, conversely the thinner areas will have more transmitted electrons and thus will appear lighter. Another part of the incident electrons that are elastically scattered by atoms in the specimen are then transmitted through the remaining portions of the specimen. All electrons

follow Bragg's Law and thus are scattered according to $2d\sin\theta = n\lambda$, where d being atomic spacing, θ being angle between incident electrons and atomic planes of the specimen, λ being wavelength of the incident electrons and n is the integer, form the diffraction patterns (DP). By selecting the diffracted beam from a selected area on the specimen, selected area electron diffraction (SAED) pattern can be obtained.

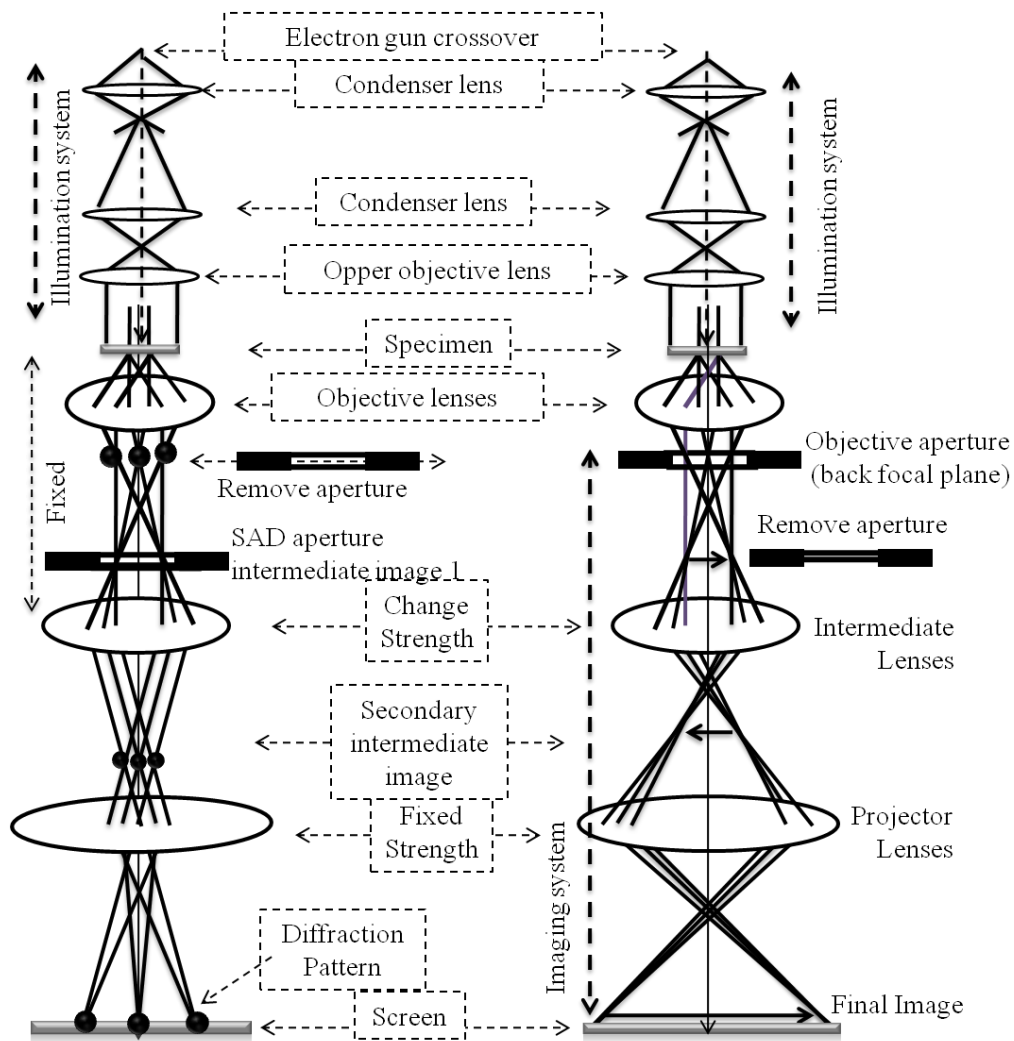


Fig. 2.4 Ray-diagram of a TEM showing the diffraction mode operation (left side) and standard imaging mode operation (right side) with the major components of the system.

The major components of the TEM can be categorised into the illumination system, the objective lens/stage, and the imaging system. By adjusting these three systems and selecting the appropriate scattered electron beams from the specimen, several types of TEM

images can be obtained which includes, bright field and dark field images, SEAD patterns, high resolution images (HRTEM) and fast Fourier transform (FFT) images. The components comprising the three systems in the TEM are listed below with a schematic diagram (Fig. 2.4).

A. Illumination system: Electron gun, condenser lenses, condenser apertures

B. Objective lens/stage: objective lenses, sample stage/holder

C. Imaging system: Intermediate and projector lenses, fluorescent viewing screen or computer display via a detector, CCD, or TV camera.

Structural studies of the GaN NWs reported in the present thesis were carried out using HRTEM (LIBRA 200FE Zeiss) with 200 kV FE electron source.

2.4.2 Electron Energy Loss Spectroscopy (EELS) and Energy Filtered TEM (EFTEM):

The EELS involves measurement of the energy distribution of electrons that have interacted with a specimen and lost characteristic amount of energy due to the inelastic scattering.^[4] The inelastic scattering of incident electrons results in several process in the specimen such as inter- and intra-band transitions, plasmon interactions, ionization of core shell (K, L, M, N) electrons and plural scattering. To observe the characteristic energy loss of incident electrons (typically 100 keV), the transmitted electron beam is directed into a high-resolution electron spectrometer. The spectrometer separates the electrons according to their kinetic energy and produces an electron energy loss spectrum showing the number of electrons (scattered intensity) as a function of the decrease in kinetic energy (typically, 0 – 1500 eV).^[4] The spectrum is divided in to two regions of interactions, low-loss and high-loss interaction regions. The low-loss interaction region is typically 0-50 eV energy loss, which consists a zero-loss peak (0 eV), inter- and intra-band transitions (2-20 eV) and plasmon interactions (5-

30 eV). The high-loss interaction region (>50 eV energy loss) consists ionization edges of core shells, energy-loss near-edge structure (ELNES) and extended energy-loss fine structure (EXELFS).

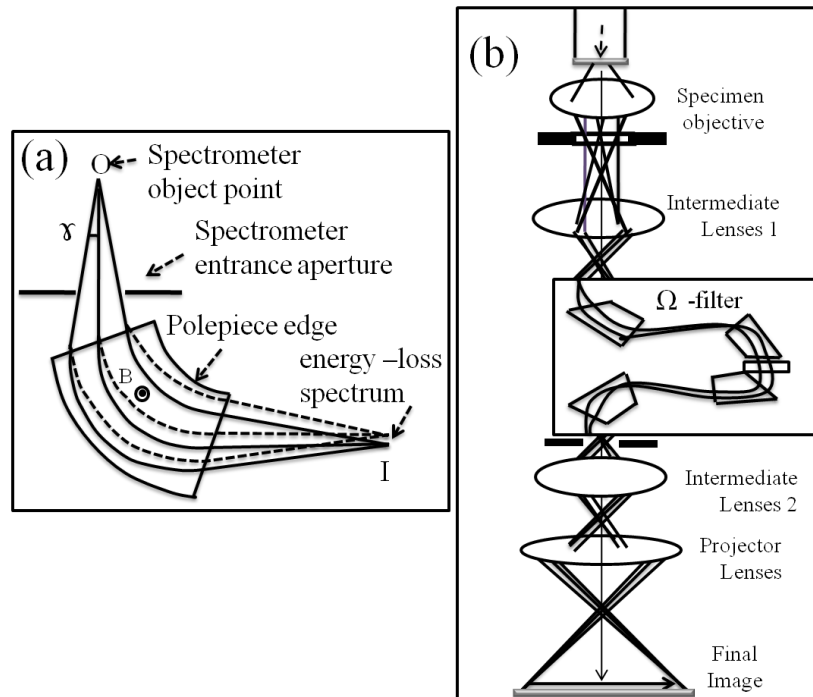


Fig. 2.5 (a) Ray-diagram of a magnetic prism in a plane perpendicular to the magnetic field. Solid lines represent zero-loss electrons ($E = 0$); dashed lines represent those have lost energy during transmission through the specimen. (b) Block diagram of a TEM-EELS system having in-column second order corrected omega energy filter.

The EELS is performed using a spectrometer based on magnetic prism (Fig. 2.5a) connected to a TEM. A highly uniform magnetic field ($B = 0.01$ T) produced between two parallel faces of an electromagnet in the magnetic prism, exerts a force $F = evB$ on each electron and bend the electrons in to circular paths of radius $R = (m/e)(1/B)v$, where e , m and v are electron charge, speed, and relativistic mass. Depending on the kinetic energy of the electrons entered in to the magnetic prism, electrons are dispersed and collected by the detector to produce a spectrum. Instead of recording the energy-loss spectrum from a particular region of specimen, a magnified image of the specimen (or its diffraction pattern) can be displayed at a selected energy loss. This can be carried out by filtering the electrons

either by using a narrow slit inserted at the spectrum plane or by changing the spectrometer current, to form an EFTEM image. The major components for the EELS and EFTEM imaging in a TEM system with in-column imaging filter are shown in a schematic view (Fig. 2.5b). EELS and EFTEM studies of the GaN NWs reported in the present thesis were carried out using a TEM (LIBRA 200FE Zeiss) with 200 kV FE electron source and in-column second order corrected omega energy filter type spectrometer with an energy resolution of 0.7 eV.

2.4.3 X-Ray Photoelectron Spectroscopy (XPS):

The XPS works based on the process of photoemission (Fig. 2.6a) in which electron is ejected from a core level of an atom in the specimen by an incident X-ray photon of energy $h\nu$.^[5] The energy of the emitted photoelectrons is then analysed by the electron spectrometer and the data is presented as a graph of intensity (counts or counts/s) versus electron energy. The photoelectrons are ejected with discrete kinetic energy (E_k) given by $E_k = h\nu - E_B - W$, where E_B is the binding energy of the atomic orbital from which electron originates and W is the work function of the spectrometer. The energy of the photoelectron is characteristic of the element from which it is ejected, thus enabling the identification of the atomic species. The major components of an XPS system (schematic view, Fig. 2.6b) are listed below.

A. X-ray source/gun: A twin anode configuration providing Al K_α (1486.6 eV) or

Mg K_α (1253.6 eV).

B. Hemispherical electron energy analyzer

C. Electron detector

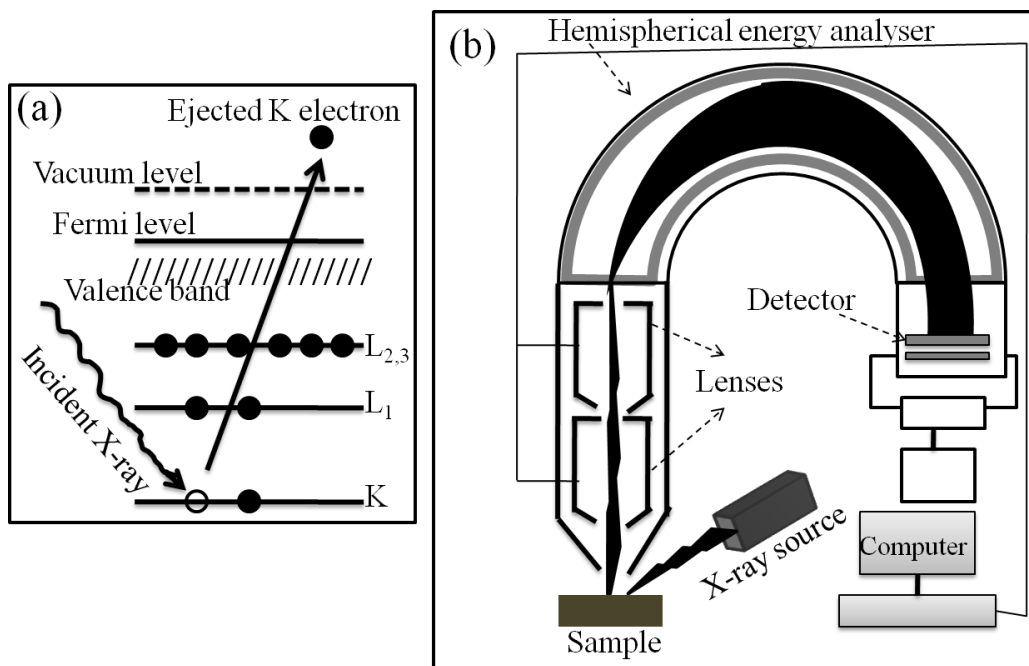


Fig. 2.6 (a) Schematic view of the X-ray induced photoelectron emission process. (b) Block diagram of the XPS setup with major components.

In the present thesis, XPS studies on GaN NWs were carried out using an X-ray source of nonmonochromatic Al K_{α} (1486.6 eV), and the binding energy values were measured by referencing with respect to the C 1s peak. The spectra were processed by applying Shirley type background and curve fitted with mixture of Gaussian–Lorentzian line shape.

2.5 Optical Characterization

2.5.1 Raman Spectroscopy:

The scattering of light, as a result of its interaction with matter, can be classified as elastic (Rayleigh scattering) or inelastic (Raman or Brillouin scattering) (Fig. 2.7). In the former case the scattered light is observed at the same frequency as the incident light ($h\nu_0$). On the other hand, inelastically scattered light, which is detected at different frequencies, constitutes the Raman or Brillouin signals of the sample. The Raman effect results from the change in polarizability of the molecule induced by the interaction of vibrational and/or rotational motions of molecules with the electromagnetic radiation. The Raman scattering, is very weak

($\sim 10^{-5}$ of the incident beam) and has frequencies $\nu_0 \pm \nu_m$, where $\nu_m (= \Delta\nu)$ is a vibrational frequency of a molecule.^[6] The $\nu_0 - \nu_m$ and $\nu_0 + \nu_m$ lines are called the Stokes and anti-Stokes lines, respectively. Thus, in Raman spectroscopy, we measure the vibrational frequency (ν_m) as a shift from the incident beam frequency (ν_0). The Raman shift can be expressed as $\Delta\nu = (1/\lambda_{\text{incident}}) - (1/\lambda_{\text{scattered}}) \text{ cm}^{-1}$. The Raman scattering intensity collected using a spectrometer is $I_s = (8\pi^4 \alpha^2 / \lambda^4 r^2) (1 + \cos^2 \theta) I_0$, where α is polarizability of the molecule, λ is wavelength of the incident light, I_0 is incident intensity, θ is angle between incident and scattered light, and r is distance from centre of scattering to detector. The major components of a Raman spectrometer are listed below.

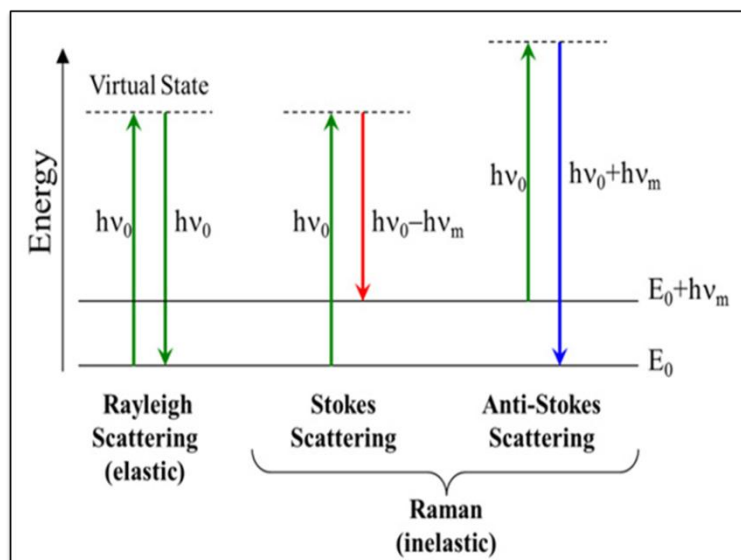


Fig. 2.7 Schematic view of the elastic and inelastic processes in a material with incidence of light.

- A. Excitation source: Continuous wave lasers
- B. Sample illumination and collection system: set of lenses or microscope
- C. Rayleigh rejection filter: Notch/Edge filters.
- D. Wavelength selector: Monochromator
- E. Detector and computer control/processing system: photomultiplier tube (PMT) / CCD.

The present Raman scattering studies on GaN NWs reported in this thesis are carried out using a micro-Raman spectrometer (inVia, Renishaw). All the major components along with available faculties of the system are reported below along with its block diagram (Fig. 2.8).

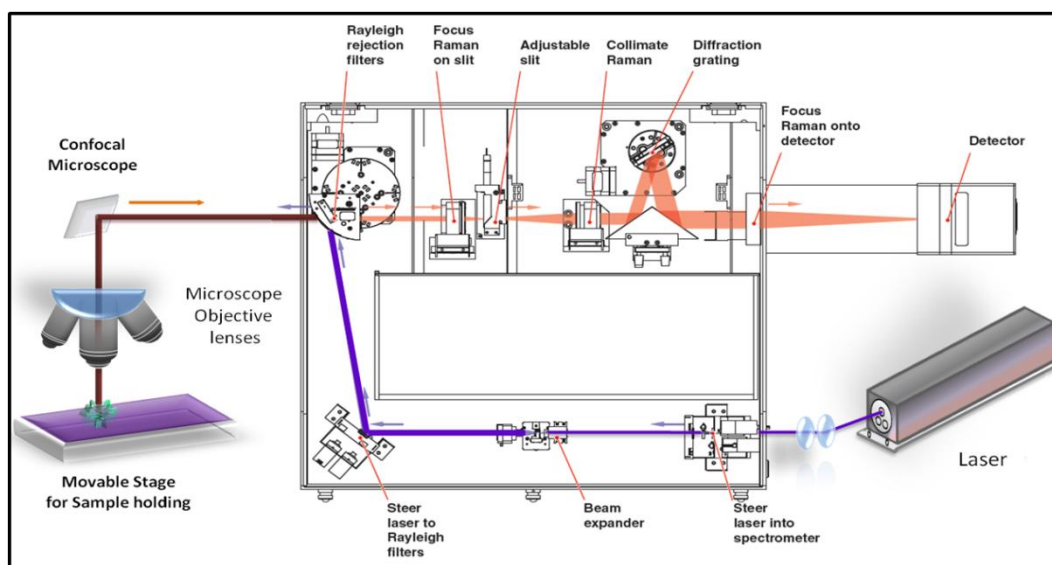


Fig. 2.8 Block diagram of the Raman setup with major parts, used for the present studies.

A. Lasers: Ar⁺ laser with 514.5 and 488 nm (Total power ~ 150 mW),

He-Cd Laser (UV - 325 nm, Power 10 mW), and 785 nm NIR laser.

B. Microscope and lenses (Leica): Backscattering configuration, standard and confocal mode, ×5, ×20, ×50, ×100, ×15 (UV), and ×40 (UV) lenses

C. Rayleigh rejection filter: Notch filter.

D. Monochromator: Gratings; 600, 1800, 2400, and 3000 gr.mm⁻¹

E. Detector: Thermoelectrically cooled CCD and InGaAs detectors

F. Additional facilities: Liquid N₂ stage for low temperature measurements, motorized XYZ stage with 100 nm XY step size resolution (Renishaw, MS20), for imaging and sample movements.

2.5.2 Photoluminescence Spectroscopy:

When an electromagnetic radiation incident on a semiconductor material, a fraction of the incident photons get reflect at the surface and the rest transmit through medium. Inside the medium some of the photons may absorb or scatter while the remainder passes through the sample. Some of the absorbed photons may dissipate as heat or reemit at a different frequency.^[7] The latter process is known as photoluminescence. This is a radiative recombination process among excited carriers, such as, electrons/holes or excitons in semiconductor during external optical excitation process. When the incident photons of energy higher than that of the bandgap (E_g) of the semiconductor the electrons get excited from the ground state to a higher energy state via absorption of photons. After some energy loss (relaxation) the excited electrons return to the ground state while emitting photons of energy lower than the exciting photons (Fig. 2.9).

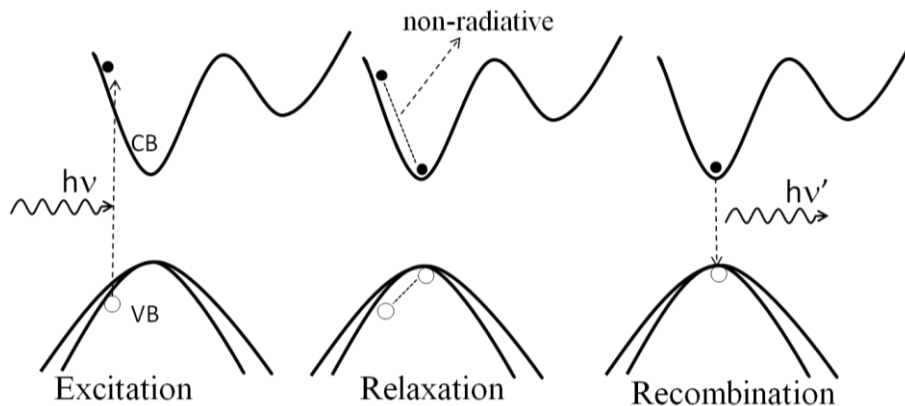


Fig. 2.9 Schematic view of the PL process in a direct bandgap semiconductor.

The luminescence property of a material is also strongly affected by the presence of native defects, impurity, dopants and absorbed molecular species. Assuming a direct bandgap semiconductor with low carrier density, the PL intensity can be expressed as

$$I_{PL} = (\hbar\omega - E_g)^{1/2} \exp\left[-\frac{\hbar\omega - E_g}{k_B T}\right],$$

where the first term arises from the joint density of states in the interband transition and the second factor arises from the Boltzmann distribution

of the electron and holes.^[7] The luminescence efficiency of direct bandgap semiconductors is relatively higher compared to indirect bandgap materials. In typical direct gap semiconductors, the optical transitions between the valence and conduction bands are dipole-allowed and have large matrix elements. In addition to band edge luminescence, transitions associated with impurities and defects in semiconductors can be studied very effectively by analyzing steady-state PL (SSPL) spectra, time-resolved PL (TRPL) spectra, or PL excitation (PLE) spectra. The major components of a typical PL apparatus are listed below.

A. Excitation source:

B. Sample illumination and collection system: set of lenses or microscope

C. Wavelength selector: Monochromator

d. Photon detector

The present PL studies on GaN NWs reported in this thesis are carried out using the same setup used for the micro-Raman measurements (inVia, Renishaw) (Fig. 2.8), by choosing the He-Cd laser source (325 nm), edge filter for rejecting the source wavelength, 2400 gr.mm⁻¹ grating and a CCD detector. Low temperature PL measurements were performed by cooling the samples in a liquid N₂ cooling stage. All the major components along with available faculties of the system are reported below along with its schematic block diagram (Fig. 2.8).

2.6 Electrical Characterization

2.6.1 Dual-Beam (Electron and Focused Ion Beam) Deposition System:

A dual-beam system is a combination of FIB with SEM.^[8] Both beams (ion and electron beams) can operate independently or simultaneously and focus on the same point of the specimen. FIB technique is based on the use of accelerated and focused ion beams and is a powerful and versatile tool for the maskless fabrication of structures and devices in the micro

and nanometer scales. This can be performed by the milling and deposition capabilities of a focused ion beam, the latter being achieved by the ion beam-assisted decomposition of a metalorganic gas precursor of the specific material that has to be deposited. When certain metalorganic compounds are introduced in the beam path, they can be dissociated and part of the compound will be deposited on the surface of the sample, where the beam is scanned and the rest will be removed by the vacuum system, giving rise to the ion-assisted deposition. Furthermore, when reactive gases are introduced in the chamber while the ion beam is scanned over the surface, enhanced milling occurs via a combined milling and reactive etching. The process can be used in order to selectively remove certain materials. Ion beam can also be used for imaging the specimen, however it damages the specimen. In such cases, the electron beam allows non-destructive observation. The combination of the FIB and a SEM in the same machine, giving rise to the dual-beam or cross-beam machines, further expands the capabilities of the technique by the possibility of performing electron-beam assisted deposition and inspection, which is less harmful than using the ion beam. Electron-assisted deposition can be performed when the metalorganic precursor is inserted in the electron beam path. The major components of the dual-beam system (schematic view, Fig. 2.10) are similar to the FESEM, in addition to the ion beam column and gas injection system, which are listed below.

A. FIB column: Ga⁺ source (Liquid Ga injection system),

Ion optics: electrostatic lenses,

Fast beam blanker

B. Gas injection system (GIS): Metalorganic precursor sources and heating lines.

In the present thesis, single GaN NW devices were fabricated using dual-beam system (FIB-SEM, AURIGA, Zeiss) having GIS facilitated with 5 lines for water, insulator (SiO₂), XeF₂, and metalorganic precursors of Pt and W.

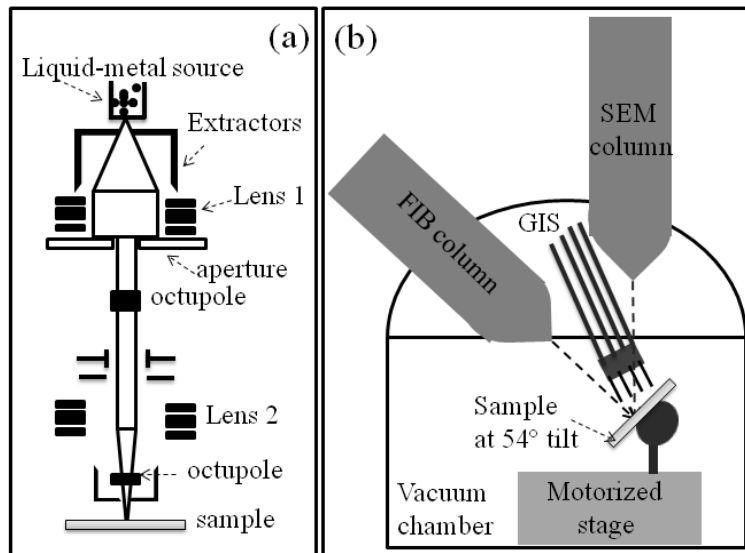


Fig. 2.10 (a) Block diagram of the FIB column. (b) Schematic view of the dual-beam deposition system.

2.6.2 Electrical Probe Station and Source-Measurement Units:

Electrical probe station is a set of metallic probes of very fine tips (typically few microns tip size) mounted on micropositioners and connected with electrical cables. In addition, the microscopy arrangement and the sample stage in the probe station allows the viewing and precise movement of the sample and micro-probes. The micro-probes are connected with electrical cables, preferably a Kelvin type to reduce the noise in the very low electrical signals. The biasing of the sample and measurement of the electrical signals can be carried out by using the source-measure unit which can apply a precise and controlled voltage and currents and can measure both of them at required intervals or a period of time.

In the present studies, since devices are made of single GaN NWs connected with micro-pads, the electrical biasing of the devices was carried out using an electrical probe station (Everbeing). The Au coated W probes of tip sizes 5-10 μm are used to connect the electrodes. Agilent source-measure units (B2902A and B2911A) which can apply and measure the 100 and 10 fA currents are used to study current-voltage characteristics of the fabricated devices.

2.7 Scanning Probe Microscope Coupled with Light

2.7.1 Atomic Force Microscopy (AFM):

The AFM is one of the techniques in the family of SPMs which are used for studying surface properties of materials from the atomic to the micron level. The AFM probes the surface of a sample with a sharp tip, a couple of microns long and often less than 100\AA in diameter. In conventional AFMs, the tip is located at the free end of a cantilever that is 100 to $200\ \mu\text{m}$ long. Forces between the tip and the sample surface cause the cantilever to bend, or deflect. A detector measures the cantilever deflection as the tip is scanned over the sample, or the sample is scanned under the tip. The measured cantilever deflections allow a computer to generate a map of surface topography. AFMs can be used to study insulators and semiconductors as well as electrical conductors. Several forces typically contribute to the deflection of an AFM cantilever.

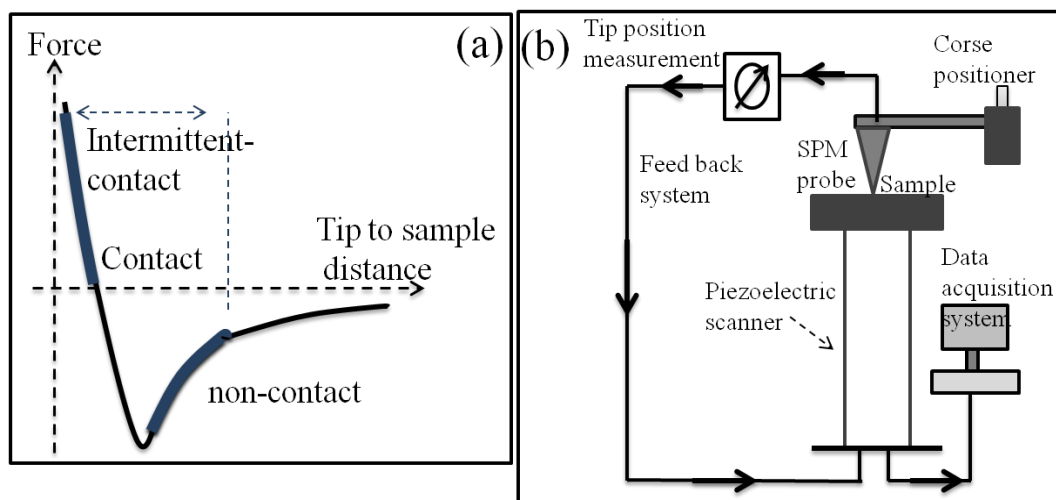


Fig. 2.11 (a) Interaction force Vs distance between tip and sample. (b) Block diagram of general SPM system with major components.

The force most commonly associated with atomic force microscopy is an inter-atomic force called as Vander Waals force and varies with distance between the tip and the sample

(Fig. 2.11a). AFM can be operated in the three modes (contact, non-contact and intermittent) by choosing the three regimes of forces between tip and sample.^[9] The major components commonly present in all SPM systems (schematic, Fig. 2.10b) are listed below.

- A. Scanning probe tip
- B. Coarse tip positioning system
- C. Feedback system
- D. Piezoelectric sample scanner.

The AFM used for the studies on GaN NWs reported in the present thesis is one of the parts of the SPM system (Nanonics, MultiView 4000; Multiprobe imaging system). The MultiView 4000 uses normal force tuning fork technology with a high Q factor and Phase Feedback to allow control of the probe/sample separation. Tuning forks in normal force mode with phase or amplitude feedback permit high performance and ease of operation for AFM imaging in intermittent mode. The AFM tips are glass-based probes and allow for the tips to be approached very close together. Unlike standard piezo scanners that keep probes separated, the 3D Flat scanner (very good AFM resolution, large vertical (axial) displacement of up to 100 μm for sample scanning and up to 30 μm for tip scanning) is used in this system.

2.7.2 Scanning Kelvin Probe Microscopy (SKPM):

The SKPM is a tool to measure the local contact potential difference (CPD) between a conducting AFM tip and the sample, thereby mapping the work function or surface potential (SP) of the sample with high spatial resolution. The CPD between the tip and sample is defined as $V_{\text{CPD}} = (\phi_{\text{tip}} - \phi_{\text{sample}}) / e$, where ϕ_{tip} and ϕ_{sample} are the work functions of the tip and sample respectively, e is the electron charge.^[10] In a SKPM, both topography and SP or CPD maps can be obtained simultaneously by scanning the AFM tip on a sample. When an AFM tip is brought close to the sample surface, an electrical force is generated between the tip and

sample surface, due to the differences in their Fermi energy levels. Fig. 2.12a shows the energy level diagram of the tip and sample surface ($\phi_{\text{tip}} \neq \phi_{\text{sample}}$), when they are separated, electrically contacted and in biasing condition. This force can be nullified by applying external bias (V_{DC}) of the same magnitude of V_{CPD} with opposite direction. Between the probe and the sample an electrical force exists in addition to the regular van-der-Waals force. The term for the total electrical force is $F = dE/dz$, where E is the potential energy and z is the tip to the sample distance. The force due to applied DC voltage can be expressed as $F_{\text{DC}} = \frac{dC}{2dZ} [(\Delta\phi - V_{\text{DC}})^2 + \frac{V_{\text{AC}}^2}{2}]$, where C is the capacitance, $\Delta\phi$ is the CPD, V_{DC} and V_{AC} are DC and AC voltages applied between the tip and the sample, respectively.

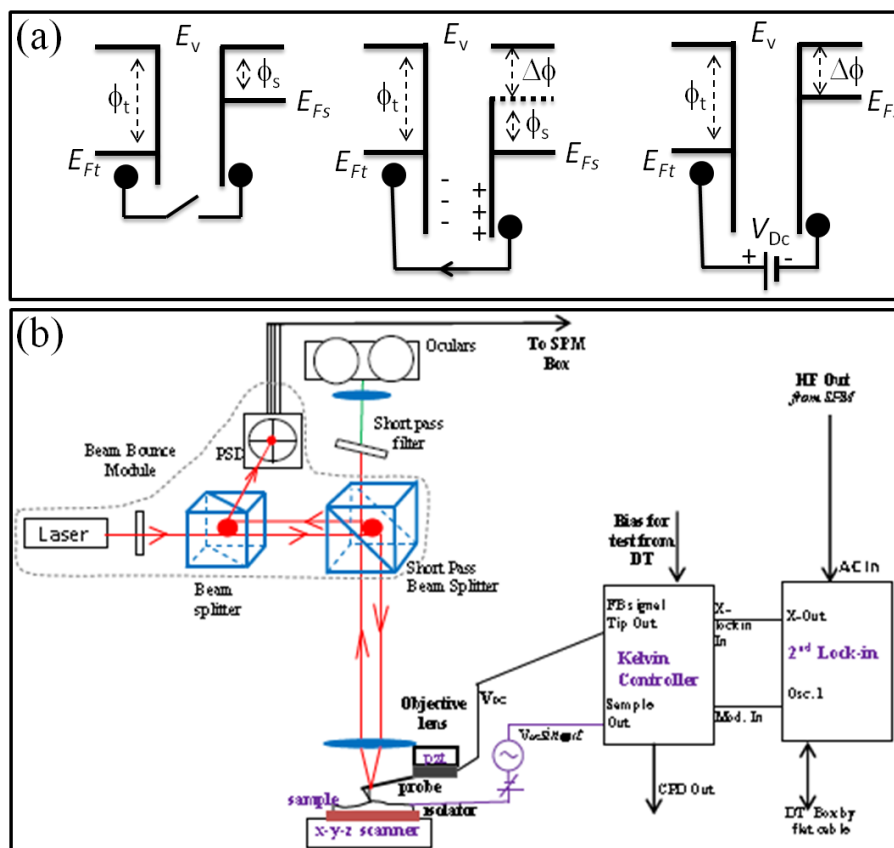


Fig. 2.12 (a) The schematic view of the energy level diagrams of the tip and sample surface, when they are separated, electrically contacted and in biasing condition. (b) Block diagram of the SKPM setup.

The block diagram of the SKPM used in the present studies along with major components is shown (Fig. 2.12b). The SKPM (Nanonics, MultiView 4000; Multiprobe imaging system) setup was operated in a closed chamber capable of maintaining a vacuum of 10^{-6} mbar, and the scanning tip (Au coated Si) was under the standard beam-bounce feedback mechanism. Fountain pen nanopipette gas delivery probe facility has been used for *in situ* SKPM measurements under gas exposure.

2.7.3 Tip-Enhanced Raman Spectroscopy (TERS):

Since the Raman scattering is a very weak ($\sim 10^{-5}$ of the incident beam) and when observed for scattering from the few molecules, it is almost negligible. However the Raman signal can be enhanced by increasing the electric field interacting with the few molecules. The field enhancement can be obtained by surface plasmons of metal nanoparticles when they are excited with laser light whose energy matches with the plasmon resonance.^[11] The Raman intensity would then be enhanced by the fourth power of the field enhancement factor. The SPM tip of small radius coated with noble (Au, Ag) metal film keeps the enhancement of the electric field local around the tip apex and can improve the spatial resolution down to 10 nm. Since a metallic tip is used for enhancing the Raman signal, the technique is term as TERS. The enhancement factor for TERS is mostly controlled by the shape and size of the tip apex. Evanescent field in the hot spots, where the electric field is significantly enhanced, are usually generated in regions of high curvature. The tip-sample distance also influences the enhancement factor. The gap between the tip and the sample must be controlled accurately with a piezoscanner and feedback mechanism to keep the enhancement factor stable. The ability to move the sample and the tip with independent piezoelectric elements enables the precise positioning of the laser beam with respect to the tip apex and the rastering of the sample for imaging. It allows the laser to be locked on a hot spot around the tip apex, and the sample can be then scanned independently to obtain an image with optimum enhancement.

The SPM setup coupled with a Raman spectrometer and laser light can be used to perform the TERS measurements.

In the present studies on GaN NWs, TERS measurements were carried out using the SPM setup (Nanonics, MultiView 4000; Multiprobe imaging system) coupled with a laser Raman spectrometer (inVia, Renishaw) in the backscattering configuration. The tip is AFM bent glass probe attached with Au particle (< 100 nm) and operated it under non-optical normal force feedback. The Raman signals are collected by exciting the samples with 514.5 nm laser using 50X objective with numerical aperture (N.A.) of 0.42 and analyzed with 1800 gr.mm^{-1} grating and a CCD detector.

2.8 Exposure Facility for Gas Sensor Testing System (EFGS)

The gas sensing properties of GaN NWs were studied using a custom-built EFGS testing system (Schematic view, Fig. 2.13). The important components of the system include double walled stainless steel chamber, heater stage (also acting as sample holder), scroll pumps, flow controllers, pressure gauges, readout system, gas delivery lines and pneumatically actuated valves. The vacuum is maintained by using dry scroll pumps. Gas flow and temperature are controlled by mass flow controller (MFC) and PID controller respectively. The entire operation of the exposure facility system can be controlled externally using supervisory control and data acquisition (SCADA) software. For electrical biasing and measurements on the sample, Agilent source measurements units were utilized. The sensor response, upon exposure to gases, manifests as a change in resistance of the sample. This resistance or other electrical output can be recorded on a PC via GPIB interface which is configured to acquire data at user-defined intervals. The parameters those can be varied are vacuum inside the chamber, operation temperature and gas mass flow ratios to generate different concentrations of gas atmospheres. The gas sensing measurements were carried out using EFGS system in

the dynamic condition. In dynamic sensing, the gas was flown at a fixed flow rate over the sensor device while maintaining a fixed pressure in the sensing chamber under constant pumping using a dry pump.

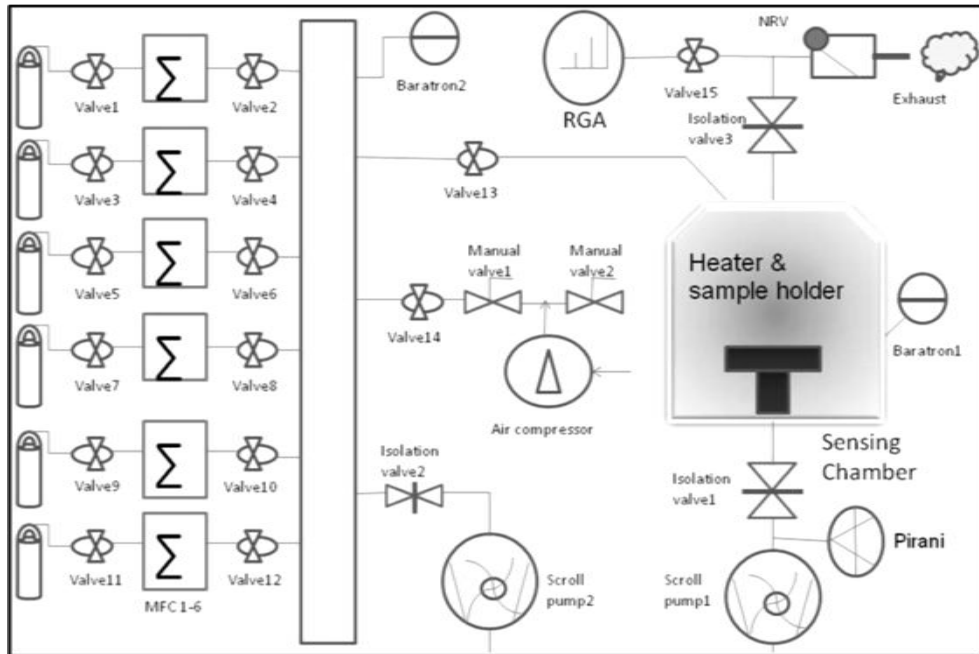


Fig. 2.13 The block diagram of the exposure facility for gas sensor (EFGS) testing system.

2.9 Summary

The experimental techniques utilized for the study of GaN NWs reported in this thesis are described briefly with basic principle, major components of the apparatus, and their technical specifications with schematic or block diagrams. The APCVD and vacuum thermal evaporation systems, used for the growth of nanostructures, are described. Electron microscopy techniques of FESEM, TEM, TEM-EELS and EFTEM utilized for morphology, structural, and elemental analysis of the nanostructures are elaborated with the help of schematic diagrams. Raman, PL setups are briefed for measuring optical properties. Dual-beam FIB-SEM deposition system and electrical measurement setups are discussed. SPM techniques involving AFM, KPFM and TERS after coupling with the spectrometer are described. The EFGS setup, utilized for studying the gas sensing properties of the NW devices is briefed.

2.10 References

- [1] K.L. Chopra, *Thin film phenomena*, 1st ed., McGraw-Hill, **1969**.
- [2] C.E. Morosanu and G. Siddall, *Thin Films by Chemical Vapour Deposition*, Springer Science+ Business Media, **1990**.
- [3] D.B. Williams, C.B. Carter, *Transmission electron microscopy: a textbook for materials science*. 2nd ed., Springer, **2009**.
- [4] R.F. Egerton, *Electron energy-loss spectroscopy in the electron microscope*, Springer Science+ Business Media, **2011**.
- [5] J.F. Watts, J. Wolstenholme, *An introduction to surface analysis by XPS and AES*, Wiley-VCH, **2003**.
- [6] J. Ferraro, K. Nakamoto, C.W. Brown, *Introductory raman spectroscopy*, 2nd ed., Academic Press, **2003**.
- [7] Y. Peter, M. Cardona, *Fundamentals of semiconductors: physics and materials properties*, Springer Science & Business Media, **2010**.
- [8] L.A. Giannuzzi, *Introduction to focused ion beams: instrumentation, theory, techniques and practice*, Springer Science & Business Media, **2006**.
- [9] R. Howland, L. Benatar, *A Practical Guide: To Scanning Probe Microscopy*, DIANE Publishing Company, **1998**.
- [10] W. Melitz, J. Shen, A.C. Kummel, S. Lee, *Surf. Sci. Rep.* **2011**, 66, 1.
- [11] M. Lucas, E. Riedo, *Rev. Sci. Instrum.* **2012**, 83, 061101.

CHAPTER 3

EFFECT OF OXYGEN IMPURITY ON MORPHOLOGICAL, STRUCTURAL AND OPTICAL CHARACTERISTICS OF NONPOLAR GaN NANOWIRES

3.1 Introduction

The most studied ubiquitous inevitable impurity in group III nitrides is the oxygen (O) which impoverishes the nitride phase and alters the electrical, optical and electromechanical properties. The degree of O contamination depends on the growth technique.^[1,2] The common source of this contamination in CVD based technique is known to be the reactant NH_3 and carrier gases, where as in MBE it is remnant water vapor.^[3] Apart from these sources, a background level of O can be liberated from the substrates and growth chamber like sapphire and quartz tubes. The consequences of O contamination are more in case of atmospheric pressure CVD technique as the base vacuum of the chamber and purging precursors are inadequate to reduce the O concentration to background level. In spite of these problems, the extent of the effect of unintentional incorporation of O in GaN NWs is unexplored. Although carbon impurity influences the optical properties by its electronic contribution,^[4] but unlike oxygen it does not directly participate in the VLS reaction process with Ga. Moreover, there is hardly any report showing morphological changes with carbon contamination. The reproducibility and homogeneity of required size and morphology of GaN NWs in a simple CVD technique are critical issues for mass production of ensemble NW devices.

As discussed earlier in the Chapter 1, GaN NWs can be grown in the VS and the VLS processes. However, these growth process themselves have their own limitations for the synthesis of GaN NWs in the CVD technique. Reports on self-catalyzed CVD grown GaN

nanostructures with controlled morphology are limited owing to the difficulties encountered in controlling important parameters such as Ga and N flux rates and subsequent switching between the fluxes. Growth modes significantly influence the resulting nanostructure's shape, size, and crystal structure. In fact, the efforts made in our earlier studies on the VS assisted growth of GaN nanostructures showed the diverse shapes and sizes of the GaN structures even up to micron scale. For example, GaN spirals were grown in CVD technique using Ga (99.999%) metal as a source material and the reactive NH_3 used as a precursor at a constant flow rate of 10 sccm at 900°C for 2 h. A large quantity of spiral like microstructures of GaN was found on high pure alumina (99.95%) boat without use of any catalyst. Fig. 3.1 shows the FESEM image of GaN spirals having average diameter $\sim 20\ \mu\text{m}$. Inset shows the magnified image of a single spiral.

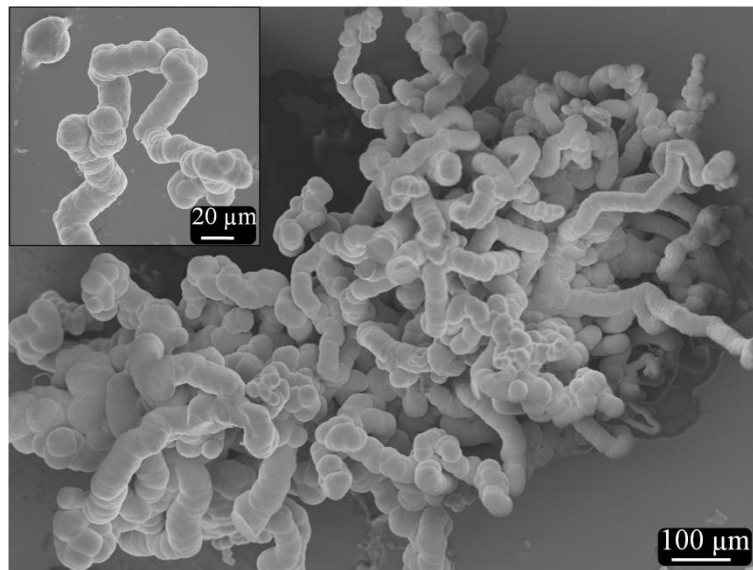


Fig. 3.1 FESEM micrograph of GaN spirals grown in the VS process on alumina boat. Inset shows the magnified image of a single spiral of diameter $\sim 20\ \mu\text{m}$ and a single sphere of GaN.

Apart from the growth parameters (Ga and N fluxes), the VS growth mode of GaN nanostructures was also influenced by the surface polarity of the GaN and substrate materials.^[6] For example, various shapes of GaN nanostructures were grown on few layer

graphene (FLG) as a template on SiO₂/Si, without the assistance of any catalyst. Two kinds of FLG templates, one with COOH- functionalized FLG powder and other was mechanically exfoliated FLG, were used for growing the GaN nanostructures. Morphological investigations on the nanostructures showed that the GaN nanostructures (Figs. 3.2a-d) with various morphologies were grown only on the template regions of the substrate.^[7]

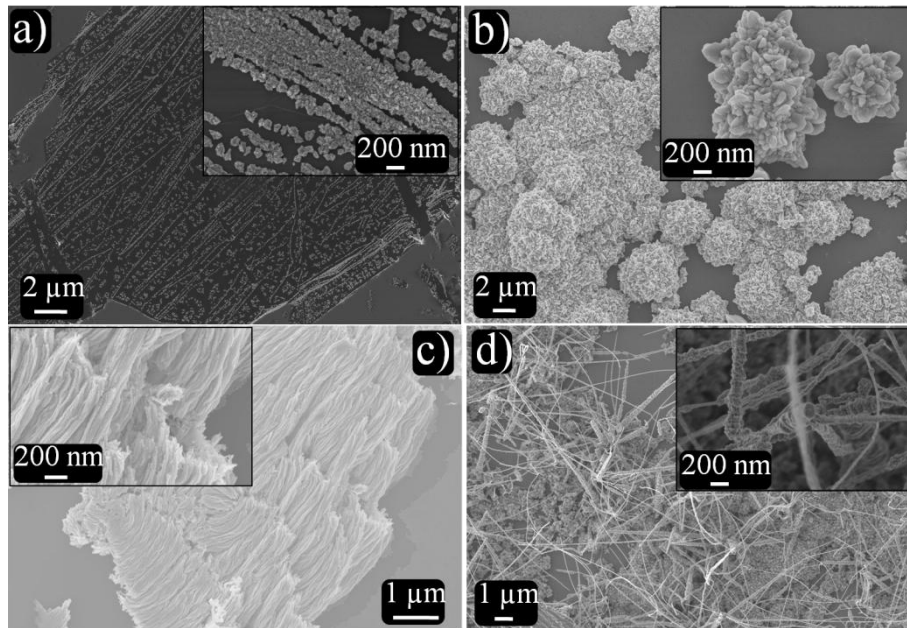


Fig. 3.2 FESEM micrographs of GaN nanostructures grown in the VS process on the substrates (a) mechanically exfoliated FLG template from HOPG transferred on to SiO₂, (b)-(d) GaN nanostructures grown on COOH- functionalized FLG powder dispersed on SiO₂ substrates. Inset shows the magnified images of the nanostructures.

In contrast to the VS process, the growth of the NWs in the VLS mode is driven by the catalyst particle. The final product purity of the GaN NWs depends on the catalyst contamination in the NWs by the process of diffusion and defect formation. Transition metals such as Fe, Ni, and Co are found to be efficient catalysts for the precipitation of supersaturated GaN in the catalyst. However, Au is a better choice of catalyst for synthesizing GaN NWs owing to its high defect formation energy (~4 eV) in GaN as compared to Ni (1.2 eV).^[8] Hence, the NW purity is expected to be better while using Au catalyst even though it has poor solubility for N as compared to other transition metals, like

Fe and Ni. The diameter distribution of target NWs is strongly influenced by the catalyst particle size. So the diameter of the NWs can be tuned by controlling the catalyst particle size. The crystallographic orientation and alignment of the NW can also be controlled via epitaxial growth followed by the VLS process.^[9] The length of the NWs depends on the reaction time and reactant flux. Despite the control of size, shape and orientation of the NWs in the VLS process, impurity concentration can strongly influence these parameters.

In this context, an effort is made to understand the effect of oxygen impurity on size, shape, and surface morphology, structural and optical properties of GaN NWs and the results are discussed in this chapter. Prior to the oxygen impurity role, the size of the catalyst particle and the effect of substrate on the growth of GaN NWs in the VLS process have been studied.

3.2 Growth of GaN Nanowires in the VLS Process Using APCVD

3.2.1 Tuning the Au Catalyst Particle Size and Shape:

The size and shape of the Au catalyst particles for the VLS growth of GaN NWs are tuned based on the principles of dewetting phenomenon in thin film. As-deposited films dewet or agglomerate to form arrays of islands when heated. This can happen well below a melting temperature of the film so that dewetting occurs while the film remains in the solid state. The driving force for dewetting is the minimization of the total energy of the free surfaces of the film and substrate, and of the film-substrate interface. The driving force for dewetting increases and the rate of dewetting is accelerated with decreasing film thickness and increasing temperature. As a consequence, temperature of dewetting decreases with a decrease in the film thickness.^[10] Thus the final size and shape of the particle can be controlled by controlling the initial film thickness and the annealing temperature and time.

Au films of different thicknesses were deposited on the Si(100) substrate. Prior to the Au deposition, the substrates were cleaned using standard RCA (Radio Corporation of

America) procedure involving the three steps; i) removal of organic contaminations (by RCA-1; H₂O/NH₄OH/H₂O₂ in the ratio 50:10:10), ii) removal of thin oxide layer (by RCA-2; HF/H₂O in the ratio 1:50) and iii) the removal of metallic contaminations (by RCA-3; H₂O/HCl/H₂O₂ in the ratio 60:10:10). Then, the substrates were ultrasonically cleaned with acetone and isopropyl alcohol (IPA), rinsed with distilled water and were dried by blowing nitrogen gas. The cleaned substrates were then loaded in to a vacuum thermal evaporation system containing molybdenum boat loaded with Au. The evaporation chamber was then evacuated to 10⁻⁶ mbar. Au films of different thicknesses (1 to 5 nm) were deposited on Si substrates in different batches by controlling the current or applied voltage to the Mo boat and the deposition time. The film thickness was monitored *in situ* using a quartz crystal thickness monitor.

The FESEM micrograph of as deposited Au film of recorded thickness 1 nm on Si substrate (Fig. 3.3a) shows the islands of Au with irregular shape. Since the amount of the Au metal deposited for the film is very less and the large variation in the substrate temperature with respect to evaporation source, the deposited Au metal formed islands (inset in Fig. 3.3a). The shape of the Au islands was tuned by further dewetting the islands by annealing at 900 °C for 15 min in the inert atmosphere. Uniform shaped Au nano particles of size ~20 nm are observed (Fig. 3.3b) after the annealing. However, the size distribution of the nanoparticles is not uniform. This could be due to the Ostwald ripening process among the smaller particles at high temperature.

The annealing temperature and time dependent studies on Au films of varying recorded thicknesses were also carried out. An Au film of recorded thickness 2 nm, which was annealed for 15 min at temperature 800 °C (Fig. 3.4a), showed incomplete dewetting process of the Au islands having irregular shape and size. However, uniform shaped Au nanoparticles of size ~ 30 (±5) nm are observed for the sample which annealed at 900 °C for

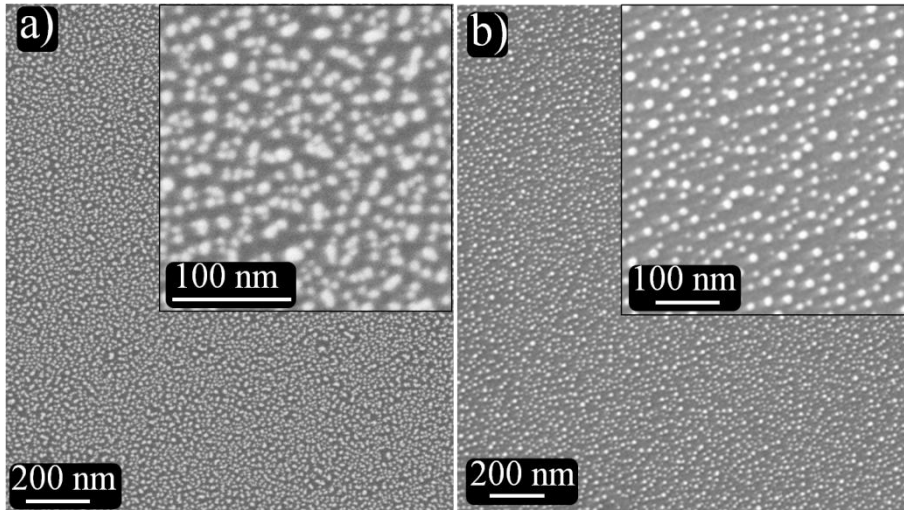


Fig. 3.3 Effect of annealing process: an Au film of recorded thickness 1 nm on Si substrate (a) before and (b) after annealing at 900 °C for 15 min.

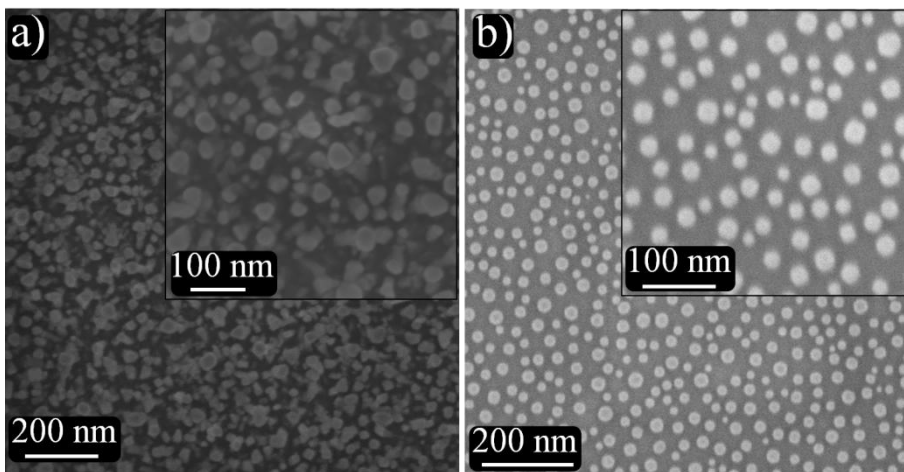


Fig. 3.4 Effect of annealing temperature: an Au film of recorded thickness 2 nm on Si substrate annealed for 15 min at temperatures (a) 800 °C and (b) 900 °C.

15 min (Fig. 3.4b). The nanoparticles are well separated from each other after annealing process. The film of recorded thickness 5 nm, which was annealed at 900 °C for 15 min, again showed the incomplete dewetting process of the islands (Fig. 3.5a). Whereas, the films annealed for 30 min at the same temperature showed the fully dewetted Au islands into particles of different shapes (Fig. 3.5b). By optimizing the annealing temperature and time for Au films of recorded thickness 1, 2, 3 and 5 nm the average particles sizes of $20(\pm 5)$ (Fig. 3.6a), $30(\pm 5)$ (Fig. 3.6b), $55(\pm 10)$ (Fig. 3.6c), and $105(\pm 40)$ nm (Fig. 3.6d) are obtained. A

large size distribution and irregular shape of the nanoparticles was observed when the films of higher thickness (≥ 5 nm) were used.

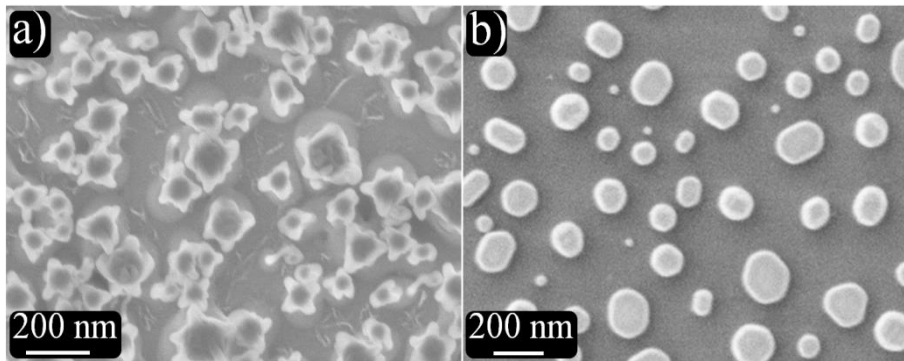


Fig. 3.5 Dependence of annealing time on film thickness: an Au film of recorded thickness 5 nm on Si substrate annealed at temperatures 900 °C for (a) 15 min and (b) 30 min.

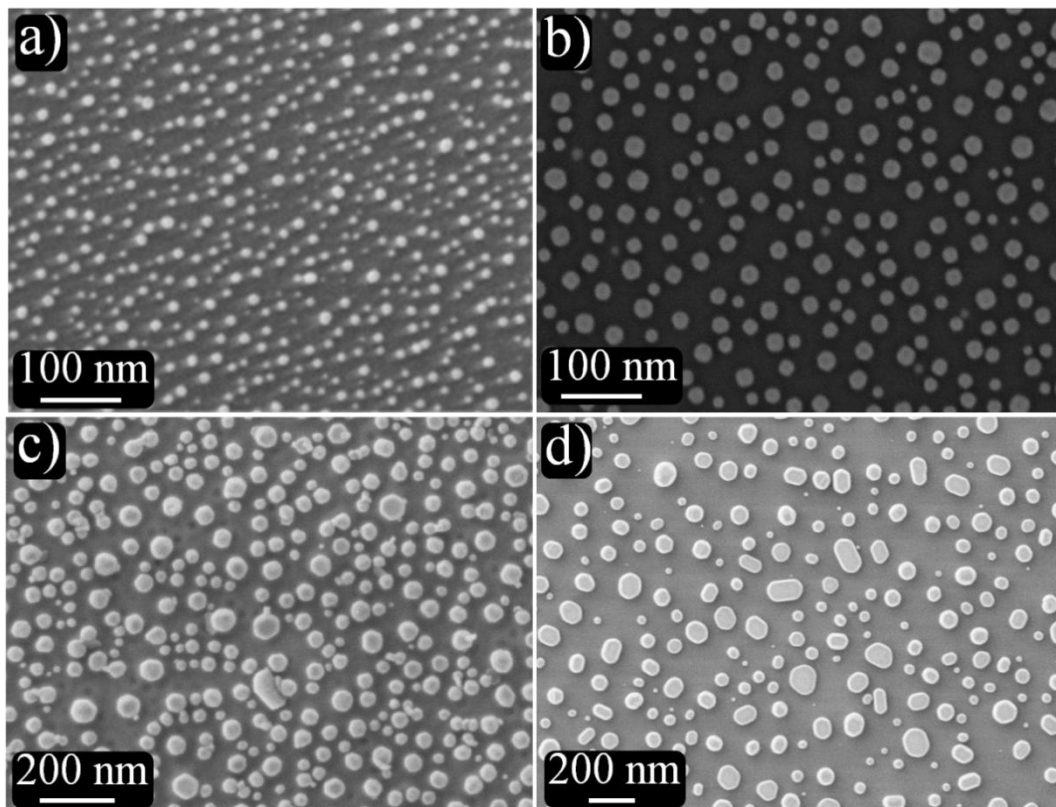


Fig. 3.6 FESEM micrographs of Au nanoparticles of different sizes (a) 20(± 5) nm (b) 30(± 5) nm, (c) 55(± 10) nm, and d) 105(± 40) nm.

3.2.2 Optimized Parameters for Growth of GaN Nanowires:

GaN NWs were synthesized using APCVD technique using the VLS process. The optimized Au nanoparticles of size ~30 nm on Si substrate were used for the NWs growth. We used Ga metal (99.999%, Alfa Aesar) as precursor, NH_3 (99.999%) as reactant gas, and a mixture of ultra high pure (UHP) Ar+ H_2 (5N) as carrier gases. The Si substrate with Au nanoparticles was kept upstream of a Ga droplet in a high pure alumina boat (99.999%) which was placed into a quartz tube. The quartz tube was evacuated to a base pressure of 10^{-3} mbar until it attained a temperature which was just below the growth temperature.

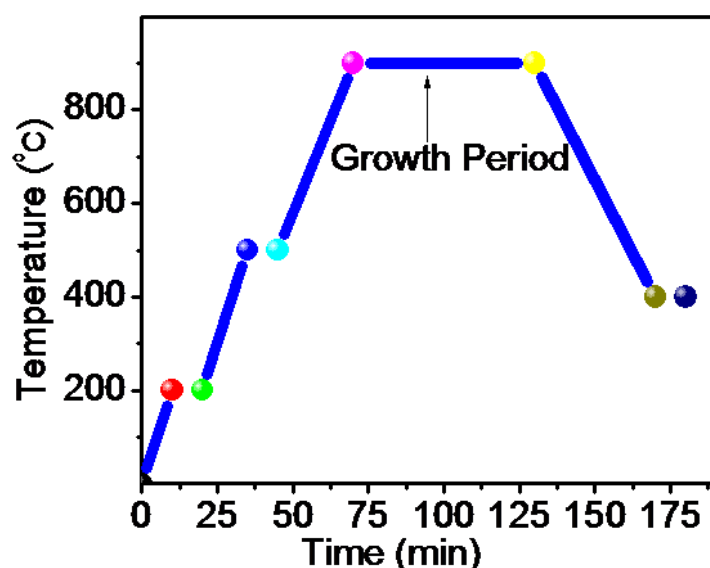


Fig. 3.7 Temperature Vs time plot for the VLS growth of GaN NWs.

The pressure of the quartz tube was brought back to atmospheric pressure by filling the tube with carrier gas. The flow of the carrier gas and the temperature at which the gas flow was started, were chosen such that the pressure of the tube reached the atmosphere exactly when the tube attained growth temperature. The growth parameters of temperature, time and distance between the substrate and source were optimized to grow the NWs. The time Vs temperature plot of the growth process is shown (Fig. 3.7). The temperature of the quartz tube was slowly raised to an optimized growth temperature of $900\text{ }^\circ\text{C}$ with $16\text{ }^\circ\text{C min}^{-1}$ ramp rate.

The NWs were grown for 60 min growth time by purging 10 sccm of NH_3 reactant gas and 20 sccm of Ar carrier gas.

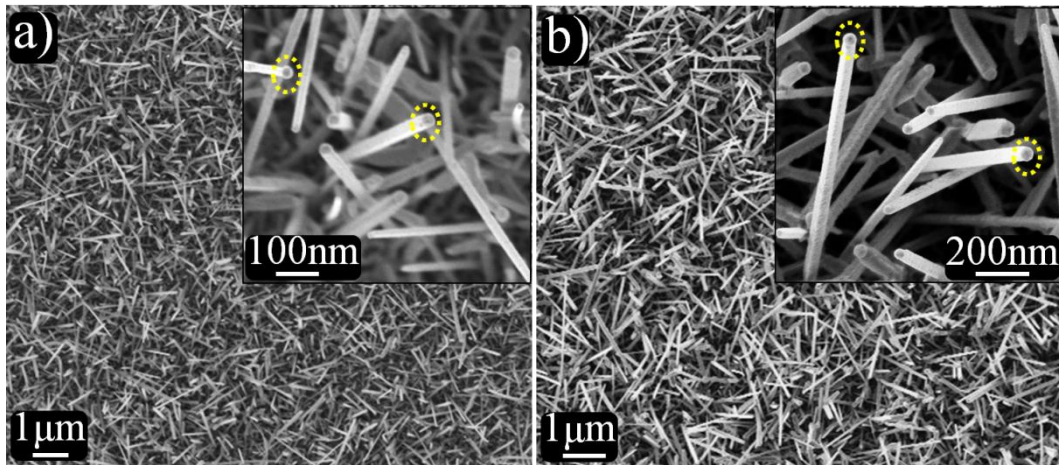


Fig. 3.8 FESEM micrographs of GaN NWs of sizes (a) $40(\pm 5)$ nm, and (b) $60(\pm 5)$ nm grown under optimized growth parameters in the VLS process. Insets show the high magnification micrographs of GaN NWs with catalyst particles (dotted circles) at the tips of NWs.

Morphological analysis of the as grown NWs shows that the NWs have smooth and homogeneous surface morphology and uniform size distribution with diameter of $40(\pm 5)$ nm is achieved using the Au catalyst particle size of $30(\pm 5)$ nm (Fig. 3.8a). The growth rate is found to be $3\mu\text{m h}^{-1}$. The particle at the tip shows that the NWs are grown in the VLS process (inset in Fig. 3.8a). The reproducibility and size selective growth of the NWs are studied by choosing the Au catalyst particle size of $55(\pm 10)$ nm. The NWs with uniform shape and size distribution of $60(\pm 5)$ nm (Fig. 3.8b) are obtained.

3.2.3 Role of Substrate:

Generally, the NW growth orientation and alignment depend on the symmetry and lattice match between the substrate and GaN.^[11-13] However, the growth conditions such as temperature, catalyst and precursor fluxes strongly influence the substrate epitaxy.^[12,13] The influences of the substrate material on the alignment and shape of GaN NW are studied by growing the NWs on different substrate surfaces, namely, Si(100), Si(111), *c*- Al_2O_3 , *c*-

AlN(60nm)/Si(111), Graphene/SiO₂/Si and SiO₂/Si. GaN NWs, grown on the Si(100) substrates have triangular shape and randomly aligned (Fig. 3.9a), while the NWs grown on the Si(111) substrates also have triangular shape but aligned from the substrate (Fig. 3.9b). No aligned growth of the NWs is observed on *c*-Al₂O₃ (Fig. 3.10a) and *c*-AlN(60nm)/Si(111) (Fig. 3.10b) substrates. Moreover, the shape of the NWs is triangular on both the substrates as observed in case of samples grown on Si.

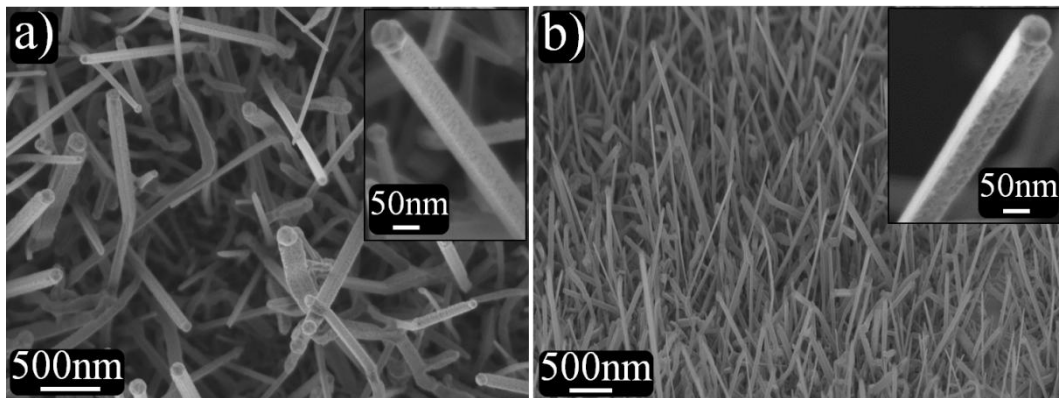


Fig. 3.9 FESEM micrographs at 54° tilt view of GaN NWs grown on substrates (a) Si(100), and (b) Si(111). Insets show the high magnification micrographs of triangular shaped GaN NWs with catalyst particles at the tips.

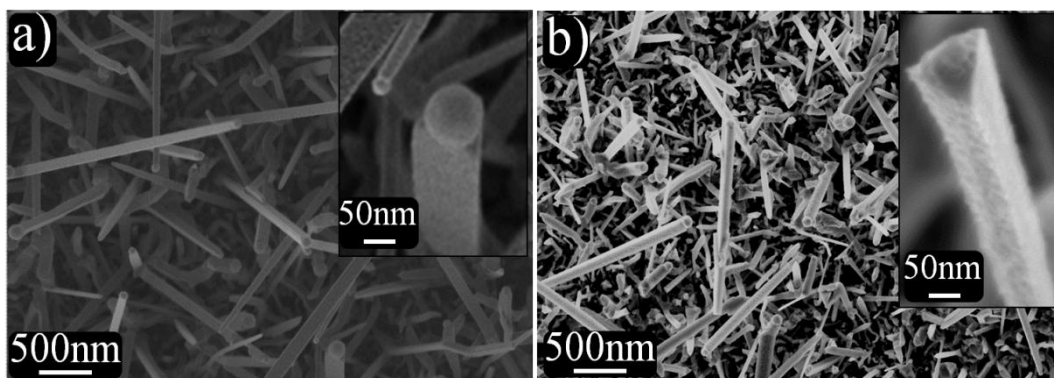


Fig. 3.10 FESEM micrographs of GaN NWs grown on substrates (a) *c*-Al₂O₃, and (b) AlN(60nm)/Si(111). Insets show the high magnification micrographs of triangular shaped GaN NWs with catalyst particles at the tips.

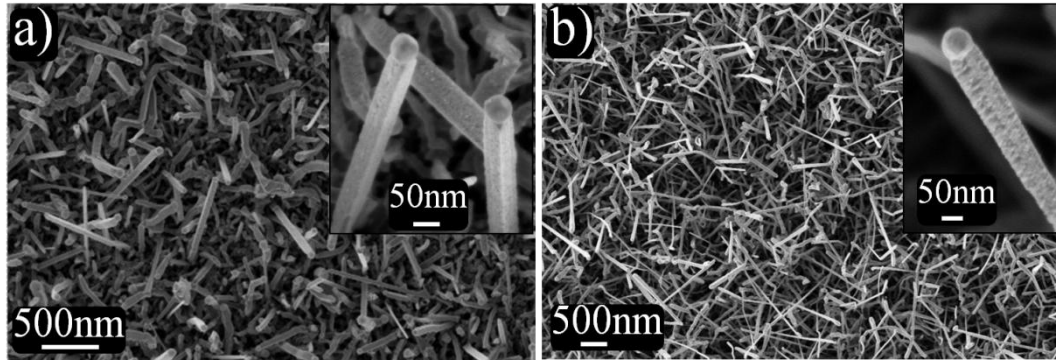


Fig. 3.11 FESEM micrographs of GaN NWs grown on substrates (a) Graphene/SiO₂(300nm)/Si, and (b) SiO₂(300nm)/Si. Insets show the high magnification micrographs of triangular shaped GaN NWs with catalyst particles at the tips.

Usually, growth on *c*-Al₂O₃ substrate and *c*-AlN buffer layer results in the *c*-axis oriented GaN due to its *c*-plane epitaxy and hence the resultant NWs grow with hexagonal cross-section. However, in the present study the NWs shape is independent of the substrate material and its crystallographic orientation. This suggests that the growth conditions and the Au catalyst particle (in the VLS growth) played major roles on the shape and alignment of NWs.^[12,13]

The role of template and surface oxide on shape and alignment of the NWs are also studied by growing the NWs on single layer graphene (SLG) and SiO₂ (300 nm) deposited on Si substrates. High quality SLG grown by hot-filament CVD technique, was used to grow the GaN NWs.^[14] The NWs grown on SLG template are smooth and having a uniform shape (triangular) with small growth rate (Fig. 3.11a). On the other hand, the NWs grown on SiO₂ are rough with non-uniform surface morphology, and having large size distribution with large growth rate (Fig. 3.11b). Generally, growth rate, size and surface morphology of NWs are strongly affected by surface oxide layer on substrate. Thus, GaN/SiO₂ interface and the diffusion of oxygen atoms in to GaN NW during the growth on SiO₂/Si substrate may be responsible for the observed non-uniform surface morphology of the NWs. On the other

hand, the oxide interface and oxygen diffusion are avoided on graphene template in case of growth on graphene/SiO₂(300nm)/Si substrate.

3.3 Influence of Oxygen impurity on GaN Nanowires

The effect of oxygen on morphological, structural and optical characteristics of the GaN NWs is studied by growing the NWs under the controlled oxygen impurity of different concentrations during the growth.^[15] The similar growth conditions, except for the O concentration, with optimized growth parameters were maintained for all the samples including the Au catalyst particle size of ~30 nm (Fig. 3.6b). Incorporation of O was carried out at different oxygen partial pressures in the range of 1.2×10^{-4} to 1.3×10^2 Torr by varying the base pressure of the growth chamber (quartz tube) and gas purity of NH₃ and Ar. For O rich condition, NWs were grown at an oxygen partial pressure of 1.3×10^2 Torr ($\sim 2 \times 10^5$ ppm O₂; sample R1) by purging high pure NH₃ (3N) and commercial Ar gases without evacuating the chamber. For O reduced condition, two sets of NW samples were grown at oxygen partial pressures of 1.2×10^{-1} Torr (~ 150 ppm O₂; sample R2) and 1.2×10^{-4} Torr (< 1 ppm O₂; sample R3) by purging ultra high pure NH₃ (5N) and UHP Ar+H₂ (5N), respectively. Another set of samples at an oxygen partial pressure of 1.2×10^{-4} Torr (< 1 ppm O₂; sample R4) were also grown using catalytic Au nanoparticles of different average size than that used in previous case for controlling size under reduced amount of O.

3.3.1 Morphological Variations:

Morphological features of the as grown samples were examined using field emission scanning electron microscope (FESEM, SUPRA 55 Zeiss). The NWs grown under O rich condition (R1) show quite rough and non-uniform surface morphology with large size distribution (Figs. 3.12a,b) and large growth rate ($17 \mu\text{m h}^{-1}$). In oxygen reduced condition, NWs of sample R2 show smooth but non-uniform size distribution (Fig. 3.12c) while that of

sample R3 shows smooth and homogeneous surface morphology (Fig. 3.12d) and uniform size distribution all over the sample with a reduced growth rate ($3 \mu\text{m h}^{-1}$). The particle at the tip shows that the NWs are grown in the VLS process (Fig. 3.12d). Although all the three sets of samples (R1, R2 and R3) were grown with similar sized catalyst particles, large variation in the diameter of the NWs of the three samples is observed. The NWs of sample R1 have a large diameter and non-uniform sizes (50–150 nm) and non-uniform surface morphologies (Figs. 3.12a,b), whereas the diameter of the NWs of sample R2 (Fig. 3.12c) is found to be significantly smaller than that of R1 but with non-uniform sizes (40–90 nm).

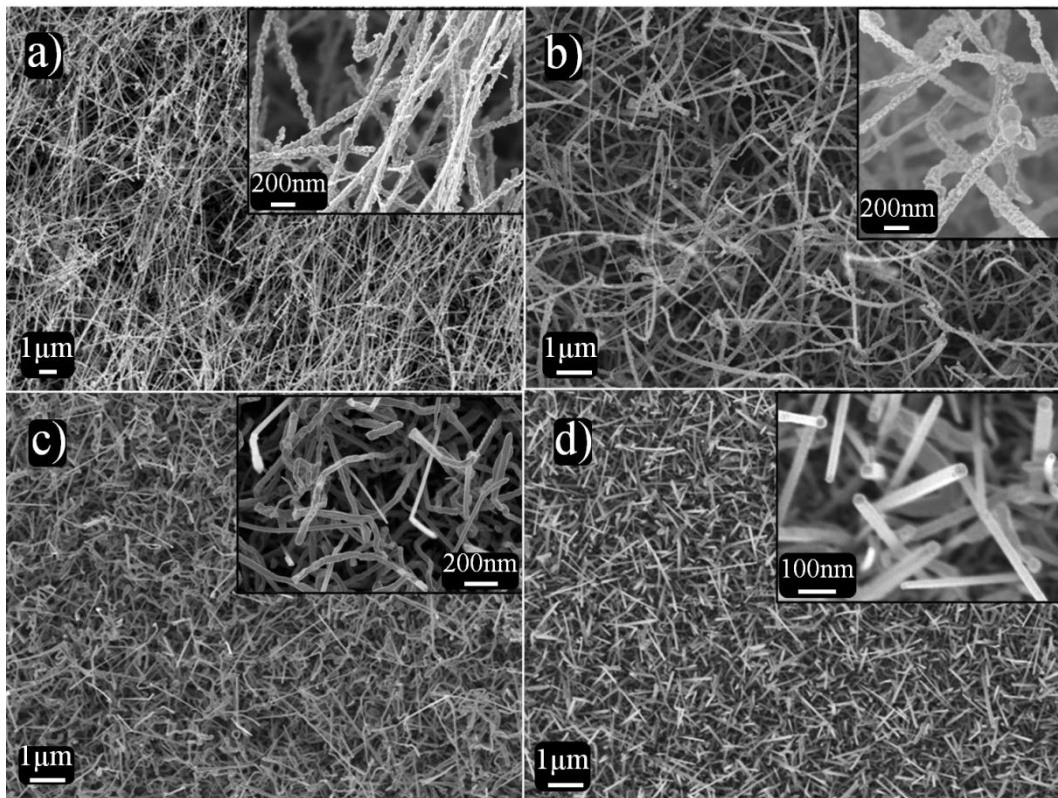


Fig. 3.12 Typical FESEM images of GaN NWs. (a and b) NWs of sample R1 showing (insets) quite rough and nonuniform surface morphology in the respective high magnification images. (c) NWs of sample R2 shows smooth but nonuniform morphology in the respective high magnification image. (d) NWs of sample R3 having uniform diameter and surface morphology along the wire shown in the high magnification image (inset). Inset, nanoparticles at the tip of the NWs are clearly seen.

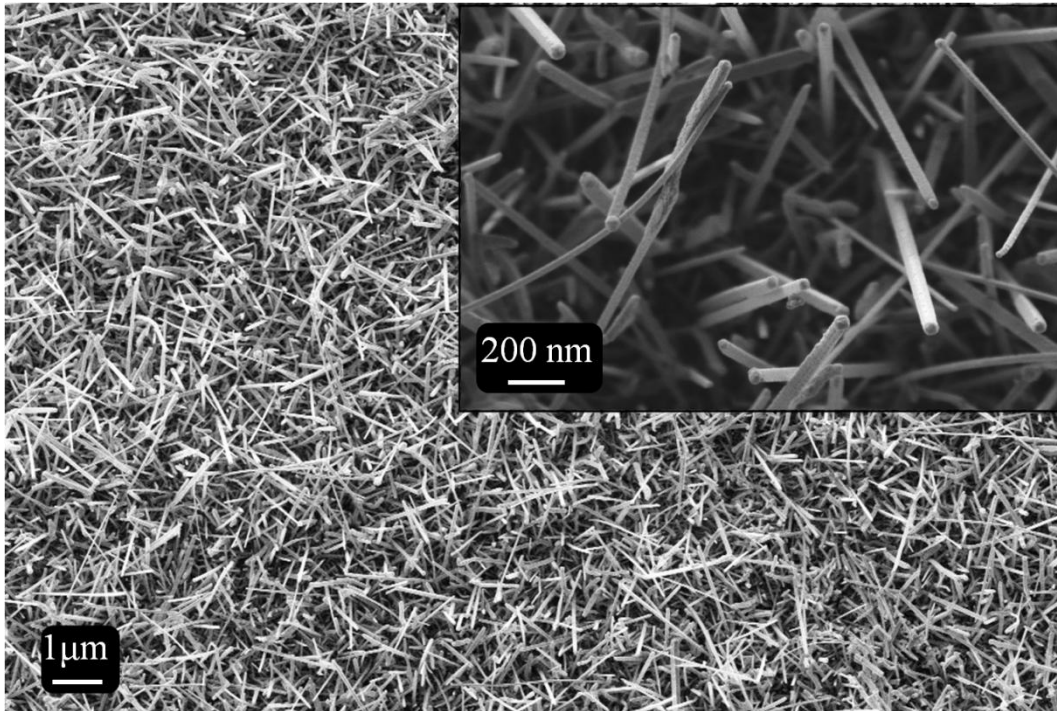


Fig. 3.13 Typical FESEM images of GaN NWs grown under oxygen reduced conditions (sample R4). Inset shows the high magnification image of NWs with uniform shape, surface morphology and size distribution of $55(\pm 5)$ nm.

We have also studied morphology of the NWs grown at different oxygen partial pressures between 10^{-4} and 90 Torr (~ 1 –100 ppm O_2) showing non-uniformity similar to those of R1 and R2.^[15] Surface morphology along the wires, however, was improved compared to that of the sample R1. In the sample R3, the diameter of the NWs exactly follows the size of the catalyst particle at the tip. NWs having uniform shape and size distribution $\sim 40(\pm 5)$ nm with homogeneous surface morphology are observed along the wire, in the entire sample (Fig. 3.12d). The reproducibility of the uniform shape, size distribution and surface morphology of the sample R3 are improved in the O reduced condition than morphology of the sample R3 are improved in the O reduced condition than those found for the samples (R1 and R2) grown under O rich condition. Au nanoparticles of size distribution $\sim 40(\pm 5)$ nm were used for demonstrating reproducibility and size selective growth of NWs, sample R4, of bigger diameter $55(\pm 5)$ nm with uniform shape and surface morphology

(Fig. 3.13). Deposition conditions, same as sample R3, were used for this purpose. The uniform size and morphology of the NWs might be a result of the controlled and thermodynamically stable growth of the crystallites with specific crystalline orientation by the incorporation of Ga and N species in the reduced impurity condition.

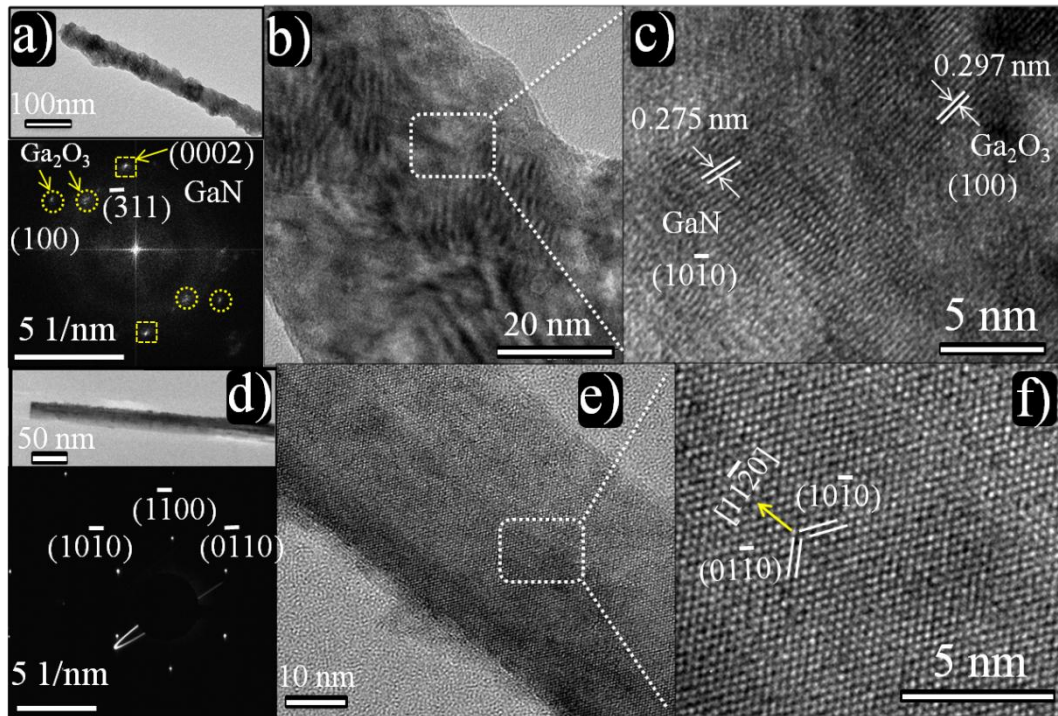


Fig. 3.14 Typical NW grown under O rich condition (sample R1) shows (a) an irregular surface morphology. FFT diffraction spots corresponding to the TEM micrograph (outset) reveal the presence of phases of GaN and Ga₂O₃. (b and c) HRTEM images of NWs. (d) A typical NW grown under O reduced conditions (sample R2) with SAED pattern (outset), indexed to wurtzite GaN of the zone axis along [0001]. (e and f) HRTEM image of the NW (Fig. 3.14d) having nonpolar planes (10 $\bar{1}$ 0) and the growth direction along [11 $\bar{2}$ 0].

3.3.2 Structural and Compositional Variations:

In the HRTEM morphological analyses, a typical NW of the sample R1 (grown under O rich condition) shows an irregular surface morphology (Fig. 3.14a). FFT spots corresponding to HRTEM micrograph of the NW (outset of Fig. 3.14a) reveal the presence of mixed phases of GaN and Ga₂O₃. The diffraction spots enclosed by dotted circles are indexed to {100} and { $\bar{3}11$ } planes corresponding to monoclinic Ga₂O₃ phase and spots enclosed by

dotted squares are indexed to $\{0002\}$ planes of wurtzite GaN phase. The HRTEM image of the NW shows non-uniform contrast (Fig. 3.14b) which may originate from variation in thickness along the NW and barely seen for lattice fringes. Lattice fringes with d -spacing 0.297 nm and 0.275 nm corresponding to $\{100\}$ planes of Ga_2O_3 phase and $\{10\bar{1}0\}$ planes of GaN phase, respectively, are observed in the magnified view (Fig. 3.14c) of the high resolution image. We may like to state here that oxide phase is highly inhomogeneous in the NWs. It is observed that (100) planes are presumably grown over nonpolar planes ($10\bar{1}0$) of GaN. However, the oxide phase was not observed along the NW length. The NWs of the sample R2 have a uniform rod like shape (Fig. 3.14d) and the corresponding SAED pattern shows perfect single crystalline feature (outset of Fig. 3.14d). The diffraction spots are indexed to $[0001]$ zone axes of wurtzite GaN. The NW has nearly uniform contrast (Fig. 3.14e) except for one of the edges of the wire where a thin amorphous layer is observed which may be due to possible formation of an oxide overlayer on the surface of NW. Magnified view of lattice resolved micrograph (Fig. 3.14f) shows an interplanar spacing of 0.276 nm corresponding to nonpolar $\{10\bar{1}0\}$ planes of wurtzite GaN and growth direction of the NW is determined to be along $[11\bar{2}0]$.

A typical NW of the sample R3 grown under O reduced conditions shows a perfect rod like shape with uniform surface morphology (Fig. 3.15a) and has an Au catalyst particle at the tip. The SAED pattern (Fig. 3.15b) reveals that the NW is a single crystalline wurtzite phase of GaN with zone axes $[0001]$. A sharp interface between GaN NW and Au catalyst particle is seen in high resolution electron micrograph (Fig. 3.15c). An interplanar spacing of 0.276 nm, shown in the magnified view (Fig. 3.15d), corresponds to the nonpolar $\{10\bar{1}0\}$ planes of wurtzite GaN. The growth direction of the NW is found to be along $[11\bar{2}0]$ direction, similar to that of sample R2.

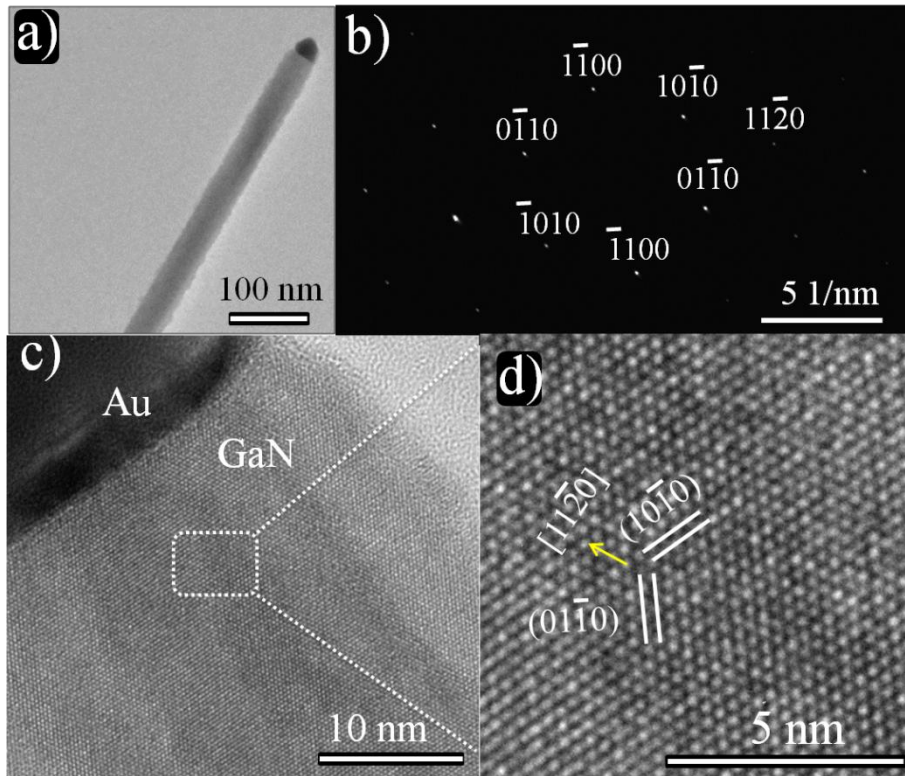


Fig. 3.15 (a) Low magnification TEM micrograph of a typical GaN NW grown under oxygen reduced conditions (sample R3). (b) SAED pattern of the NW, indexed to wurtzite GaN with zone axis along $[0001]$. (c) HRTEM image collected near the tip of the NW having Au nanoparticle. (d) Magnified view of the HRTEM image shows the NW having nonpolar planes $(10\bar{1}0)$ and the growth direction along $[11\bar{2}0]$.

The O incorporation into the NW may occur through two possible ways. It may occur through liquid/solid interface (Au-Ga/GaN) while the NW grows in the VLS process and O incorporation may occur directly on the active nonpolar surfaces of the NW (Fig. 3.16). In the O rich condition, when the NW grows along a nonpolar direction $[11\bar{2}0]$, there is a large tendency of incorporation of O along with N at liquid/solid interface. Thus, in the extreme limit of impurity incorporation a supersaturation mixture of nitride and oxide phases might have formed. The presence of two phases might have brought the instability in the uniformity of NW by introducing fluctuations due to thermodynamically non-equilibrium growth of the different atomic planes during simultaneous incorporation of N and O species. As a result, NWs tend to form non-uniform morphology along the axis of the wire.

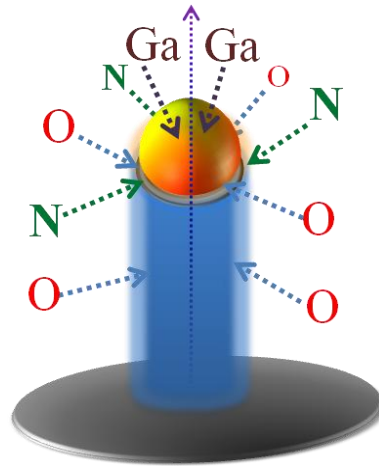


Fig. 3.16 Schematic view of the possible O incorporation pathways, along with Ga and N during the VLS growth of GaN NW.

Although the two nonpolar planes, $(11\bar{2}0)$ and $(10\bar{1}0)$, have similar surface energies,^[16] O atoms have strong tendency to segregate on the $(10\bar{1}0)$ planes.^[17] In the direct incorporation of O into $(10\bar{1}0)$ surfaces, O replaces the N and forms stable defect complexes in their stability order $2(O_N)$, $V_{Ga}-3(O_N)$ and finally it supersaturates to form Ga_2O_3 at the extreme limits of Ga and O.^[17,18] On further incorporation, O mobilizes to a new place and the process of defect formation and oxide overlayer formation repeat. As a result, NWs become thick and have a rough surface morphology with an oxide over layer. In order to confirm the variations in O and N concentrations in the NWs, we have carried out EELS studies.

The EELS spectra of NWs of the three samples are analyzed by collecting the *K*-edge emission of N and O. The spectra show a drastic variation in the fine structures of N-*K* and O-*K* edges (Figs. 3.17a,b). All the *K*-edge spectra are background subtracted on the basis of power law energy dependence (AE^{-r}) .^[19] A clear splitting in the fine structure with poor intensity of N-*K* edge spectra (Fig. 3.17a) is observed for the NW of sample R1, grown under O rich conditions, with irregular surface morphology. The fine structures of N-*K* edges from

the NWs of samples R2 and R3, grown under the O reduced condition are broadened and show the increase in N concentration. The O-*K* edge spectra follow reverse trend for samples

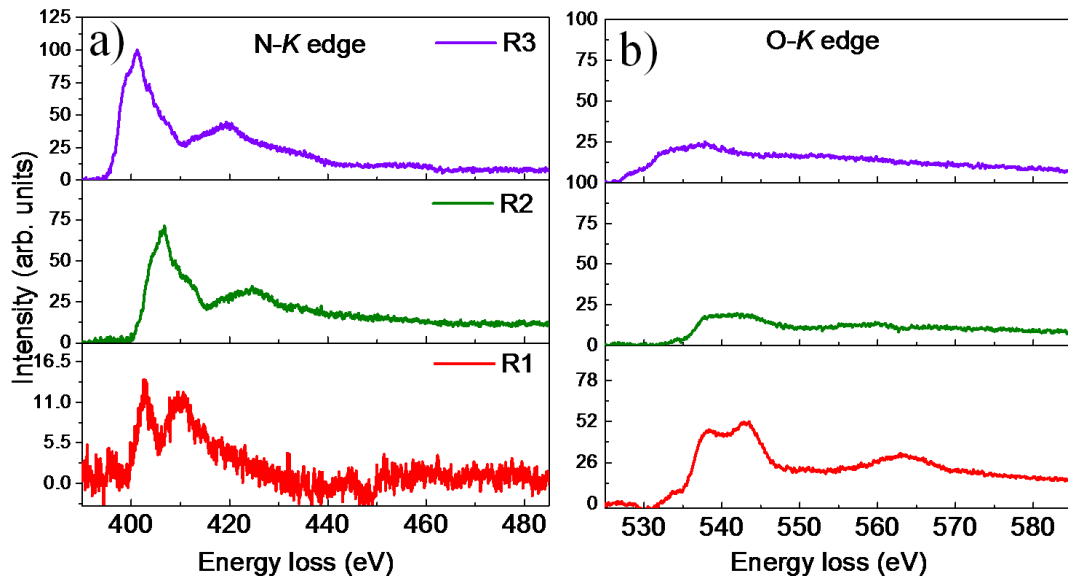


Fig. 3.17 EELS spectra of GaN NWs of the samples R1 and R2, R3 grown under O rich and O reduced conditions, respectively. (a) Background subtracted N-*K* edge of NWs. (b) Corresponding O-*K* edge of NWs of the samples R1, R2 and R3.

R1 to R3. The O-*K* edge spectra obtained from the NWs of samples R2 and R3 (Fig. 3.17b) are broad and weak while that of the NWs of sample R1 (Fig. 3.17b) shows clear splitting in fine structure and intense peaks. The rise and fall in the intensity of the O-*K* edge and the N-*K* edge, respectively, for the NWs of sample R1 are presumably due to the O substitution for N in the GaN during the growth of samples in O rich conditions.

The variation in the N to O concentration with respect to NW surface morphology is investigated by obtaining the electron energy loss *K*-edge spectra of N and O, from two different positions of the each NW of the samples R1 and R3 grown under O rich and O reduced conditions, respectively. Fig. 3.18a shows the power law energy dependent background subtracted *K*-edge spectra of N and O obtained from the position 1 (middle region of the NW, thin and rough morphology) and position 2 (tip region of the NW, thick and rough morphology) on the NW of the sample R1. Fig. 3.18b shows background

subtracted K -edge spectra of N and O obtained from the position 1 (middle region of the NW) and position 2 (close to one end of the NW) on the NW of the sample R3.

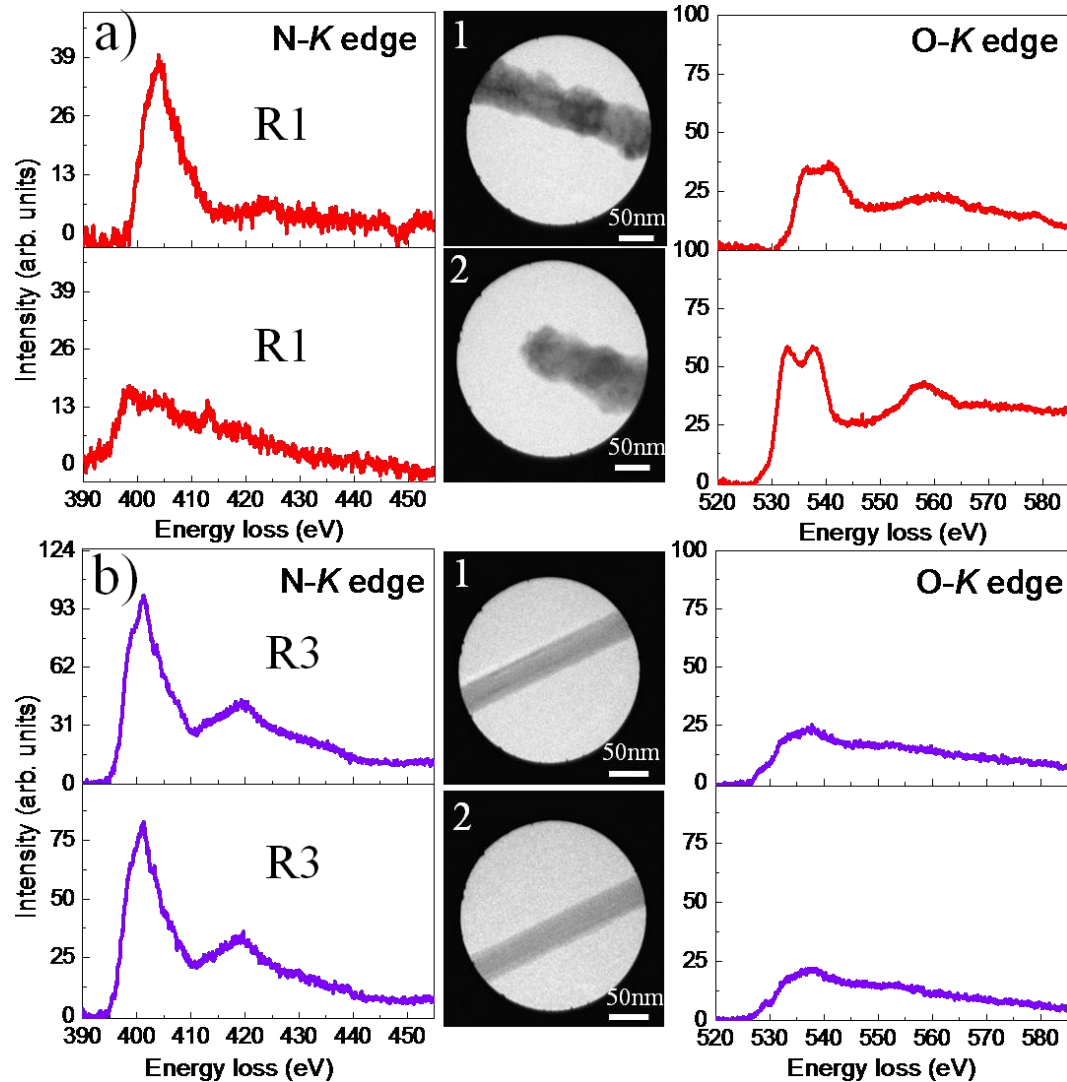


Fig. 3.18 (a) EELS spectra of background subtracted K -edges of N and O obtained from the position 1 (middle region of the NW with thin and rough morphology) and position 2 (tip region of the NW with thick and rough morphology) on the NW of the sample R1 grown under O rich conditions. (b) EELS spectra of background subtracted K -edges of N and O obtained from the position 1 (middle region of the NW) and position 2 (close to one end of the NW) on the NW of the sample R3 grown under O reduced conditions.

The ratio of two elemental concentrations can be obtained by calculating the core loss integral intensity of K -edge, $I_K(\beta, \Delta)$ for a collection-semi angle β over an energy range Δ

beyond threshold and a partial scattering cross-section for that particular threshold edge $\sigma_K(\beta, \Delta)$.^[19,20] Therefore the ratio of concentrations for N (n_N) and O (n_O) is given by,

$$\frac{n_N}{n_O} = \frac{I_{KN}(\beta, \Delta) \sigma_{KO}(\beta, \Delta)}{I_{KO}(\beta, \Delta) \sigma_{KN}(\beta, \Delta)}$$

The core loss partial scattering cross-sections for K -shells of N and O, $\sigma_{KN}(\beta, \Delta)$ and $\sigma_{KO}(\beta, \Delta)$, respectively, are calculated using SIGMAK3 program which is based on hydrogenic model.^[20] The core-loss intensity of K -shells for N and O, $I_{KN}(\beta, \Delta)$ and $I_{KO}(\beta, \Delta)$, respectively, are calculated by integrating the area under the curve over an energy $\Delta=50$ eV above the corresponding thresholds.

The concentration ratio of N to O (n_N/n_O) was measured at the position 1 (Fig. 3.18a) middle region of the NW of the sample R1 is found to be 0.20. Whereas, the ratio is reduced to 0.09 for the spectra collected at position 2, tip region of the NW with thick and rough surface morphology. The data shows that the inhomogeneous incorporation of O into the crystalline planes of GaN. For the NW of sample R3 (Fig. 3.18b), n_N/n_O is measured at positions 1 (middle) and 2 (end), of the NW and are found to be 1.21 and 1.19, respectively, showing dramatic reduction in O concentration and homogeneous incorporation of N into crystalline planes of GaN.

3.4 Optical Characteristics

3.4.1 Raman Spectroscopic Study:

GaN crystallizes in a wurtzite structure (space group $C_{6v}^4-P6_3mc$) with two formula units per primitive cell.^[21] According to factor group analysis at the Γ point of the Brillouin zone, eight sets of phonon normal modes, namely $2A_1+2E_1+2B_1+2E_2$ are possible. Among them, one set of A_1 and E_1 modes are acoustic, while the remaining six modes, namely $A_1+E_1+2B_1+2E_2$ are

optical modes. The A_1 and E_1 are polar modes i.e., the interaction of the vibration with the long-range Coulomb field leads to energy differences between phonons polarized longitudinally (LO) and transverse (TO) to the direction of propagation of the phonon. The A_1 and E_1 modes are therefore split into LO and TO modes. The atomic vibrations in wurtzite GaN for zone centre phonons are shown schematically in Fig. 3.19a.^[22]

A typical Raman spectrum of a single GaN NW of sample R3 dispersed on a metallic [crystalline Cu(100)] substrate shows (Fig. 3.19b) the peaks at 144, 252, 421, 537, 568, and 725 cm^{-1} . The wave numbers 144, 537, 568, and 725 cm^{-1} are found to match with E_2^L , $A_1(\text{TO})$, E_2^H and $A_1(\text{LO})$ phonon modes, respectively, of the wurtzite GaN.^[23] Additional peaks at 252, and 421 cm^{-1} correspond to zone boundary (ZB) phonon modes of GaN which are non-zone centre phonons appear due to the finite crystallite size effects. The broad peak in between E_2^H and $A_1(\text{LO})$ modes is possibly due to surface optical (SO) phonons.^[23] Generally the intensity, position and FWHM of the $A_1(\text{LO})$ phonon peak are strongly influenced by the free carrier concentration (electrons or holes) in the GaN as a result of the LO phonon-plasmon coupling.^[22] A sharp intense peak of $A_1(\text{LO})$ mode of single GaN NW (sample R3), shows that a very weak phonon-plasmon coupling. This suggests the high resistive nature of the O-reduced GaN NW due to the reduction in background electron concentration. Raman spectra for GaN NWs of sample R1, from both ensemble and single NWs were studied (Fig. 3.19c). The peak around 305, and 521 cm^{-1} in ensemble NWs (Fig. 3.19c), which are absent in single NW spectra, correspond to the ZB_{Si} and optical phonon modes, respectively of Si substrate on which NWs are grown. The peaks at 252, 421, 569 and 730 cm^{-1} correspond to ZB, and symmetry allowed E_2^H and $A_1(\text{LO})$ phonon modes of GaN, respectively. The $A_1(\text{LO})$ mode is blue shifted by 5 cm^{-1} with an asymmetric broadening and a reduction in the peak intensity, suggesting strong coupling between LO phonons and electron carrier generated by O_N and V_N in GaN.^[22,24]

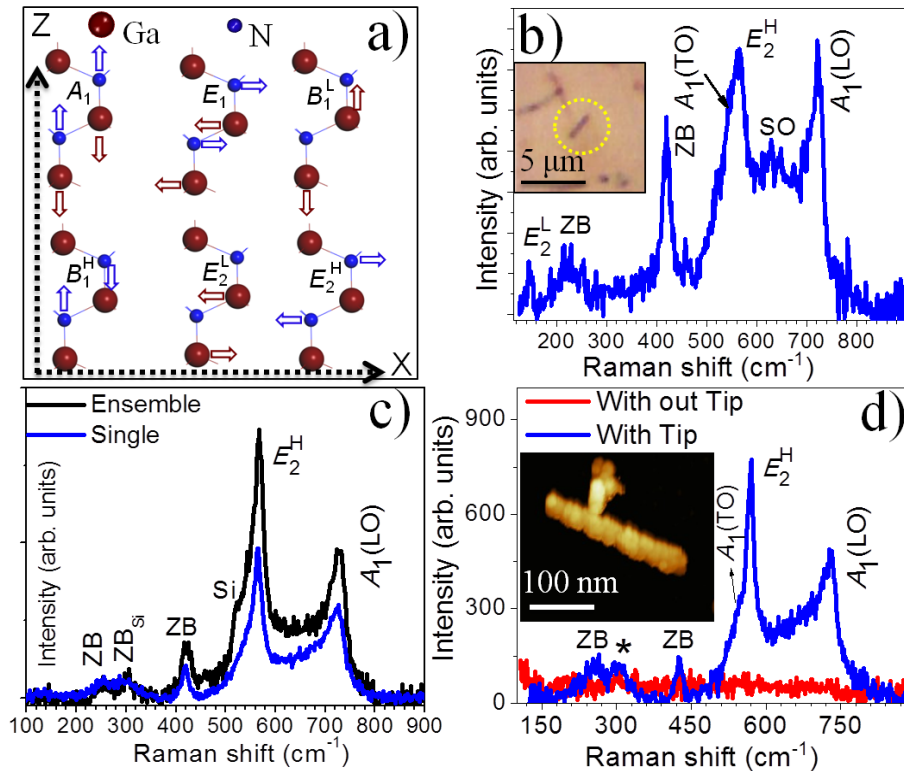


Fig. 3.19 (a) Schematic view of the atomic vibrations in wurtzite GaN for zone centre phonons.^[22] Arrow marks indicate the direction of vibrations. (b) A typical Raman spectrum of single GaN NW of sample R3 with low O concentration. Inset shows the optical image of a single NW (encircled) on Cu(100) substrate (c) Raman spectra of ensemble and a single GaN NW of O rich sample R1. (d) TERS spectra of a single GaN NW of sample R1 with and without TERS tip. AFM image of the NW is shown in the inset. The peak pointed out by star mark (*) corresponds to GaO_xN_y phase.

However, the spectra did not show any peak corresponding to crystalline phase of oxide (Ga_2O_3) because of its rare and inhomogeneous presence in the NWs. In order to observe the local chemical changes on single NWs, TERS spectrum using the evanescent field of Au nanoparticle attached SPM tip on a single NW (sample R1) was also recorded (Fig. 3.19d). TERS spectrum shows symmetry allowed modes at 538, 569 and 729 cm^{-1} corresponding to the $A_1(\text{TO})$, E_2^H and $A_1(\text{LO})$ phonon modes, respectively, of wurtzite GaN phase.^[23] The ZB modes are also observed at 252 and 421 cm^{-1} . A tiny peak around 315 cm^{-1} may be assigned to a oxy-nitrides (GaO_xN_y) phase.^[25] Inhomogeneous inclusion of O may primarily be responsible for not identifying symmetry allowed modes of Ga_2O_3 which is found in our

HRTEM study (outset of Fig. 3.14a). The absence of oxide phase shows that O incorporation in GaN may be in the form of native defect of O_N or its complexes with V_N , contributing to generation of electron carrier in the NW.^[22,24] As a matter of fact, the asymmetry in the $A_1(\text{LO})$ mode is because of strong coupling between LO phonons and electron carrier generated by O_N and V_N in GaN, as discussed in case of normal Raman study in single NW (Fig. 3.19c).

3.4.2 Photoluminescence Study:

Optical quality of the GaN NWs of three sets of samples (R1, R2 and R3) grown under O rich and O reduced conditions was investigated using PL spectroscopy. A UV laser of 325 nm wavelength was used to excite the NWs and the emission spectra were recorded at 80 K. The luminescence from the NWs of sample R1 (Fig. 3.20), grown under O rich conditions, shows a broad emission around 2.0-2.3 eV which may be attributed to the YL band.^[24,26] A weak emission around 3.27 eV is also observed. In the GaN, oxygen easily substitutes the N (O_N) due to low defect formation energy and forms a shallow donor level.^[2] The Ga vacancies (V_{Ga}) are deep acceptors and forms complexes with O shallow donors as $V_{\text{Ga}}O_N$, which possibly causes the emission of the YL band around 2.2 eV.^[24] In the O rich conditions particularly with concentration above 10^{20} cm^{-3} , the O incorporation increases the $V_{\text{Ga}}O_N$ complex formation leading to an increase in the intensity of the YL band. In the O deficient condition, intensity of the YL band decreases drastically in the luminescence spectra of NWs of sample R2 while it vanishes in the collected luminescence spectra from NWs of sample R3. A second broad peak around 3.27 eV in the spectra of sample R1 (Fig. 3.20) is attributed to the recombination of neutral donor-acceptor pair (DAP; D^0A^0), due to the transition from a shallow donor state of nitrogen vacancy (V_N) to a deep acceptor state of V_{Ga} . The DAP peak is red shifted by 10 meV which may be the result of defects present in the NW.^[27] Emission due to excitons bound to neutral donors (D^0X_A), which is commonly

peaked at 3.47 eV, is completely suppressed.^[24] This shows that the optical quality of NWs of the sample R1, grown under O rich condition, is degraded.

The luminescence spectrum of NWs of the sample R2 (Fig. 3.20) shows strong emission around 3.0-3.5 eV with a significant reduction in the YL band compared to that of sample R1. The spectrum consists of a free exciton (FE) emission around 3.51 eV along with its LO phonon replica (FE-LO) around 3.385 eV.^[24] A peak corresponding to DAP (D^0A^0) type transition around 3.27 eV along with its second order LO (2LO) phonon replica, D^0A^0 -2LO at 3.1 eV and a blue luminescence (BL) around 2.85 eV are also observed.^[27] The NWs grown under O reduced conditions of the sample R3 emitted a strong band of D^0X_A at 3.47 eV (FWHM \sim 130 meV) along with a 2LO phonon replica of excitons bound to neutral donors (DBE)-2LO band around 3.31 eV. The DBE band may appear because of the presence of either the intrinsic V_N or the residual O donors (O_N) formed below the conduction band.^[24]

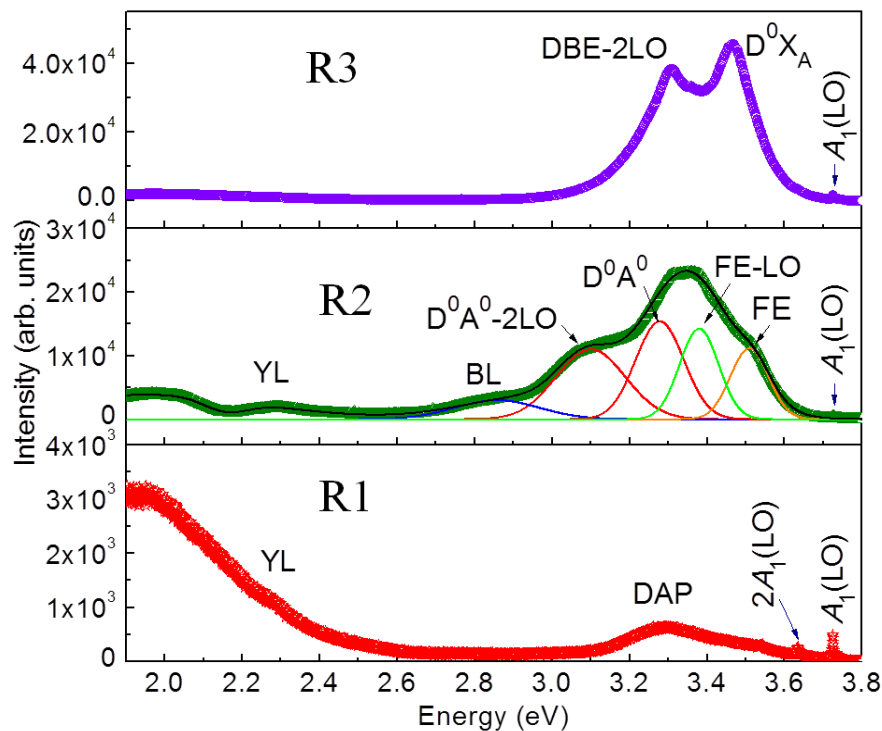


Fig. 3.20 Typical PL spectra of GaN NWs of the samples R1, R2 and R3, collected in the energy range 2.0 - 3.8 eV, at 80 K.

Surprisingly we have observed the 2LO coupling in some of the PL spectra while coupling with 1LO mode is absent. The absence of 1LO coupling is not very clear and it may be due to the breakdown of symmetry in the resonant condition. The absence of the YL band and strong emission of DX band in luminescence spectra of NWs grown under the O reduced condition are the implication of high optical quality GaN phase.

3.5 Waveguide Property:

We have also used these GaN NWs, grown under O reduced conditions, as waveguides for observing far field excitation-emission process. Very often we observe bright violet emission spots corresponding to the D^0X_A band around 3.47 eV (357 nm with FWHM 27 nm) of PL emission for R3 sample (Fig. 3.21).

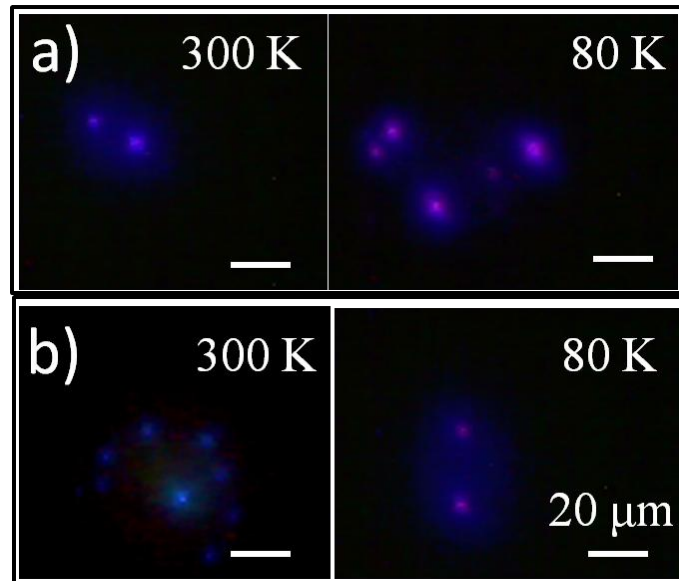


Fig. 3.21 Typical optical images of far field bright violet emission spots at 300 and 80 K on the NWs of sample (a) R3 and (b) R4. Emission spots are coming out of the ends of the NWs through the available open space while other ends are at the excitation with laser light.

Multiple violet emission spots from R3 (Fig. 3.21a) and R4 (Fig. 3.21b) samples at different places on the NWs grown area were recorded at room temperature (300 K) as well as 80 K, respectively. GaN is reported to have a very high refractive index of 2.7 at 357 nm

wavelength.^[28] These emissions come out of the ends of the NWs through the available open space while other ends are at the excitation with laser light. In this regard we have also calculated the condition for a NW to function as a single-mode optical waveguide,^[29] where $1 \approx \pi d \sqrt{n_1^2 - n_2^2} / \lambda < 2.4$, with 1 being the practical lower limit. For diameter, d of our NWs $\sim 40(\pm 5)$ nm (sample R3) and $55(\pm 5)$ nm (sample R4) at wavelength, $\lambda = 357$ nm; $n_1 \sim 2.7$ and $n_2 = 1$ are the refractive indices of the NW around 357 nm and surrounding medium of air, respectively, we can get the minimum value close to 1.

3.6 Summary

Size selective nonpolar wurtzite GaN NWs with uniform surface morphology are grown by reducing the O concentration to the background level. The NWs, grown under O rich conditions, show inhomogeneous surface morphologies and non-uniform size distribution. Electron energy loss spectroscopic measurements confirm large variations in the O concentrations along the NW grown under O rich conditions. High resolution transmission electron microscopic analysis reveals that the nonpolar NWs are grown along $[11\bar{2}0]$ with side facets $(10\bar{1}0)$. Far field bright multiple violet emission spots from NWs, grown under the O reduced condition, show formation of single-mode waveguide in these samples. Thus by controlling the O concentration, large scale growth of high structural and optical quality nonpolar GaN NWs is reported by using simple yet versatile chemical vapor deposition technique. The results pave the way for commercialization of ensemble GaN NW devices for optoelectronic applications.

3.7 References

- [1] G.A. Slack, L.J. Schowalter, D. Morelli, J.A. Freitas Jr, *J. Cryst. Growth* **2002**, 246, 287.
- [2] T. Mattila, R. Nieminen, *Phys. Rev. B* **1996**, 54, 16676.
- [3] S. Pearton, H. Cho, J. LaRoche, F. Ren, R. Wilson, J. Lee, *Appl. Phys. Lett.* **1999**, 75, 2939.
- [4] J.L. Lyons, A. Janotti, C.G. Van de Walle, *Appl. Phys. Lett.* **2010**, 97, 152108.
- [5] A. Patsha, P. Sahoo, S. Dhara, and A. K. Tyagi, *AIP Conf. Proc.* **2012**, 1447, 1289.
- [6] P. Sahoo, D.S. Oliveira, M.n.A. Cotta, S. Dhara, S. Dash, A.K. Tyagi, B. Raj, *J. Phys. Chem. C* **2011**, 115, 5863.
- [7] A. Patsha, P. Sahoo, Kishore K. Madapu, S. Dhara, and A. K. Tyagi, *IEEE Xplore, Proc. of the International Conf. on Nanoscience, Engineering and Technology*, **2011**, 553.
- [8] C.-K. Kuo, C.-W. Hsu, C.-T. Wu, Z.-H. Lan, C.-Y. Mou, C.-C. Chen, Y.-J. Yang, L.-C. Chen, K.-H. Chen, *Nanotechnology* **2006**, 17, S332.
- [9] P. Sahoo, S. Dhara, S. Dash, A.K. Tyagi, *Nanosci Nanotechnol-Asia* **2011**, 1, 140.
- [10] C.V. Thompson, *Annu. Rev. Mater. Res.* **2012**, 42, 399.
- [11] T. Kuykendall, P.J. Pauzauskie, Y. Zhang, J. Goldberger, D. Sirbuly, J. Denlinger, P. Yang, *Nat. Mater.* **2004**, 3, 524.
- [12] S.Y. Bae, H.W. Seo, J. Park, H. Yang, H. Kim, S. Kim, *Appl. Phys. Lett.* **2003**, 82, 4564.
- [13] G.T. Wang, A.A. Talin, D.J. Werder, J.R. Creighton, E. Lai, R.J. Anderson, I. Arslan, *Nanotechnology* **2006**, 17, 5773.
- [14] S. Kataria, A. Patsha, S. Dhara, A.K. Tyagi, H.C. Barshilia, *J. Raman Spectrosc.* **2012**, 43, 1864.

- [15] A. Patsha, S. Amirthapandian, R. Pandian, S. Dhara, *J. Mater. Chem. C* **2013**, 1, 8086.
- [16] J.E. Northrup, J. Neugebauer, *Phys. Rev. B* **1996**, 53, R10477.
- [17] J. Elsner, R. Jones, M. Haugk, R. Gutierrez, T. Frauenheim, M. Heggie, S. Oberg, P. Briddon, *Appl. Phys. Lett.* **1998**, 73, 3530.
- [18] J.E. Northrup, *Phys. Rev. B* **2006**, 73, 115304.
- [19] R.F. Egerton, *Rep. Prog. Phys.* **2009**, 72, 016502.
- [20] R.F. Egerton, *Electron energy-loss spectroscopy in the electron microscope*, Springer Science+ Business Media, **2011**.
- [21] T. Azuhata, T. Sota, K. Suzuki, S. Nakamura, *J. Phys.: Condens. Matter* **1995**, 7, L129.
- [22] H. Harima, *J. Phys.: Condens. Matter* **2002**, 14, R967.
- [23] A. Patsha, P. Sahoo, S. Dhara, S. Amirthapandian, A.K. Tyagi, *J. Raman Spectrosc.* **2013**, 44, 651.
- [24] M.A. Reshchikov, H. Morkoç, *J. Appl. Phys.* **2005**, 97, 061301.
- [25] P. Sahoo, J. Basu, S. Dhara, H.C. Fang, C.-P. Liu, T.R. Ravindran, S. Dash, A.K. Tyagi, *J. Mater. Sci.* **2012**, 47, 3447.
- [26] M. Toth, K. Fleischer, M. Phillips, *Phys. Rev. B* **1999**, 59, 1575.
- [27] P. Sahoo, D.S. Oliveira, M.n.A. Cotta, S. Dhara, S. Dash, A.K. Tyagi, B. Raj, *J. Phys. Chem. C* **2011**, 115, 5863.
- [28] A. Barker, M. Ilegems, *Phys. Rev. B* **1973**, 7, 743.
- [29] C.-L. Chen, *Elements of optoelectronics and fiber optics*, Irwin Chicago, **1996**.

CHAPTER 4

EFFECT OF Mg DOPING ON NONPOLAR GaN NANOWIRES

4.1 Introduction

The functionality of nanoscale electronic and optoelectronic devices made of compound semiconductor NWs like group III–nitrides relies on the complex process of doping. The efforts put on the incorporation of dopants in the III–nitride based GaN NWs lead to nanodevices of LED, lasers, HEMT, logic gates, photodetectors, solar cells and gas sensors.^[1-7] Apart from the doping process the type of dopant and defects, variation in NW size and crystallographic orientations heavily influence the growth and various electrical and optical properties of NWs.^[8-12] Generally the NWs are grown via catalyst mediated VLS method which offer control over diameter and composition of the NWs.^[9,13] For the growth of compound semiconductors like III–nitride NWs in the VLS process, the liquid/solid interface involving the catalyst and the NW plays a crucial role in driving axial growth of the NW. Abrupt variations in composition at the interface deviates the NW growth from steady state.

Mg is the most successful *p*-dopant in III–nitrides,^[14-16] which paves the way for realizing III–nitride based electronic^[15,16] and optoelectronic devices.^[3,4,17] Doping of III–nitride NWs, in particular *p*-type doping, is a difficult process compared to that for thin films as the dopant incorporation and distribution depends on N/III ratio and incorporation pathways, respectively.^[18,19] Depending on the dopant type, host lattice, and crystallographic orientation, the incorporation pathways can alter in NWs as well as in thin films.^[20-22] Understanding of the dopant incorporation paths in NWs can help in tuning the dopant distribution over a precise location along the NW which is crucial for aforementioned NW devices.

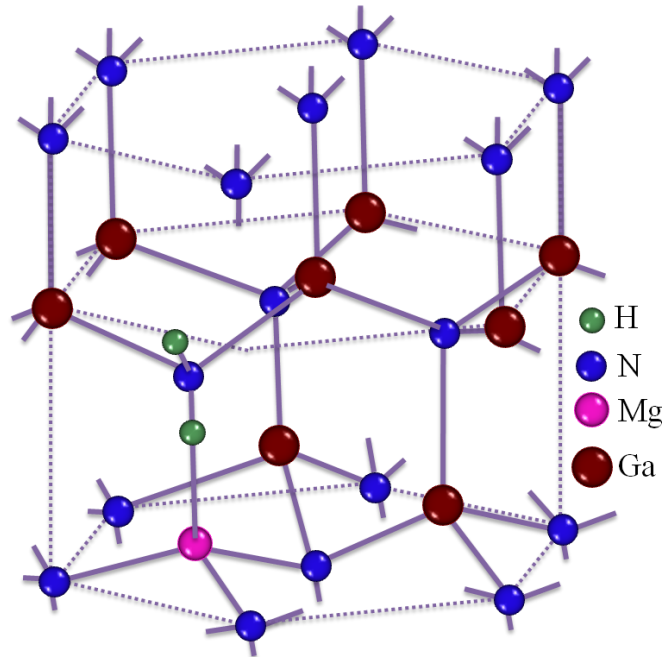


Fig. 4.1 Schematic representation of the proposed bond center and anti-bonding site incorporation of H in GaN and its passivation of Mg during growth of GaN.^[23]

Mg incorporates in GaN by substituting in place of Ga atom as shown in the schematic (Fig. 4.1). Because of its high-acceptor ionization energy in GaN, however, concentration of un-ionized Mg dopants is high at room temperature leading to low hole density. Also the native point defects like V_N and unintentional impurity (O) atoms act as donors which suppress the hole density further.^[24] Thus, all these factors make high Mg doping necessary in order to overcome the excess electron density due to unintentional donors as well as low hole concentration due to high acceptor ionization energy. At the same time, high doping levels of Mg in GaN is found to create pyramidal defects and stacking faults as well as reduction in hole density because of self-compensation and compensation due to the formation of excess amount of V_N .^[25-27] So, the optimization of Mg doping levels in GaN is also a necessary as well as a challenging process for increasing the hole concentration. Depending on the growth method, there are possibilities of multiple acceptor levels due to Mg dopant and complexes formed by it.^[28,29] Photoluminescence studies on Mg

doped GaN give a better understanding of these acceptors formed by Mg dopants. In this chapter, studies carried out on Mg dopant incorporation in GaN NWs grown in the CVD technique via VLS process, are reported. Effect of Mg dopants at the liquid/solid interface (Au–Ga/GaN) is studied in the axial growth of GaN NWs to find the pathway of the Mg incorporation. Influence of Mg doping on morphology, structure and optical properties of GaN NWs are also reported.

4.2 Growth of Mg Doped GaN Nanowires in VLS Process Using APCVD

Mg doped nonpolar GaN NWs were synthesized in the APCVD technique using the VLS process. The Au nanoparticles of size $\sim 55(\pm 10)$ nm on Si (111) substrate were used for the NWs growth.^[11] Ga metal (99.999%, Alfa Aesar) as precursor, NH₃ (99.999%) as reactant gas and mixture of UHP Ar+H₂ (5N) as carrier gases were used for the growth. Mg₃N₂ (Alfa Aesar) was used as a source for incorporating Mg in the GaN NWs. Si substrate with Au nanoparticles was kept upstream to the Ga droplet and Mg source in a high pure alumina boat which was placed into a quartz tube. The temperature of the quartz tube was slowly raised to a growth temperature of 900 °C with 15 °C min⁻¹ ramp rate. NWs were grown for 1 h by purging 10 sccm of NH₃ reactant gas, and 20 sccm of Ar carrier gas and the growth process was intentionally terminated by reducing the temperature of the growth zone. Concentration of the Mg dopant was controlled by changing either the distance between the Mg source and substrate or the flow rate of the carrier gas. Mg dopants, for *p*-type conduction in GaN NWs, were activated by thermally annealing the as-grown samples in a separate quartz tube in the N₂ atmosphere at 750 °C for 30 min.

4.3 Study on Dopant Pathway in VLS Grown Mg Doped GaN Nanowires

4.3.1 Morphological Study:

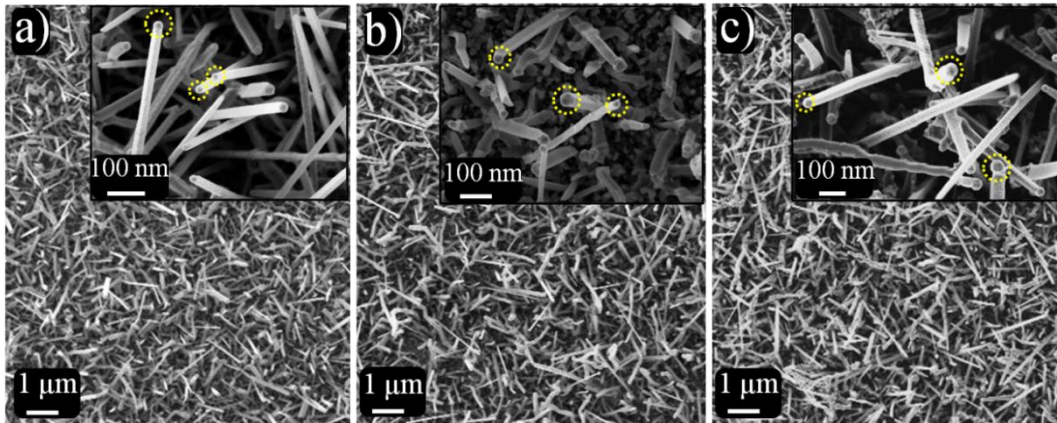


Fig. 4.2 Typical FESEM images of GaN NWs. (a) Undoped NWs having uniform diameter along with the Au catalyst particle (encircled) at the tip of the wire (inset). (b) GaN:Mg-I and (c) GaN:Mg-II are Mg doped GaN NWs. The sample GaN:Mg-I is less doped compared to that of the sample GaN:Mg-II. All the NWs are grown with Au catalyst particle (encircled) at the tip (insets b, c).

Morphological variations in the Mg doped GaN NWs grown with two different concentrations of Mg are compared with that of the undoped NWs using FESEM (SUPRA 55 Zeiss) studies. Fig. 4.2 shows the typical FESEM micrographs of the three samples of GaN NWs in which one is undoped (Fig. 4.2a) and two are Mg doped, GaN:Mg-I (Fig. 4.2b) and GaN:Mg-II (Fig. 4.2c). The GaN:Mg-I NWs are less doped compared to that of the GaN:Mg-II. The particle at the tip shows that the NWs are grown in VLS process (insets in Figs. 4.2a-c). The diameter of the NWs exactly follows the size of the catalyst particle at the tip and has uniform shape and size distribution of $\sim 60 (\pm 5)$ nm for the undoped sample (inset in Fig. 4.2a). The growth rate of the NWs is found to be $3 \mu\text{m}\cdot\text{h}^{-1}$. Noticeable change in the morphology and increase in the diameter distribution (65 ± 5 nm) are observed for the samples of GaN:Mg-I compared to those of undoped NWs. Whereas a distinct tapering at the

tip region and increase in the diameter distribution to 70 (± 10) nm have been observed for the GaN:Mg-II NWs while increasing the doping concentration. The increase in the diameter of the doped NWs may be due to the increased contact angle of the catalyst in the presence of impurity.^[9]

4.3.2 Compositional and Structural Study:

The XPS studies were carried out on Mg doped GaN NWs using an X-ray source of nonmonochromatic Al K α (1486.6 eV), and the binding energy values were measured by referencing with respect to the C 1s peak. The spectra were processed by applying Shirley type background and curve fitted with mixture of Gaussian–Lorentzian line shape. Typical XPS spectra are shown (Fig. 4.3) for undoped and Mg doped GaN:Mg-I and GaN:Mg-II NWs.

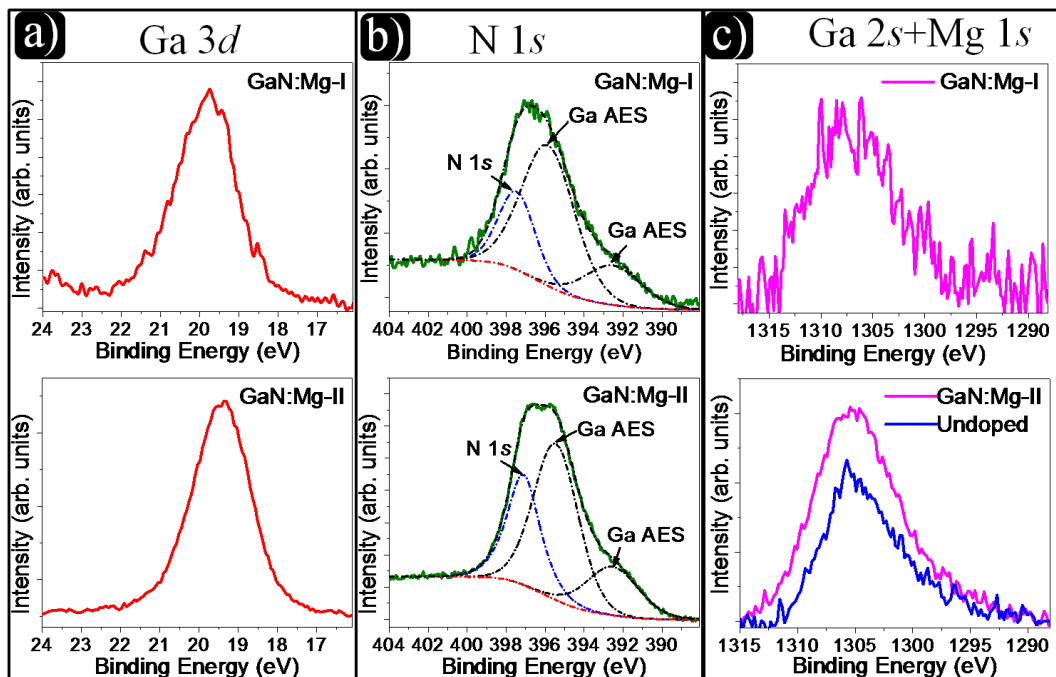


Fig. 4.3 XPS spectra from Mg doped GaN NWs of the samples GaN:Mg-I and GaN:Mg-II: (a) Ga 3d (b) N 1s and (c) Ga 2s + Mg 1s. Ga 2s peak recorded from undoped sample is plotted in (c) for comparison. Solid lines are experimental data, and discontinuous lines are fitted data.

Binding energy of Ga 3*d* level (Fig. 4.3a) for the GaN:Mg-I NWs is observed at 19.8 eV, while it is observed at 19.4 eV for the sample GaN:Mg-II.^[30] The binding energy of N 1*s* core level (Fig. 4.3b) is identified by deconvoluting the corresponding spectra from the Ga Auger electron spectra (Ga AES). N 1*s* core level is identified at 397.5 eV (Fig. 4.3b) for the GaN:Mg-I NWs while it is observed at 397.1 eV for the GaN:Mg-II.^[30] Binding energies of both Ga 3*d* and N 1*s* levels are red shifted by 0.4 eV while increasing the Mg concentration. For Mg 1*s* core level, spectra were recorded in the binding energy range 1320–1290 eV. A broad peak, observed in the energy range 1312–1300 eV for GaN:Mg-I sample, is difficult to be deconvoluted for the Mg 1*s* and Ga 2*s* peaks (Fig. 4.3c). It is because both peaks are in the same region and FWHM of the peak is quite high (~10 eV).^[31] However, in the case of the sample GaN:Mg-II, the intensity of the broad peak is increased significantly (Fig. 4.3c). When the spectra were compared with the pure Ga 2*s* peak of the undoped sample (Fig. 4.3c), both the shape and FWHM of the peaks were significantly different from each other. This shows the presence of Mg in doped NWs. Since the Ga 2*s* peak is quite asymmetric in shape, it is not possible to subtract it from the doped sample in order to estimate the Mg concentration.^[31]

For structural studies, HRTEM (LIBRA 200FE Zeiss) observations were performed on NWs which were dispersed in isopropyl alcohol and transferred to the TEM Cu grids. A typical low magnification TEM micrograph of an undoped NW shows a perfect rod-like shape with uniform surface morphology (Fig. 4.4a). It also shows an Au catalyst particle at the tip. The SAED pattern (right outset of Fig. 4.4a) reveals that the NW is a single crystalline wurtzite phase of GaN with zone axes along [0001]. A sharp interface between GaN NW and Au catalyst particle is seen in the HRTEM image (bottom outset of Fig. 4.4a). An interplanar spacing of 0.275 nm (zoomed view in the inset of bottom outset of Fig. 4.4a) corresponds to the nonpolar {10 $\bar{1}$ 0} planes of wurtzite GaN.^[11] The growth direction of the

NW is found to be along the $[10\bar{1}0]$ direction. A typical low magnification TEM micrograph of a doped NW shows a rod-like shape with uniform surface morphology (Fig. 4.4b). The SAED pattern (outset of Fig. 4.4b) of the GaN:Mg-I NW, collected along the zone axis $[01\bar{1}0]$, is also found to be single crystalline wurtzite phase. From the magnified view (inset of bottom outset of Fig. 4.4b) of the NW near the tip region, a distinct contrast is observed along with a small distorted portion (~ 20 nm in length) of the wire right below the catalyst particle. The sharp interface between the NW and Au catalyst particle is also lost. A lattice resolved high resolution image (bottom outset of Fig. 4.4b) shows an interface formed between NW and distorted portion of the wire where the gradual orientation of the lattice fringes of $\{10\bar{1}0\}$ planes is observed.

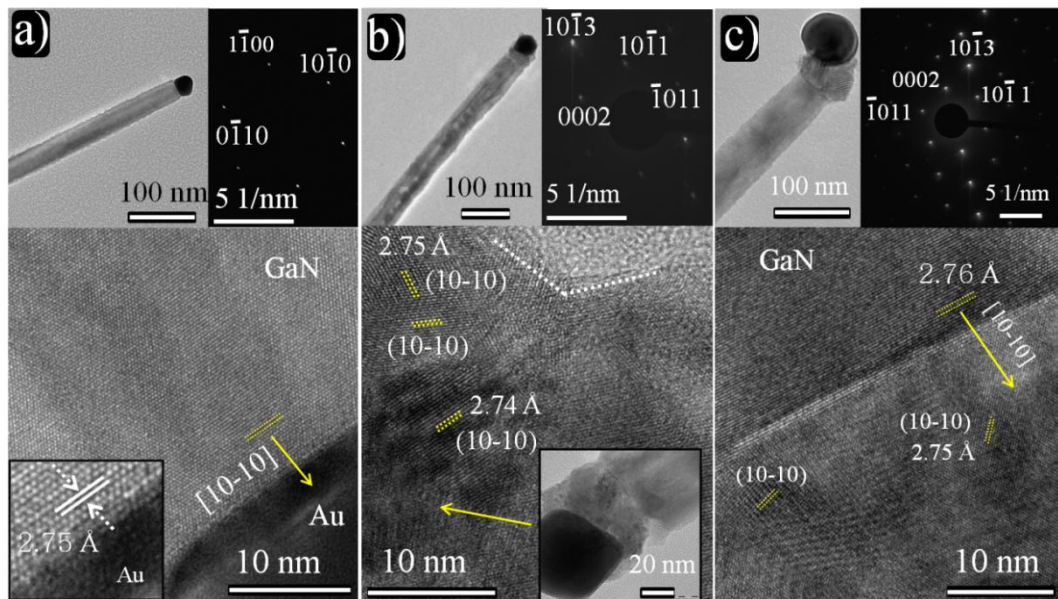


Fig. 4.4 (a) Low magnification TEM image of a typical undoped GaN NW. SAED of the NW, indexed to wurtzite GaN with zone axis along $[0001]$. HRTEM collected near the tip of the NW having growth direction along $[10\bar{1}0]$ and a sharp interface between Au and GaN is seen (inset). (b) GaN NW doped with Mg (GaN:Mg-I). SAED pattern of the NW collected along the zone axis $[01\bar{1}0]$ of wurtzite phase. An interface separating the NW and distorted portion of the tip region with Au nanoparticle is seen in HRTEM. Inset shows the contrast variation in the tip region. (c) GaN NW doped with increased Mg concentration (GaN:Mg-II). SAED pattern of the NW collected along the zone axis $[01\bar{1}0]$ of wurtzite phase. Clear interface is visible in the HRTEM collected near the tip region and NW having growth direction along $[10\bar{1}0]$. Inset shows lattice fringes of $(10\bar{1}0)$ planes at the interface.

Variation in contrast along the wire between the catalyst particle and the interface (inset of bottom outset of Fig. 4.4b) may be due to different grain thickness formed by the excess incorporation of the Mg. Sample GaN:Mg-II, with greater doping concentration than that of GaN:Mg-I, is also found to have similar distorted growth in a small portion of the wire (~40 nm length) near the tip region right below the catalyst particle (Fig. 4.4c). An increase in diameter of this small portion is also observed, as compared to that of the remaining portion of the NW. SAED pattern on the NW collected along the zone axis $[01\bar{1}0]$ shows single crystalline wurtzite phase of GaN (outset of Fig.4.4c). An interplanar spacing of 0.276 nm (bottom outset of Fig. 4.4c) corresponds to the nonpolar $\{10\bar{1}0\}$ planes of wurtzite GaN. The growth direction is found to be along the $[10\bar{1}0]$.

4.3.3 Dopant pathway study:

The observations from structural studies suggest that, during the VLS growth process of GaN NW in the CVD technique, the Mg dopants may have also incorporated at liquid/solid interface of Au–Ga/GaN along with the N atoms. Incorporation of the N is expected directly at the interface, as being a group V element it cannot be dissolved in the Au catalyst.^[18] On the other hand, Mg can easily be dissolved in the Au and can be infused through Au–Ga/GaN interface.^[18] When the growth process is terminated by reducing the growth temperature, the excess incorporation of the Mg dopants at the tip region below the catalyst particle may have introduced stacking faults along the NW leading to the twinning of the $\{10\bar{1}0\}$ planes.^[26] However, a clear interface is observed for GaN:Mg-II NWs at the junction of the NW and the distorted portion similar to that of GaN:Mg-I NWs as the growth continues (Figs. 4.4b,c).

The EELS studies were carried out for identifying the presence of Ga, N, and Mg in a single NW using in-column second order corrected omega energy filter type spectrometer with an energy resolution of 0.7 eV. No appreciable changes in the shape of N *K*-edge spectra

(Fig. 4.5a) of Mg doped NWs (GaN:Mg-I and GaN:Mg-II) are observed with respect to that of the undoped NWs. Typical low intensity Mg *K*-edge spectra (Figs. 4.5b,c) collected from single GaN:Mg-I and GaN:Mg-II NWs are presented. As the extended feature of the Ga *L*-edge is overlapping with the Mg *K*-edge, we compare the same region with that of the undoped NWs (Figs. 4.5d,e).

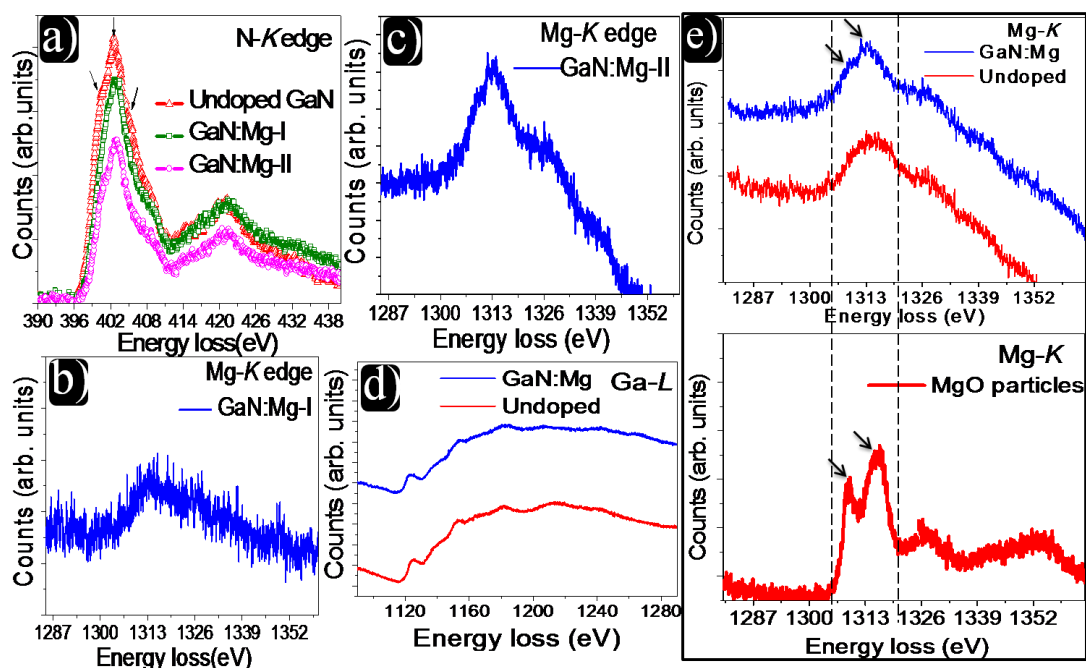


Fig. 4.5 Typical EELS spectra corresponding to (a) N *K*-edge collected from the NWs of three samples, and Mg *K*-edges collected from single GaN NWs of Mg doped samples (b) GaN:Mg-I and (c) GaN:Mg-II. Comparison of EELS spectra corresponding to (d) Ga-*L* edge and (e) Mg-*K* edges collected from single GaN NWs of the undoped and Mg doped sample (top). Mg-*K* edge is also compared with that of MgO reference sample (bottom) showing similar fine feature as observed in the Mg doped GaN NWs.

A significant variation in the ELNES, similar to the Mg *K*-edge features of reference MgO sample (Fig. 4.5e) is observed for doped NWs, confirming the presence of Mg atoms in our doped samples.

Distribution of Mg dopants along each NW of both the Mg doped samples is investigated using EFTEM micrographs generated from the electron energy loss due to Ga, N and Mg atoms. Figs. 4.6a,b (grey color) depicts the typical zero-loss EFTEM micrographs of

GaN:Mg-I and GaN:Mg-II NWs, respectively. The EFTEM micrographs corresponding to the Ga *L*-edge for the two samples (red color in Figs. 4.6a,b) reveal uniform distribution of the Ga along the wire including the Au catalyst particle. This observation reveals that incorporation of the Ga has occurred through the Au catalyst and formed the Au–Ga alloy.

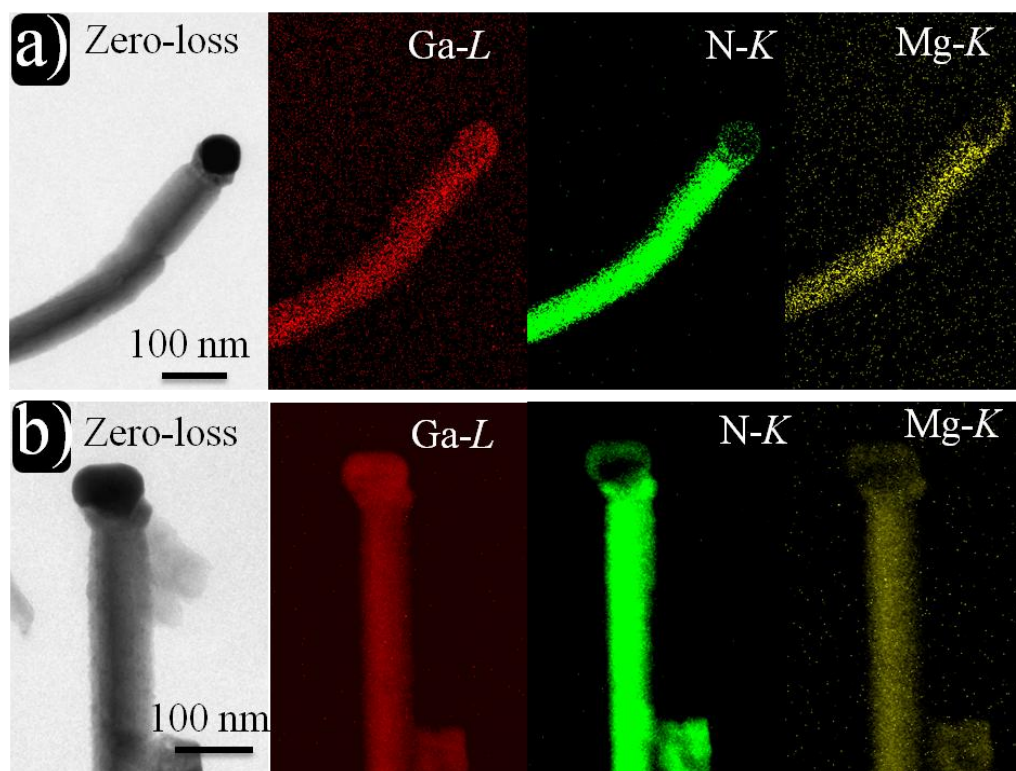


Fig. 4.6 EFTEM micrographs generated from the NW for each Mg doped sample (a) GaN:Mg-I and (b) GaN:Mg-II correspond to zero-loss energy (grey color), Ga-*L* (red color), N-*K* (green color) and Mg-*K* (yellow color). These are pseudocolors chosen for describing presence of different elemental species in the NW.

Similar observations were made in case of undoped GaN NWs (Fig. 4.7a). However, the EFTEM micrographs for the N *K*-edge, of both Mg doped as well as undoped NWs (green color in Figs. 4.6a,b and Fig. 4.7a) show uniform distribution of the N atoms along the wire except in the Au particle. The observation confirms that the N has been incorporated through the interface between Au–Ga/GaN. A faint contrast around the catalyst particle in case of the sample GaN:Mg-II (green color in Fig. 4.6b) is due to the small distorted portion of GaN NW surrounded below the particle, which is projected out of the plane.

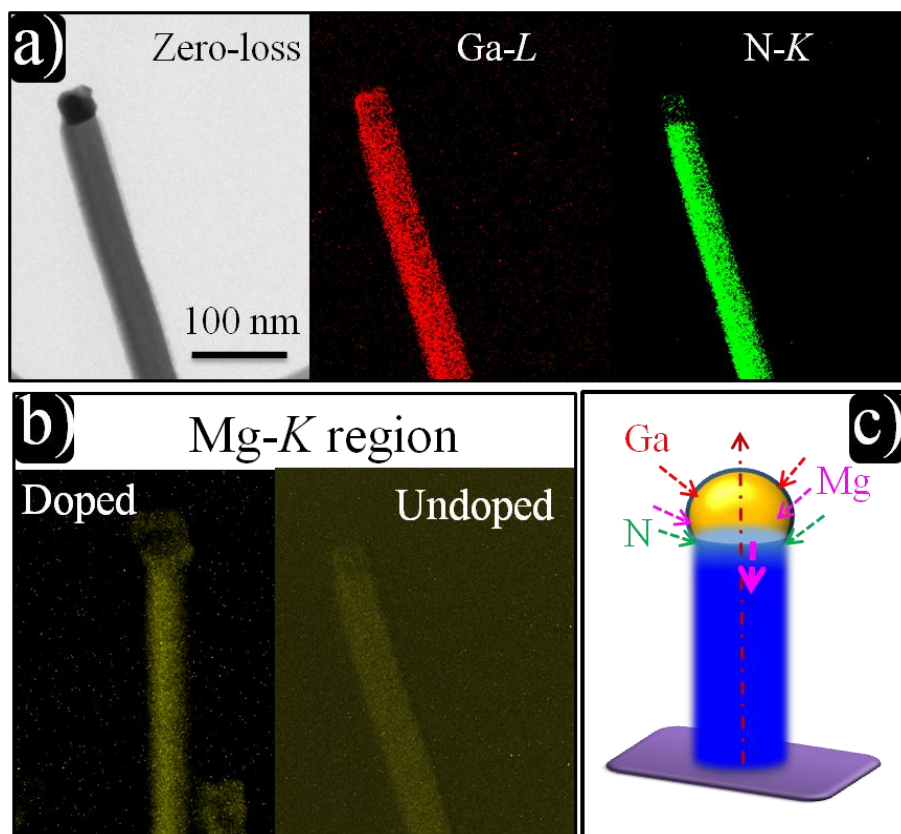


Fig. 4.7 (a) EFTEM micrographs collected from the undoped NW (b) Comparison of the EFTEM micrographs generated from the Mg *K*-edge region, collected from doped and undoped NWs. Au catalyst particle appears dark in the doped NW in the absence of Mg at the tip. Whereas in case of undoped sample, uniform contrast is observed including the catalyst particle due to the extended features of Ga *L*-edge. (c) Schematic view of the incorporation pathways of different elements during the VLS growth of NW.

The EFTEM micrographs corresponding to the Mg *K*-edge (yellow color in Figs. 4.6a,b) depict that the Mg is uniformly distributed along the NW up to the catalyst particle while it is absent in the catalyst particle. Since the Mg *K*-edge and extended feature of Ga *L*-edge overlap with each other, we have selected a narrow energy window at Mg-*K* edge region to generate the EFTEM micrographs with minimum effect of Ga *L*-edge and have compared with that of the undoped NW (Fig. 4.7b). Catalyst Au nanoparticle appears dark due to the absence of Mg in the doped sample. However, in the case of the undoped NW, a very faint uniform contrast is observed for the NW including the catalyst nanoparticles due to the extended features of Ga *L*-edge. This is happened because the Ga formed an alloy with Au

and diffused toward the NW. So, the Au particle does not disappear in the EFTEM micrograph of the undoped NW. The uniform contrast of the Mg element along the NW with uniform shape revealed that the Mg dopants, preferably, were incorporated through the Au–Ga/GaN interface during the axial growth process (Fig. 4.7c). It is different for NWs synthesized in the radial growth process using epitaxial techniques where the Mg incorporation takes place along the side facets showing accumulation of dopants along the side walls forming a shell.^[18] The uniform distribution of the dopant in a single NW indicates insignificant surface accumulation of Mg in the present study using the CVD growth technique. It is also clear from the micrographs that the amount of the Mg dopants is less in GaN:Mg-I (yellow color in Fig. 4.6a) than that of the GaN:Mg-II (yellow color in Fig. 4.6b) NWs. The observation is consistent with that of the doping levels used during growth of the samples.

4.4 Optical Properties

4.4.1 Raman Spectroscopic Study:

The Raman spectroscopy studies were carried out on a single (dispersed on crystalline Cu(100) substrate) and the ensemble Mg doped GaN NWs of the sample GaN:Mg-II. A typical spectrum of ensemble NWs shows (Fig. 4.8a) the peaks at 252, 421, 570, and 728 cm^{-1} . The wave numbers 570, and 728 cm^{-1} correspond to the symmetry allowed E_2^H and $A_1(\text{LO})$ the phonon modes, respectively, of the wurtzite GaN.^[32] Additional peaks at 252 and 421 cm^{-1} are ZB phonon modes of GaN which are non-zone centre phonons appearing due to the finite crystallite size effects. The peaks around 521 and $\sim 305 \text{ cm}^{-1}$ in ensemble NWs (Fig. 4.8a) correspond to the optical and ZB_{Si} modes, respectively, of Si substrate on which NWs were grown. A small hump in the range of 600-650 cm^{-1} may contain both the surface optical (SO) and the LVM modes of Mg doped GaN. Identification of these modes with a

such a low intensity, however is difficult because of non-uniformity of doping in the ensemble NWs using normal Raman spectroscopy. The localized study of the vibrational modes in single NWs using the evanescent field of Au nanoparticle attached SPM tip assisted TERS is elucidated further. The shift in E_2^H and $A_1(\text{LO})$ mode by 2 and 3 cm^{-1} , respectively, as compared to that of the undoped NWs (Fig. 3.19b; Chapter 3), may be due to the stress generated by high Mg doping in GaN in the doped GaN:Mg-II sample.^[32]

The intensity, position and FWHM of the $A_1(\text{LO})$ phonon peak are strongly influenced by the free carrier concentration (electrons/holes) in the GaN as a result of the LO phonon-plasmon coupling.^[32,33] As the free carrier concentration increases, the intensity of the $A_1(\text{LO})$ phonon peak diminishes and the peak position shifts to higher wave number with asymmetric shape and broadening. The spectrum corresponding to the ensemble of sample GaN:Mg-II showed a sharp intense peak of $A_1(\text{LO})$ mode which could be due to a very weak phonon-plasmon coupling. This suggests the high resistive nature of the Mg doped GaN NWs (Fig. 4.8a). The high resistive nature of highly doped GaN:Mg is expected owing to the self-compensation of Mg dopant and its passivation by H. However, in case of a single NW, the asymmetric broadening and the reduction in the intensity of $A_1(\text{LO})$ mode show the phonon-plasmon coupling appears to be strong as compared that of the ensemble NWs. The difference in the characteristic features of phonon-plasmon coupling observed among single and ensemble NWs, suggests the non-uniform doping in ensemble GaN NWs. In order to observe the local chemical changes by monitoring the lattice vibration modes of single NWs, TERS spectrum on a single NW of the sample GaN:Mg-II was also recorded and compared with that of undoped GaN NW. The AFM image of single NWs of undoped and doped (GaN:Mg-II) samples are presented in Fig. 4.8b. Additional peaks are observed at 537, 633 and 656 cm^{-1} along with ZB (421 cm^{-1}), and symmetry allowed E_2^H (570 cm^{-1}) and $A_1(\text{LO})$ (729 cm^{-1}) modes of GaN for the sample GaN:Mg-II (Fig. 4.8c). The peak at 537 cm^{-1}

corresponds to the $A_1(\text{TO})$ phonon mode,^[32] and the peak at 633 cm^{-1} corresponds to SO mode of GaN.^[34] The additional peak at 656 cm^{-1} corresponds to the LVM mode due to Mg doping in GaN.^[32] Both $A_1(\text{TO})$ and SO modes also appear for the undoped NW (Fig. 4.8d) but with reduced intensity and broadening.

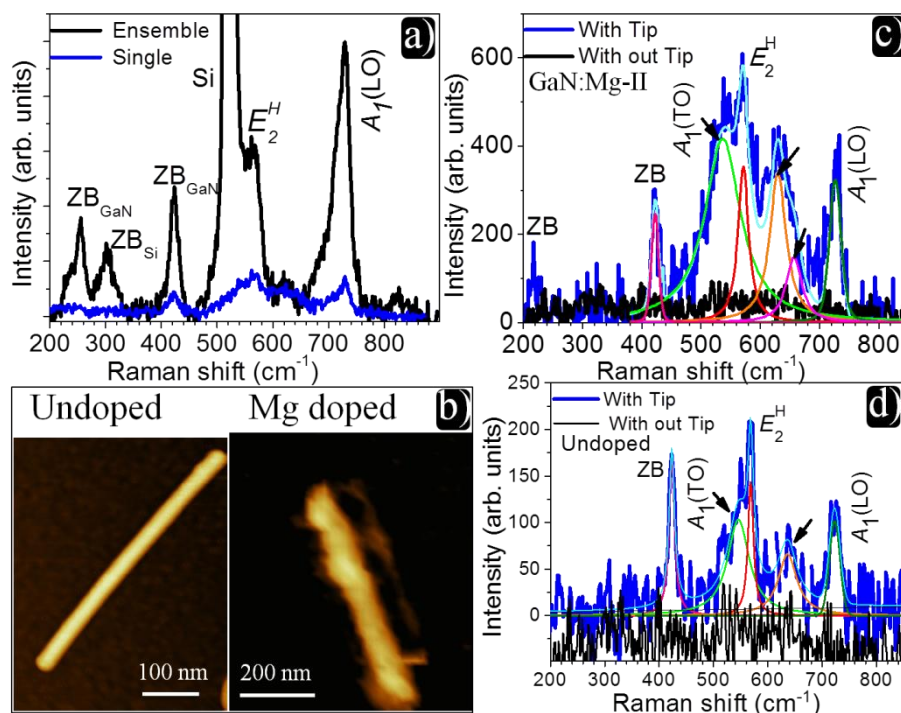


Fig. 4.8 (a) Typical Raman spectra of ensemble and single GaN NW of sample GaN:Mg-II (b) AFM images of single NW of undoped and doped (GaN:Mg-II) samples. TERS spectra of a single NW of (c) GaN:Mg-II and (d) undoped samples collected with and without TERS tip. Spectrum of undoped sample collected without tip is vertically shifted down to avoid the overlap.

4.4.2 Photoluminescence Study:

The PL studies were carried out on undoped and Mg doped GaN NWs with an excitation wavelength of 325 nm of the He–Cd laser. The spectra were collected using 2400 lines mm^{-1} grating and thermoelectrically cooled CCD detector. The luminescence from the undoped GaN NWs at room temperature (300 K) shows a broad band ranging from 3.3 to 3.5 eV (Fig. 4.9a). When the NWs were cooled to 80 K, the spectra were dominated by a peak at 3.516 eV followed by the peaks at 3.475 and 3.33 eV (Fig. 4.9a). The PL peak at 3.516 eV

corresponds to FE transition between conduction band minimum and valence band maximum along with its 2LO phonon replica (FE-2LO) at 3.33 eV.^[11] An intense luminescence of FE emission represents the high optical quality of the undoped NWs. The luminescence peak at 3.475 eV (Fig. 4.9a) is identified as the emission due to the DBE.^[24] Mg doped GaN:Mg-I and GaN:Mg-II NWs (Figs. 4.9b,c) show emission of a broad band around 3.2 to 3.3 eV, generally termed as the ultraviolet luminescence (UVL) along with low intensity BL peaks around 2.85 eV,^[35] and the acceptor bound excitons (ABE)^[36] at 3.46 eV at 300 K. The UVL and the BL peaks, which are assigned to the DAP transitions involving Mg acceptors, are the main signatures of Mg doped GaN samples.^[36]

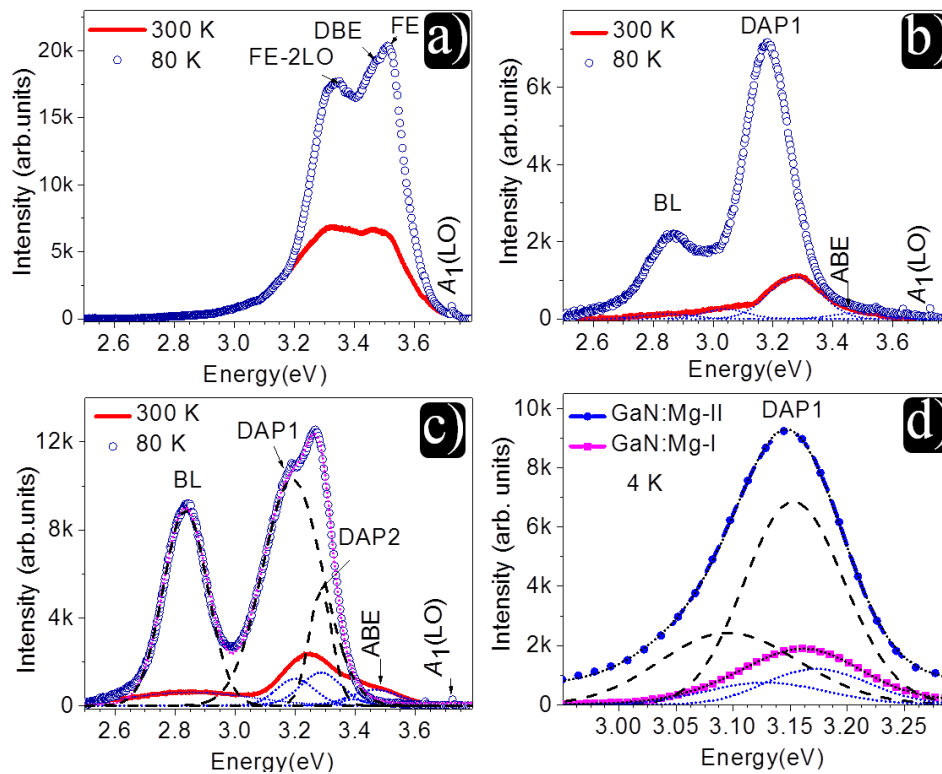


Fig. 4.9 Typical PL spectra of GaN NWs of the samples (a) undoped, (b and c) Mg doped in increased concentration, GaN:Mg-I and GaN:Mg-II respectively, collected at the temperatures 300 and 80 K. (d) DAP1 peak at 4 K for the NWs of Mg doped samples GaN:Mg-I and GaN:Mg-II. Discontinuous lines are fitted data corresponding to the individual peaks.

At low temperature (80 K), PL spectra of both the Mg doped samples (GaN:Mg-I and GaN:Mg-II) are dominated by DAP peaks (Figs. 4.9b-d). The BL peak appears because of the transitions between shallow acceptors (Mg_{Ga}) and deep donors, presumably owing to the V_N . The intensity of the BL band increases with increasing Mg doping in GaN. The significant increase in the intensity of the BL band around 2.85 eV (Figs. 4.9b,c) is clearly observed for our Mg doped GaN NWs. As the doping concentration in GaN:Mg-II NWs is higher than that for the GaN:Mg-I samples, the intensity of the BL band of the former is quite high compared to that of the latter. The UVL peaks due to the DAP transitions are another significant feature in the PL spectra of the Mg doped GaN NWs. An intense peak at 3.18 eV in the PL spectra (Fig. 4.9b) of sample GaN:Mg-I corresponds to DAP transition (DAP1) involving shallow acceptors and shallow donors (V_N). The shallow acceptor is attributed to the acceptor formed by Mg as a substituent for Ga (Mg_{Ga}).^[35] However, in the case of GaN:Mg-II NWs, luminescence due to DAP (DAP1) transitions is observed around 3.18 eV along with a shoulder peak around 3.28 eV which may be due to another type of DAP transition (DAP2).^[28] The observation of DAP2 transitions may arise because of two different types of acceptors having different binding energies related with Mg or due to two types of donor states related to V_N and their complexes with H.^[28,29] The DAP2 transition may be observed at higher temperature because of the defective nature of the band. In both the samples of Mg doped GaN NWs, the PL peak corresponding to the ABE is suppressed by DAP peaks at 80 K. A tiny peak around 3.72 eV in the PL spectra of all the three samples (Figs. 4.9a-c) corresponds to symmetry allowed Raman mode of $A_1(LO)$.^[11] At 4 K, only one kind of DAP transition (DAP1) in PL spectra (Fig. 4.9d) is observed for both samples GaN:Mg-I and GaN:Mg-II revealing the unstable nature of DAP2.^[28] The peak position of the DAP1 is red shifted by 20 meV for the sample GaN:Mg-II with increase in the Mg doping level as compared to that of the GaN:Mg-I NWs. During the growth process, H evolved from NH_3

and carrier gases passivated both the acceptors (Mg_{Ga}) and donors (V_N) by forming the complexes of $Mg_{Ga}-H$ and V_N-H , respectively (Fig. 4.1).^[5] The presence of these two complexes may manifest in the observation of DAP2 peak, which is observed to be generally absent in the low temperature PL studies of annealed samples. During the post growth annealing process both the complexes dissociate and activate the Mg_{Ga} .^[24]

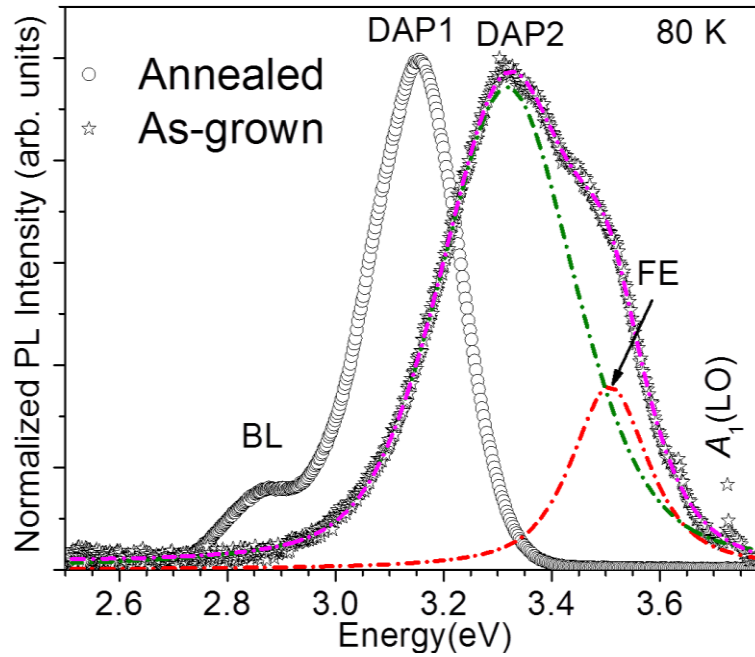


Fig. 4.10 Typical PL spectra of GaN NWs of the as-grown and annealed samples GaN:Mg-I, collected at the temperature 80 K.

The activation process of Mg dopants is further understood by studying the PL spectra of as-grown and annealed NWs. The luminescence of as-grown NWs shows (Fig. 4.10) a broad peak ranging from 3.0 to 3.6 eV. The PL peak at 3.51 eV (discontinuous curve in Fig. 4.10) corresponds to FE transitions. The broad peak at 3.31 eV (discontinuous curve in Fig. 4.10) corresponds to donor acceptor pair transition (DAP2) which is blue shifted by 20 meV due to excitation power of the laser. However, the PL spectra of annealed NWs show an intense peak at 3.15 eV corresponding to the DAP transition (DAP1) due to shallow donors (V_N) and shallow acceptors (Mg_{Ga}) in their pure form. Thus, the absence of DAP2 in the low

temperature PL studies of annealed samples show the successful incorporation and activation of different concentrations of Mg dopants in the nonpolar GaN NWs.

4.5 Summary

Mg doped *p*-type nonpolar GaN NWs are successfully grown via VLS mechanism by the CVD technique. HRTEM studies show that the NWs are grown along $[10\bar{1}0]$ nonpolar planes of GaN. XPS and EELS studies along with localized measurement using TERS on Mg doped NWs show the presence of Mg dopants. Local distortion and twinning of atomic planes between catalyst particle and the NW confirm the interface as Mg incorporation pathway. Structural analysis shows the direct evidence of incorporation of the Mg atoms through the Au–Ga/GaN interface for the first time using the energy filtered TEM imaging. Photoluminescence studies with DAP transition indicate successful activation of Mg dopants.

4.6 References

- [1] J.C. Johnson, H.J. Choi, K.P. Knutsen, R.D. Schaller, P. Yang, R.J. Saykally, *Nat. Mater.* **2002**, 1, 106.
- [2] R. Yan, D. Gargas, P. Yang, *Nat. Photonics* **2009**, 3, 569.
- [3] Y.B. Tang, Z.H. Chen, H.S. Song, C.S. Lee, H.T. Cong, H.M. Cheng, W.J. Zhang, I. Bello, S.T. Lee, *Nano Lett.* **2008**, 8, 4191.
- [4] Y. Dong, B. Tian, T.J. Kempa, C.M. Lieber, *Nano Lett.* **2009**, 9, 2183.
- [5] F. Gonzalez-Posada, R. Songmuang, M. Den Hertog, E. Monroy, *Nano Lett.* **2012**, 12, 172.
- [6] M.D. Brubaker, P.T. Blanchard, J.B. Schlager, A.W. Sanders, A. Roshko, S.M. Duff, J.M. Gray, V.M. Bright, N.A. Sanford, K.A. Bertness, *Nano Lett.* **2013**, 13, 374.
- [7] P. Sahoo, S. Dhara, S. Dash, S. Amirthapandian, A.K. Prasad, A. Tyagi, *Int. J. Hydrogen Energy* **2013**, 38, 3513.
- [8] H.-Y. Chen, R.-S. Chen, N.K. Rajan, F.-C. Chang, L.-C. Chen, K.-H. Chen, Y.-J. Yang, M.A. Reed, *Phys. Rev. B* **2011**, 84, 205443.
- [9] S.K. Lim, S. Crawford, G. Haberfehlner, S. Gradecak, *Nano Lett.* **2013**, 13, 331.
- [10] D. Tham, C.Y. Nam, J.E. Fischer, *Adv. Funct. Mater.* **2006**, 16, 1197.
- [11] A. Patsha, S. Amirthapandian, R. Pandian, S. Dhara, *J. Mater. Chem. C* **2013**, 1, 8086.
- [12] R. Calarco, M. Marso, T. Richter, A.I. Aykanat, R. Meijers, V.D.H. A, T. Stoica, H. Luth, *Nano Lett.* **2005**, 5, 981.
- [13] X. Duan, C.M. Lieber, *Adv. Mater.* **2000**, 12, 298.
- [14] S.N. Das, S. Patra, J.P. Kar, M.-J. Lee, S.H. Hwang, T.I. Lee, J.-M. Myoung, *Mater. Lett.* **2013**, 106, 352.
- [15] Y. Huang, X. Duan, Y. Cui, C.M. Lieber, *Nano Lett.* **2002**, 2, 101.

- [16] G. Cheng, A. Kolmakov, Y. Zhang, M. Moskovits, R. Munden, M.A. Reed, G. Wang, D. Moses, J. Zhang, *Appl. Phys. Lett.* **2003**, 83, 1578.
- [17] M.L. Reed, E.D. Readinger, H. Shen, M. Wraback, A. Syrkin, A. Usikov, O.V. Kovalenkov, V.A. Dmitriev, *Appl. Phys. Lett.* **2008**, 93, 133505.
- [18] J. Wallentin, M.T. Borgström, *J. Mater. Res.* **2011**, 26, 2142.
- [19] D.E. Perea, E.R. Hemesath, E.J. Schwalbach, J.L. Lensch-Falk, P.W. Voorhees, L.J. Lauhon, *Nat. Nanotechnol.* **2009**, 4, 315.
- [20] S.C. Cruz, S. Keller, T.E. Mates, U.K. Mishra, S.P. DenBaars, *J. Cryst. Growth* **2009**, 311, 3817.
- [21] J. Dufouleur, C. Colombo, T. Garma, B. Ketterer, E. Uccelli, M. Nicotra, A. Fontcuberta i Morral, *Nano Lett.* **2010**, 10, 1734.
- [22] P. Xie, Y. Hu, Y. Fang, J. Huang, C.M. Lieber, *Proc. Natl. Acad. Sci. U.S.A.* **2009**, 106, 15254.
- [23] H. Morkoç, *Handbook of Nitride Semiconductors and Devices, Materials Properties, Physics and Growth*, John Wiley & Sons, Vol.1, **2008**.
- [24] M.A. Reshchikov, H. Morkoç, *J. Appl. Phys.* **2005**, 97, 061301.
- [25] P. Kozodoy, H. Xing, S.P. DenBaars, U.K. Mishra, A. Saxler, R. Perrin, S. Elhamri, W. Mitchel, *J. Appl. Phys.* **2000**, 87, 1832.
- [26] S. Khromov, C.G. Hemmingsson, H. Amano, B. Monemar, L. Hultman, G. Pozina, *Phys. Rev. B* **2011**, 84.
- [27] Z. Liliental-Weber, T. Tomaszewicz, D. Zakharov, J. Jasinski, M. O'Keefe, *Phys. Rev. Lett.* **2004**, 93.
- [28] B. Monemar, P. Paskov, G. Pozina, C. Hemmingsson, J. Bergman, T. Kawashima, H. Amano, I. Akasaki, T. Paskova, S. Figge, D. Hommel, A. Usui, *Phys. Rev. Lett.* **2009**, 102.

- [29] R. Juday, A. Fischer, Y. Huang, J. Huang, H. Kim, J.-H. Ryou, R. Dupuis, D. Bour, F. Ponce, *Appl. Phys. Lett.* **2013**, 103, 082103.
- [30] R. Carin, J. Deville, J. Werckmann, *Surf. Interface Anal.* **1990**, 16, 65.
- [31] T. Hashizume, *J. Appl. Phys.* **2003**, 94, 431.
- [32] H. Harima, *J. Phys.: Condens. Matter* **2002**, 14, R967.
- [33] T. Kozawa, T. Kachi, H. Kano, Y. Taga, M. Hashimoto, N. Koide, K. Manabe, *J. Appl. Phys.* **1994**, 75, 1098.
- [34] S. Bhattacharya, A. Datta, S. Dhara, D. Chakravorty, *J. Raman Spectrosc.* **2011**, 42, 429.
- [35] M. Reshchikov, J. McNamara, S. Fernández-Garrido, R. Calarco, *Phys. Rev. B* **2013**, 87, 115205.
- [36] B. Monemar, P.P. Paskov, G. Pozina, C. Hemmingsson, J.P. Bergman, S. Khromov, V.N. Izyumskaya, V. Avrutin, X. Li, H. Morkoç, H. Amano, M. Iwaya, I. Akasaki, *J. Appl. Phys.* **2014**, 115, 053507.

CHAPTER 5

ROLE OF OXYGEN IMPURITY ON GAS SENSING PROPERTIES OF GaN NANOWIRES

5.1 Introduction

Understanding the physical and chemical processes at the surfaces of semiconductor nanostructures is of paramount importance for developing nanostructure based energy and sensor devices. For example, by controlling the surface Fermi level pinning with different kinds of dopants in GaN and InGaN NWs, efficient H₂ evolution in photoelectrochemical water splitting has been realized for energy applications.^[1-3] Functionalization of semiconductor nanostructure surfaces with different metal clusters and functional groups resulted in highly sensitive and selective gas, chemical, and bio- sensor devices for sensing applications.^[4-6] The key chemical and physical processes involved in the aforementioned device operations are an absorption of photons or adsorption of gaseous molecules, subsequent charge transfer and charge transport on semiconductor surfaces.^[7] However, owing to the high surface to volume ratio in nanostructures, the complex behaviour of semiconductor nanostructure surfaces strongly influences the above three fundamental processes and alters the device performances.

For chemisorbed species during the sensing, the charge transfer on the surface is driven by the active sites available on the semiconductor surface.^[7] The active sites are governed by intrinsic and extrinsic defects in semiconductors, metal-semiconductor Schottky junctions or some functional groups attached to the surface. In the case of oxide semiconductor surfaces (SnO₂, ZnO, and TiO₂ and others), sensing takes place via chemisorbed oxygenated species (O₂⁻, O²⁻) serving as active sites for charge transfer and enhanced sensitivity. Similarly, the functionalized metal nanoparticles like Ag, Au, Pt and Pd

create active sites for the selective or low temperature sensing.^[7-11] Whereas, thermally stable and chemically inert pure group III- nitride semiconducting surfaces (such as GaN and AlGaN) utilize the Schottky junction with metal or heterojunctions with other semiconducting surfaces as active sites in the sensing process.^[4,12-18] Despite the potential applications of group III-nitride NWs as LEDs, lasers, HEMTs, logic gates, photodetectors, solar cells and sensors, the performances of these devices suffer from unintentional oxygen impurities.^[13,19-23] Extensive studies on unintentional oxygen impurities in group III-nitrides showed a strong influence of surface oxide on the sensing parameters of nitride devices, apart from the variations in structural, electrical and optical properties.^[19,20,24-27] Sensor device fabrication method itself has resulted in the metal-semiconductor junction with the presence of intermediate oxide layer. The gas sensitivity of such a device is enhanced by a factor of 50 as compared to that of the devices made without an oxide layer.^[24] The reported observations of sensing response by III-nitride NWs even without the assistance of any metal particles suggest the role of unintentional oxygen impurities on the chemical interactions at the semiconductor surface.^[24,28,29] However, the underlying mechanism has not yet been understood.

During the sensing process, the chemisorbed molecules on a semiconductor surface induce a bending of energy bands near the semiconductor surface.^[30] This surface band bending (SBB) can be precisely studied by the SKPM measurement. Apart from the type of semiconductor, the SBB (upward for *n*-type and downward for *p*-type) is strongly influenced by intrinsic and extrinsic defects, particle size, surface states, adsorbed gas or chemical molecules, incident photons, crystallographic orientations, surface reconstruction and temperature during the measurements.^[30-34] This method can therefore be utilized for understanding the chemisorption related sensing mechanism.

The detection of potential greenhouse gas CH₄ is extremely demanding in environmental safety.^[35] Here we report the underlying mechanism of methane (CH₄) sensing by GaN NWs and the role of surface defects formed by the oxygen impurities in the NWs. The presence of oxygen impurity and the type of possible oxygen defects in NWs are identified by the EELS studies. In this process, the EELS spectra corresponding to known oxygen defect complexes in GaN were simulated and compared with the experimental data to identify the type of oxygen defect complexes present in the GaN NWs. The gas sensing responses of the as-grown GaN NWs are tested by fabricating ensemble NW sensor devices, without any metal catalyst decoration on NWs. In order to understand the charge transfer process during the gas sensing, *in situ* SKPM measurements are carried out on single GaN NWs under CH₄ exposure.

5.2 Nanowires Synthesis and Characterization

5.2.1 Nanowire Synthesis:

Nonpolar GaN NWs having different oxygen concentrations were synthesized using APCVD technique in a VLS process. A detailed growth process, structural, compositional and optical study of GaN NWs with different oxygen impurity concentrations can be found in Chapter 3 (Section 3.3). Four NW samples were grown under different oxygen impurity concentrations of around 10⁵ ppm (sample R1), 10³ ppm (sample R2), 10² ppm (sample R3) and < 2 ppm (sample R4), for the present study.

5.2.2 Morphological and Structural Characteristics:

The typical morphologies of the as-grown NWs of the samples R1 (Fig. 5.1a), R2 (Fig. 5.1b), R3 (Fig. 5.1c) and R4 (Fig. 5.1d) were studied using FESEM (SUPRA 55 Zeiss). The NWs R1(Fig. 5.1a) and R2 (Fig. 5.1b), grown under oxygen rich atmospheres of 10⁵ and 10³ ppm,

respectively, are found to be quite rough with non-uniform surface morphologies along the wires. These NWs have a large diameter distribution of 40 – 150 nm. The diameter distribution of the NWs of sample R3 (Fig. 5.1c), grown under the low oxygen concentration of 10^2 ppm is reduced to 40 – 100 nm. The NWs R4 (Fig. 5.1d), grown under oxygen deficient atmospheres of < 2 ppm, showed uniform shape with homogeneous surface morphology and a narrow diameter distribution of $\sim 60(\pm 15)$ nm. The particle at the tip suggests that the growth of NWs followed the VLS process.

Typical TEM micrograph of NWs from the sample R1 shows an irregular surface morphology (Fig. 5.2a). The diffraction spots enclosed by dotted circles in FFT image (inset of Fig. 5.2b) corresponding to HRTEM micrograph of the NW, are indexed to $\{10\bar{1}0\}$ and

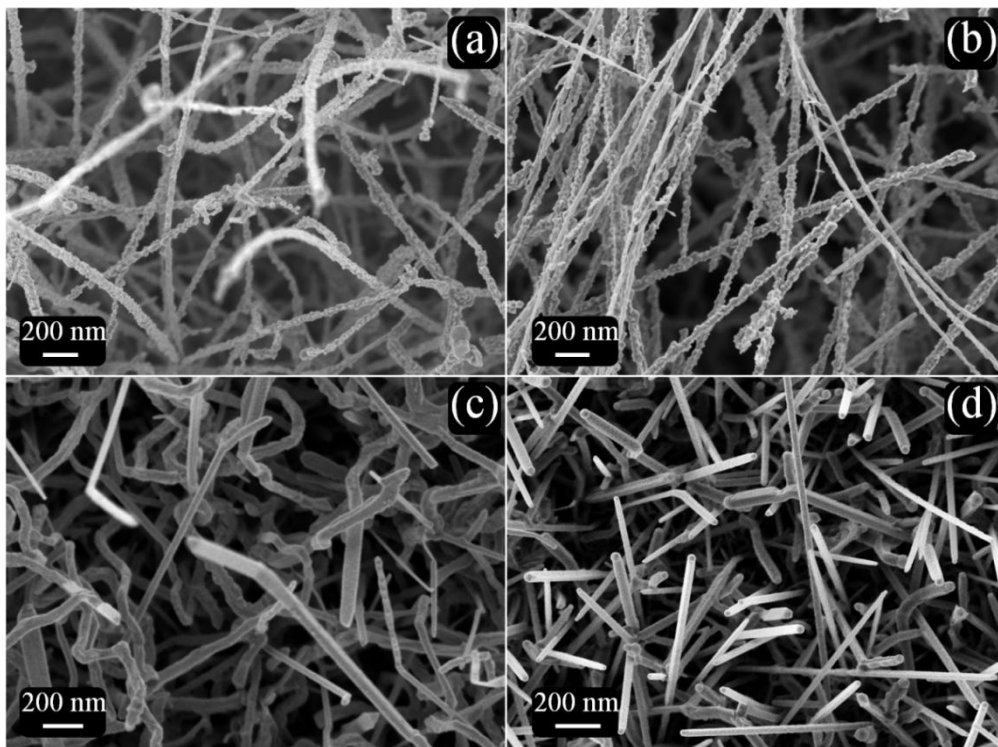


Fig. 5.1 Typical FESEM micrographs of GaN NWs grown under different oxygen concentrations of (a) $\sim 10^5$ ppm; sample R1, (b) $\sim 10^3$ ppm; sample R2. Both show quite rough and nonuniform surface morphology. (c) NWs grown under oxygen concentrations of $\sim 10^2$ ppm; sample R3 and (d) < 2 ppm; sample R4, having the uniform diameter and surface morphology along the NWs. Nanoparticles at the tip of the NWs are clearly observed.

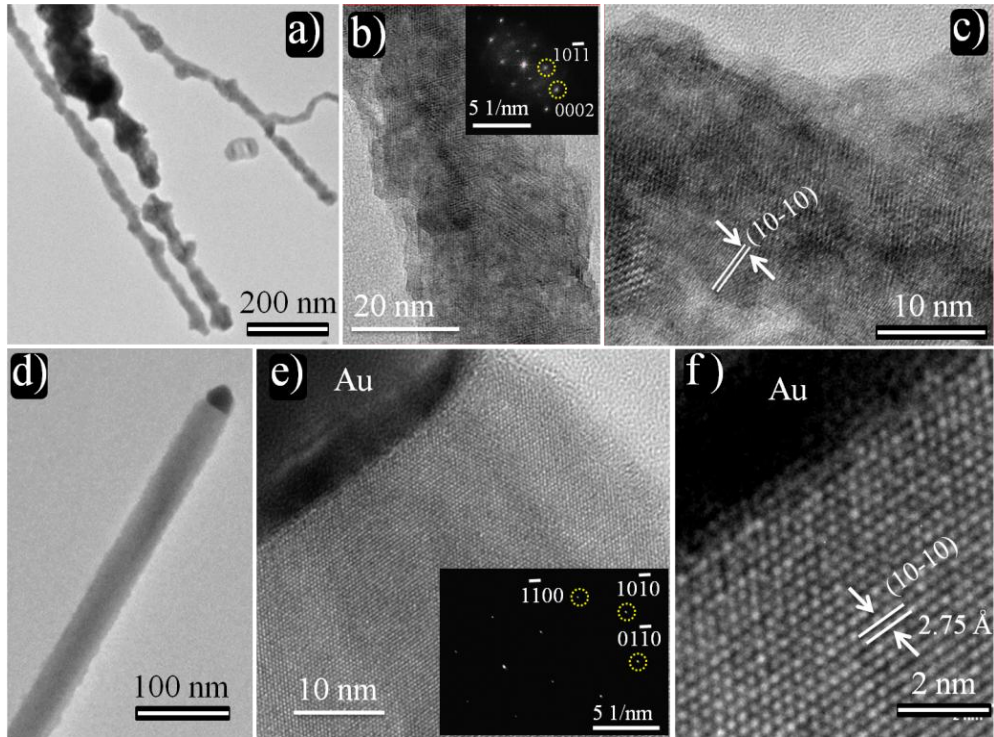


Fig. 5.2 Structural studies of the NWs: Sample R1; (a) Typical low magnification TEM image of NWs shows an irregular surface morphology, (b) HRTEM image of the NW with non-uniform contrast along the wire. Inset shows FFT image corresponding to HRTEM micrograph of the NW. (c) Magnified view of the HRTEM image of the NW with lattice fringes corresponding to $\{10\bar{1}0\}$ planes of GaN phase. Sample R4; (d) Low magnification TEM image of a typical NW, (e) HRTEM image collected near the tip of the NW having Au nanoparticle. Inset shows SAED pattern of the NW, indexed to wurtzite GaN with zone axis along $[0001]$ (f) Magnified view of HRTEM image shows the NW having nonpolar planes $(10\bar{1}0)$.

$\{0002\}$ planes of wurtzite GaN phase. High resolution image of the NW shows non-uniform contrast (Fig. 5.2b) which may originate from variation in thickness along the NW and barely seen for lattice fringes. Lattice fringes with d -spacing of 0.275 nm corresponding to $\{10\bar{1}0\}$ planes of GaN phase are observed in the magnified view (Fig. 5.2c) of high resolution image. A typical NW of the sample R4 shows a perfect rod like shape with uniform surface morphology (Fig. 5.2d) and having an Au catalyst particle on the tip. Uniform contrast along with sharp interface between GaN NW and Au catalyst particle is observed in the HRTEM image (Fig. 5.2e). The SAED pattern (inset of Fig. 5.2e) reveals that the NW is a single crystalline wurtzite phase of GaN with zone axes $[0001]$. An interplanar spacing of 0.275 nm,

shown in the magnified view (Fig. 5.2f), corresponds to the nonpolar $\{10\bar{1}0\}$ planes of wurtzite GaN. The growth direction of the NW is found to be along $[10\bar{1}0]$ direction.

5.3 Oxygen Defects Analysis by EELS Studies: Experiment and Simulation

The EELS experiments were carried out to identify the presence of N and O in NWs using an in-column second-order corrected omega energy filter type spectrometer with an energy resolution of 0.7 eV in a HRTEM (LIBRA 200FE Zeiss). Previous investigations on oxygen defects in GaN revealed that the most favorable defect states are $2(O_N)$ and $V_{Ga}-3(O_N)$.^[26,27,38,39] Existence of the oxygen impurity and the aforementioned lattice oxygen defects in NW samples were investigated by comparing the simulated and experimental EELS spectra of GaN NWs. It is worth mentioning that the EELS is highly sensitive to the presence of light elements as well as oxidation states. The experimental EELS spectra of all the NW samples were analyzed by collecting the *K*-edge emissions of N and O atoms. All the experimental core-loss spectra were background subtracted on the bases of power law energy dependence (AE^{-r}). The relative concentration of N to O atoms (n_N/n_O) in the NWs was estimated from the experimental EELS spectra. The n_N/n_O is found to be increased from oxygen rich (0.3 for R1) to oxygen deficient NWs (1.2 for R4). The N *K*-edge and O *K*-edge EELS spectra corresponding to $2(O_N)$ and $V_{Ga}-3(O_N)$ defects in GaN were then simulated and subsequently compared with the experimental spectra of GaN NWs grown under different oxygen impurity concentrations.

The EELS calculations were performed by the density functional theory (DFT) based Cambridge Sequential Total Energy Package (CASTEP) code in the Materials Studio (accelrys) package. The DFT+U calculations of the N *K*-edge and O *K*-edge EELS spectra were performed using the CASTEP code in the generalized gradient approximation (GGA)

and the projector augmented wave (PAW) method. Experimental lattice parameters of wurtzite GaN, $a = 3.189$, and $c/a = 1.626$ were used for the calculations. The Monkhorst – Pack k -point grid of $8 \times 8 \times 4$ and a plane wave energy cutoff value of 500 eV were chosen. A $2 \times 2 \times 2$ supercell with 32 atoms was considered. The O_N was created by replacing N with O atom and V_{Ga} was created by removing one Ga atom in the GaN supercell. A core hole was introduced in the $1s$ orbital of N and O atoms to calculate respective core-loss K -edge spectra. The N K -edge spectra for a simulated GaN structure with $2(O_N)$ and $V_{Ga}-3(O_N)$ defects were calculated by introducing a core hole in N atom situated in the vicinity of the defect.

A pure GaN structure projected along Z-axis \parallel (0001) is shown in Fig. 5.3a. The simulated N K -edge spectrum of pure GaN system is compared with the experimental N K -edge spectrum of sample R4 which is having the lowest oxygen concentration (Fig. 5.3a). Both the experimental and simulated spectra matched well except a small energy shift among the extended energy loss featuring around 425 eV. The ionization edge of N K -edge spectrum is found to be around 399 eV. The calculated N K -edge spectrum for the GaN structure with $2(O_N)$ defect is found to match with the experimental spectrum (Fig. 5.3b) of R3. Both the ionization edges and the near-edge fine structure features matched well. Similarly, the O K -edge spectrum of the simulated $2(O_N)$ defect state in GaN, was compared with that of the experimental data of R3 (Fig. 5.3b). The experimental spectrum is quite broad compared to the calculated spectrum, however, the near-edge and the extended energy loss features resembled that of the experimental data. The ionization edge of the O K -edge spectra is found to be around 531 eV.

Similarly, the K -edge spectrum (middle of Fig. 5.3c) was calculated for the N atom in the vicinity of $V_{Ga}-3(O_N)$ defect configuration in GaN structure (top of Fig. 5.3c) and is found to match closely with the experimental spectrum of the NWs of R1 including the near-edge features. The calculated O K -edge spectrum (bottom of Fig. 5.3c) of the $V_{Ga}-3(O_N)$

defect also matched well with that of the sample R1. It is worth mentioning that the clear near-edge fine structures of N and O *K*-edges (Fig. 5.3c) are observed for both the experimental and the simulated spectra. Thus the EELS study and simulations simulation helped in understanding the existence of the $2(O_N)$ and $V_{Ga}-3(O_N)$ oxygen defects in GaN NWs and also provided insights into their dependence on the concentration of oxygen impurity during the NW growth. An earlier study based on first-principles total energy calculations for the oxygen defects in GaN (surface oxygen coverage of about 10^{15} cm^{-2})

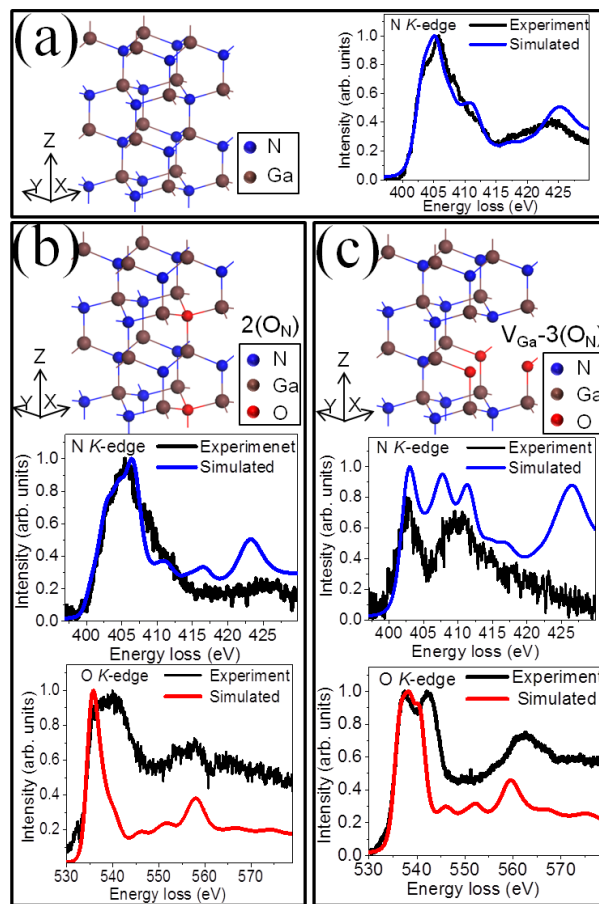


Fig. 5.3 Experimental and simulated EELS spectra of GaN NWs. (a) Right side; a simulated pure GaN structure, projected along Z-axis \parallel (0001) and Left side; the corresponding core loss N *K*-edge spectrum compared with that of the experimental spectrum collected from the NWs of sample R4. (b) Top; A simulated GaN lattice with $2(O_N)$ oxygen defect configuration, Middle and Bottom; simulated core loss N *K*-edge and O *K*-edge spectra, respectively, are compared with that of the experimental spectra collected from the NWs of sample R3. (c) Top; A simulated GaN lattice with $V_{Ga}-3(O_N)$ oxygen defect configuration, Middle and Bottom; simulated core loss N *K*-edge and O *K*-edge spectra, respectively, are compared with that of the experimental spectra collected from the NWs of sample R1.

showed that $2(O_N)$ and $V_{Ga-3}(O_N)$ defect configurations had low surface energies [0.5 – 1.7 eV/ (1×1) over a range of Ga chemical potential] in comparison to those of other defect states.^[38] Among the two lattice defect states, $2(O_N)$ is the stable configuration with low surface energy as compared to that of $V_{Ga-3}(O_N)$.

5.4 Nanowires Device Fabrication, Electrical and Gas Sensing properties

5.4.1 Device Fabrication:

The ensemble GaN NW sensor devices were fabricated by depositing interdigitated electrodes of Ti/Al/Ti/Au metal films on the mats of the as-grown NWs, at $\sim 10^{-6}$ mbar using the thermal evaporation technique. The Ohmic nature of the contacts was tested after annealing the devices at 400 °C for 5 min in an inert N_2 atmosphere. For room temperature and the *in situ* gas exposure SKPM measurements, pristine NWs were mechanically dry transferred from the NWs grown substrate to Au coated (~ 100 nm) conducting substrate.

5.4.2 Current–Voltage (*I-V*) Characteristics:

Prior to the gas sensing measurements of the GaN NWs, the nature of the electrical contacts to the NWs was studied using Agilent source measurement unit (B2902A) by measuring *I-V* characteristics of the fabricated ensemble NW devices. The *I-V* characteristics of the four devices, measured under -2 to +2 V bias, showed that the contacts are Ohmic in nature (Fig. 5.4). Resistances of the devices increased from 0.94 k Ω (sample R1) to 4.91 k Ω (samples R4) with a decrease in the oxygen concentration of the GaN NWs. This observation indicates a strong influence of background electrons produced by oxygen shallow donors acting as *n*-type dopants in GaN.^[27,40]

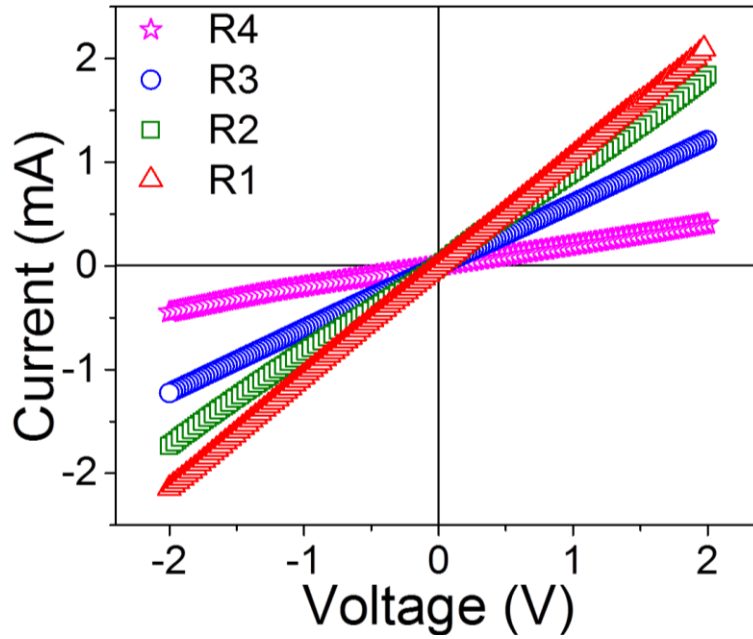


Fig. 5.4 The current-voltage characteristics of the four devices made of samples R1, R2, R3, and R4 measured under ± 2 V bias showing the contacts are Ohmic in nature and the increase in resistance for the samples R1 to R4.

5.4.3 Gas Sensing Properties:

Gas sensing by four devices made of NW samples R1, R2, R3, and R4 were carried out using a custom built in-house gas exposure facility under dynamic condition.^[36] In dynamic sensing, the gas was flown at a fixed flow rate over the sensor device while maintaining a fixed pressure in the sensing chamber under constant pumping using a dry pump. In the present case, responses of the devices were obtained at different concentrations and temperatures in the N_2 (99.999%) background at 10^{-2} mbar base pressure of the sensor chamber. Gas sensing properties for the four sensor devices made of the NW samples R1, R2, R3, and R4 were studied toward CH_4 (99.999%), a reducing gas. CH_4 is chosen ahead of the reducing gases like inflammable H_2 and corrosive NH_3 to have an ease in the handling, particularly, due to the limitation of SKPM chamber for the *in situ* measurement. The sensor response transients at different concentrations (50–500 ppm) of CH_4 and at different temperatures (50–150 °C) of the devices were recorded. The devices of sample R1, R2 and

R3 showed a significant response at 125 °C even at low concentration of 50 ppm gas exposure (Figs. 5.5a-c). In contrast, the device of sample R4 (Fig. 5.5d) did not respond even for 500 ppm. The sensor responses $(R_N - R_G / R_N) \times 100\%$ where R_N and R_G represent the resistances of the devices in N_2 background and sensing gas, respectively, are calculated. The maximum response at 500 ppm of CH_4 for the sensor devices of samples R1, R2 and R3 are 1.27 %, 0.87%, and 0.54 %, respectively. The gas responses of the devices were reproducible even after three months from the fabrication date. The responses of these devices are in the similar order of the reported values in case of the CH_4 sensing by GaN and SnO_2 NWs.^[9,13,29]

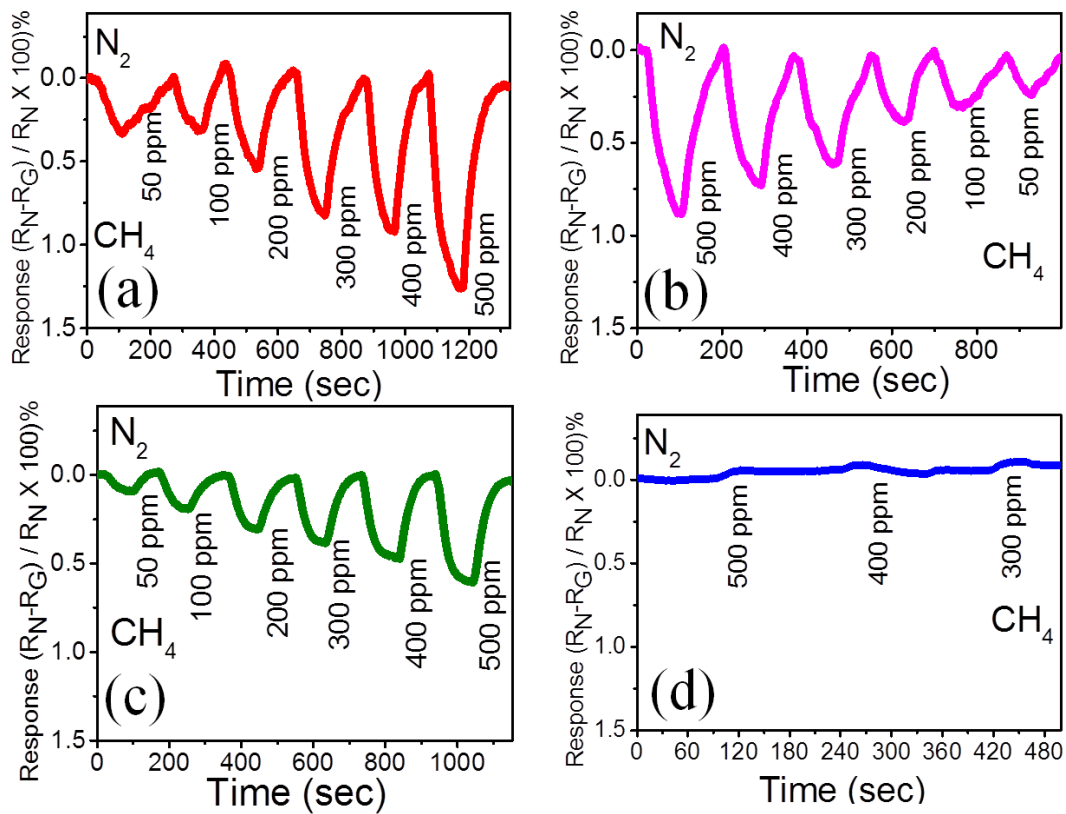


Fig. 5.5 Temporal responses of CH_4 sensing by four devices made of NW samples (a) R1, (b) R2, (c) R3, and (d) R4 at different gas concentrations at 125 °C .

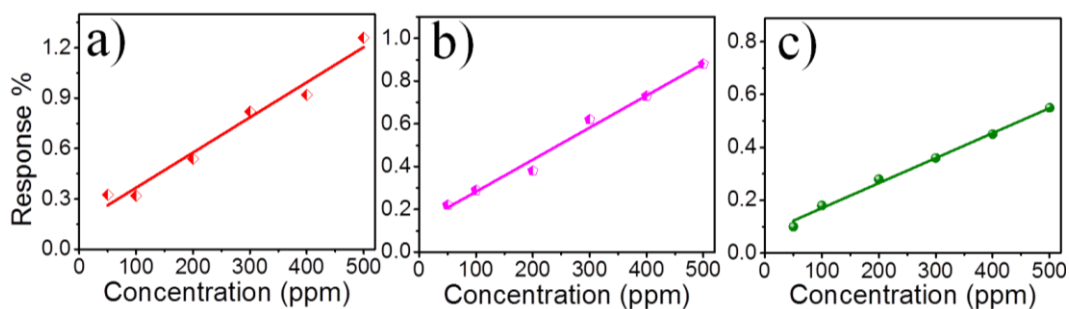


Fig. 5.6 The sensor response over a concentration range of 50 – 500 ppm of CH₄ for the device (a) R1, (b) R2, and (c) R3.

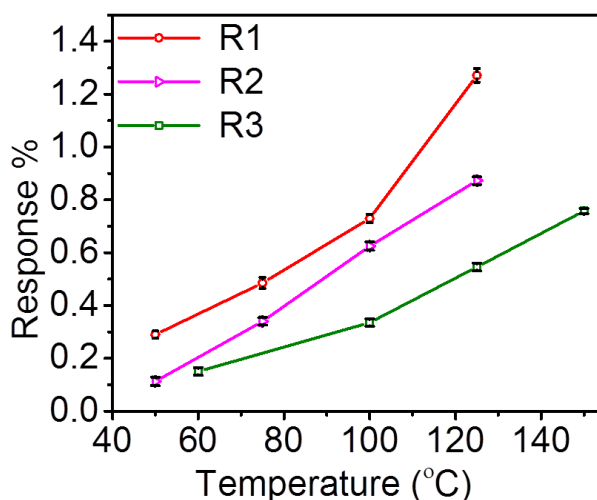


Fig. 5.7 Temperature dependent CH₄ sensing response by the devices of samples R1, R2 and R3 showing the increase in response with increasing temperature.

The three devices showed a linear response over a concentration range of 50 – 500 ppm of CH₄ (Fig. 5.6). There is a gradual reduction in the sensing response as the oxygen concentration in the GaN NWs is decreased from R1 to R3 (Fig. 5.5). Temperature dependent CH₄ sensing measurements showed increased amount of response with increasing temperature (Fig. 5.7). The lowest temperature at which the devices responded was 50 – 60 °C. The influence of temperature on the sensing response confirmed the chemisorption instead of physical adsorption of the CH₄ on NW surface.^[8] The increase in the temperature provides an activation energy for chemisorption induced sensor responses leading to an effective and efficient use of surface binding sites. It might be noted that the chemisorption of

CH₄ on the pure GaN surface did not occur even at high temperature without the assistance of a metal catalyst.^[6,14] However, the observed responses by the NW samples suggested the presence of active sites which might have driven the chemisorption of CH₄.

The active sites in GaN NWs could be lattice oxygen defects, which might have formed during the NW growth. For understanding the type of oxygen defects responsible for sensing by NWs, the results of EELS study were utilized. The experimental and simulated EELS studies revealed the existence of oxygen defects 2(O_N) and V_{Ga}-3(O_N) in the NWs. However, the presence of crystalline phase consisting of Ga and oxygen is ruled out from the Raman studies of ensemble and single GaN NW grown under oxygen rich condition (sample R1), as Raman modes corresponding to the oxide phase were not observed.^[41] This observation indicates that oxygen may only be present as point defects or its complexes. During the sensing experiments, the CH₄ adsorption occurred strongly on the NW surfaces due to 2(O_N) and V_{Ga}-3(O_N) defect states and the net charge transfer process took place between these defects and CH₄. The recovery process could therefore be explained by further adsorption of the residual oxygen, present in the exposure chamber, on the active sites involved in the sensing process.

5.5 SKPM Studies on Nanowires

5.5.1 Surface Potential Measurements of As-Grown Nanowires:

The SKPM studies were carried out for measuring the surface potential (SP) or the contact potential difference (CPD) on the NWs at room temperature using an Agilent 5500 with a three-lock-in amplifier setup. For the measurements, a V_{AC} bias at frequencies in the range 10-15 kHz plus a DC bias, V_{DC}, were applied between an electrically conductive tip (SCM-PIT; Pt-Ir coated Si tip). The samples in a controlled environmental chamber with humidity level below 15% were maintained by continuously flowing pure N₂.^[37]

The underlying mechanism of CH₄ sensing by GaN NWs, with various concentrations of lattice oxygen defects, is probed by studying the SP or the CPD variations on several NW surfaces using the SKPM technique. In SKPM mode, usually the CPD is compensated by applying external bias voltages that facilitate a simultaneous acquisition of topography and the surface potential SP.^[37] The CPD can be written as

$$V_{\text{CPD}} = (\phi_{\text{M}} - \phi_{\text{s}}) / q \quad (5.1)$$

where ϕ_{M} and ϕ_{s} are work function of the metal tip and the sample, respectively, and q is the elementary charge. The change in the work function of the sample directly reflects in the CPD values. As discussed earlier in the introduction, the SP measurements are influenced by several factors. The SP variations of the as-grown GaN NWs and the influential factors such as the diameter and impurity concentration in NWs were studied at room temperature prior to CH₄ exposure of the NWs.

Simultaneous topography and CPD (or SP) maps were acquired for the four NW samples R4 (Fig. 5.8a), R3 (Fig. 5.8b), R2 (Fig. 5.8c) and R1 (Fig. 5.8d). A typical topography map of NWs R4 (Fig. 5.8a, left side), grown under reduced oxygen atmosphere shows a quite smooth and homogeneous surface morphology along the NW having an average diameter ~ 60 nm. The corresponding SP map (Fig. 5.8a, right side) depicts the uniform SP contrast with an average value of $86 (\pm 2)$ mV, along the NW. As the concentration of the oxygen was increased during the growth (for samples R3, R2 and R1), the topography maps of NWs R3 (Fig. 5.8b, left side), R2 (Fig. 5.8c, left side) and R1 (Fig. 5.8a, left side) showed increased amount of surface roughness along the wires. The RMS roughness on these surfaces increased from ~ 8 to 26 nm for samples R4 to R1. The FESEM studies also qualitatively supported this observation (Fig. 5.1). The corresponding SP maps of NWs R3 (Fig. 5.8b, right side), R2 (Fig. 5.8c, right side) and R1 (Fig. 5.8d, right side) revealed the inhomogeneous SP contrast resembling topography variations along the

surface of the NWs. The SP variation could be due to different facets present in the rough morphologies.

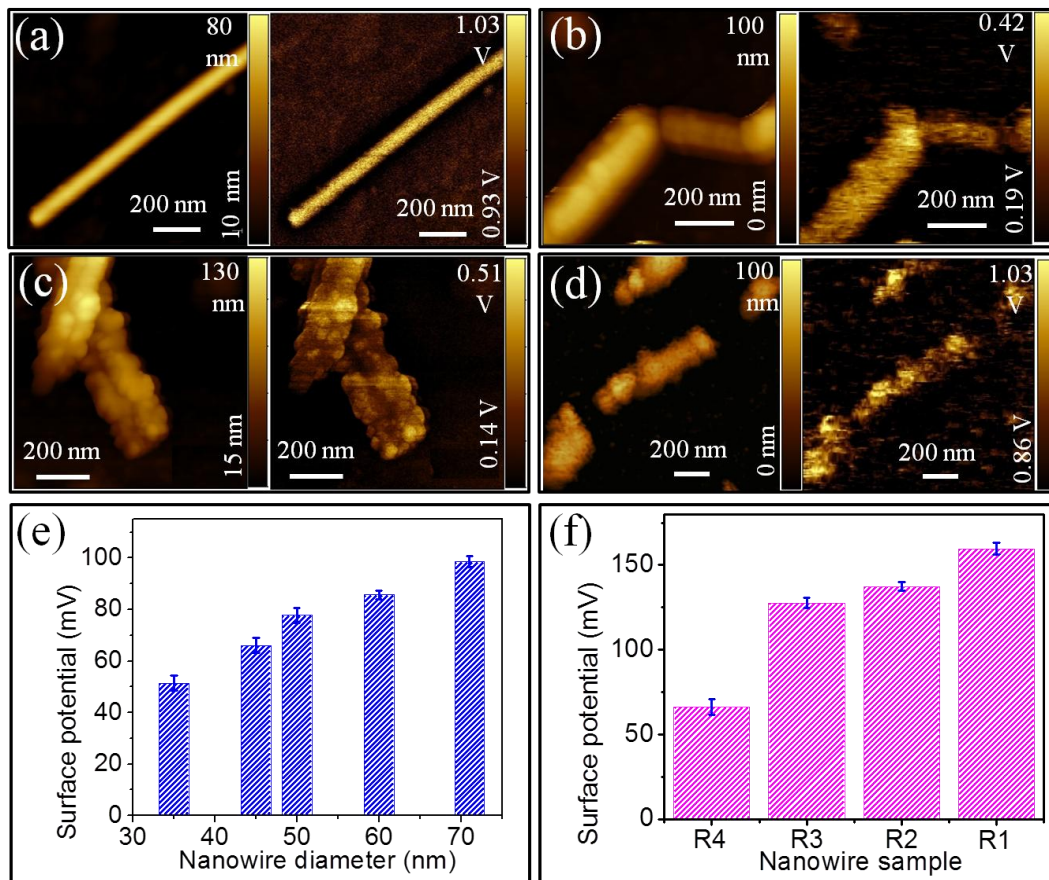


Fig. 5.8 Typical SKPM micrographs of NW samples (a) R4, (b) R3, (c) R2, and (d) R1. In all images, Left side; topography maps and Right side; SP maps. (e) NW diameter dependent SP values extracted from the SKPM maps of sample R4 and (f) SP plot of NWs samples R1, R2, R3, and R4 with different oxygen impurity.

A statistical analysis of SP values of NWs R4 with different diameters was also carried out. The results showed (Fig. 5.8e) an increase in the SP values with increasing NW diameter. This observation is in accordance to SBB due to the defects as explained below. GaN behaves as an *n*-type semiconductor due to the intrinsic V_N and unintentional substituent O at N site (O_N). The excess negative charges at the surface of an *n*-type semiconductor (GaN) cause the accumulation of positive charges near the surface leading to the formation of a space charge or the depletion region. In this case, the surface bands bend upward resulting

to a positive SP value. With an increase in the NW diameter, the surface charge density reduces for a fixed amount of doping concentration in R4. This reduction in the surface charge density also diminishes the accumulation of positive charges near the surface. Consequently, the resultant SP value is found to increase with increasing diameter (Fig. 5.8e). Statistics of SP values (Fig. 5.8f) of similar diameter (~ 45 nm) NWs with different oxygen concentration showed an increase in the SP value from 66 (± 4) to 160 (± 4) mV with increasing oxygen impurity in NWs (from samples R4 to R1). The increase in the SP values (more positive) with oxygen impurity is evident from the fact that the increased majority carrier concentration by oxygen donors reduces the upward band bending. So the SP values became more positive. Apart from the dopant concentration, the net SBB observed in oxygen rich NWs could be a result of the surface states and surface defects.

5.5.2 *in situ* SKPM Measurements Under Gas Exposure:

High temperature and *in situ* localized gas exposure studies on single NWs under vacuum were studied using the Nanonics Multiprobe (MultiView 4000) imaging system. Simultaneous topography and SP maps were acquired by using a two-lock-in amplifier setup. The first lock-in amplifier recorded the fundamental resonance frequency ($f_z \sim 68$ kHz) of Si probe and the second lock-in amplifier used the second order mechanical resonance frequency (~ 420 kHz) of the Si probe. For localized gas delivery of few picoliters (10^{-12} liters) of gas on a single NW, Nanonics (nonoptical normal-force feedback) tuning fork based ($f_z \sim 34.4$ kHz and Q-factor ~ 1080) FountainPen nanopipette gas delivery probe with aperture size ~ 200 nm was used. Thus, a dynamic condition was also simulated here as only few picoliters of gas were delivered in the large chamber volume of 1.5 liters.

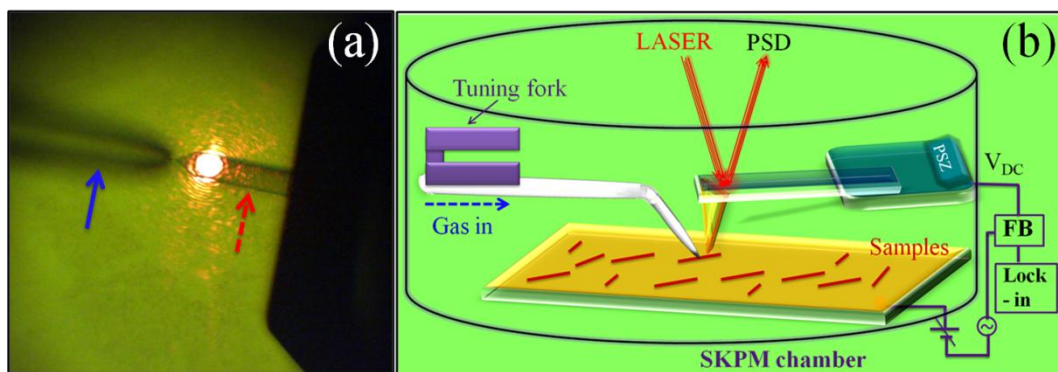


Fig. 5.9 (a) Optical image of the aligned two probes used for the *in situ* SKPM measurements under gas exposure. Cantilever based Au coated Si probe (dashed arrow line) with beam-bounce feedback is used for the SKPM measurements on NWs dispersed on Au film. Non-optical normal-force feedback is used for the tuning fork based nanopipette gas delivery probe (solid arrow line). (b) Schematic view of the SKPM study with the *in situ* gas exposure multiprobe setup.

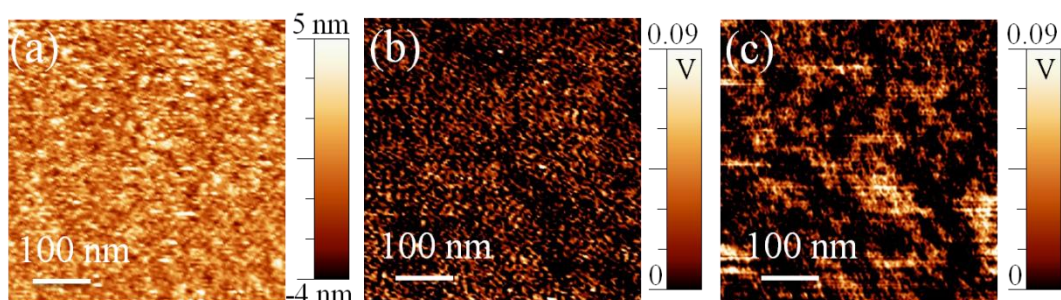


Fig. 5.10 SKPM measurements on standard Au film for calibration of Au coated Si tip at 100 °C under 10^{-2} mbar. (a) Topography maps; the RMS roughness is ~ 1.5 nm. SP maps (b) before and (c) during the CH_4 exposure; RMS values (CPD_{RMS}) before and during the gas exposure are ~ 28 mV and ~ 25 mV, respectively.

The local charge transfer mechanism in the CH_4 sensing is probed by acquiring SP or CPD maps of the NWs using SKPM with the *in situ* gas exposure multiprobe setup. A schematic view of the setup along with an optical image is shown (Figs. 5.9a,b). The setup consisted of a standard beam-bounce feedback cantilever based Au coated Si probe (dashed red arrow in Fig. 5.9a) for SKPM measurements which were carried out in an intermittent mode of AFM with a tip-sample distance of ~ 20 nm. By positioning the Kelvin probe and the gas delivery nanopipette probe (solid arrow line in Fig. 5.9a) facing in opposite and close to each other (Fig. 5.9a), under their respective feedback, simultaneous topography and CPD

maps were acquired with sample stage scanning. This arrangement allows us to expose the NWs to target gas locally, using a nanopipette probe and to measure the CPD on NWs using the SKPM probe.

Before proceeding to the SKPM measurements on the NW samples, Au coated Si tip was calibrated on pure Au film under similar conditions of the SKPM measurements. An absolute concentration of 1000 ppm CH₄ (99.999%) in N₂ (99.999 %) base gas was delivered through the nanopipette probe which allowed the exposure of few ppm of sensing gas mixture with respect to the volume of the SKPM chamber. The very low volume of the gas flown in few ppm levels did not alter the base pressure of the chamber ($\sim 10^{-2}$ mbar) over a period during the SKPM measurements. The RMS surface roughness value of ~ 1.5 nm for the Au film at 100 °C under 10^{-2} mbar (Fig. 5.10a) and the RMS value of CPD (CPD_{RMS}) ~ 28 mV (Fig. 5.10b) were measured without the CH₄ exposure. During the CH₄ exposure, the CPD_{RMS} value (~ 25 mV) was not changed considering the estimated error limit (Fig. 5.10c). The results showed that the tip work function did not change with the experimental conditions in the SKPM chamber.

Prior to the high temperature *in situ* SKPM measurements, the NW samples on Au substrate were kept in the SKPM chamber at $\sim 10^{-6}$ mbar pressure for 12 h in a dark condition and at room temperature. The samples were then heated to 125 °C for 2 h at $\sim 10^{-6}$ mbar pressure in dark and brought to the required SKPM measurement temperature and were allowed to stabilize for 2 h. The procedure helped the samples to dehumidify and stabilize the surface potentials. The SKPM measurements were carried out on two NW samples grown under two extreme cases of oxygen deficient (sample R4) and oxygen rich (sample R1) conditions among the four samples by maintaining similar experimental conditions of 100 °C at $\sim 10^{-2}$ mbar base pressure, at which gas sensing experiments were performed. Simultaneous

topography and CPD (or SP) maps were acquired before the CH₄ exposure as well as during the CH₄ exposure.

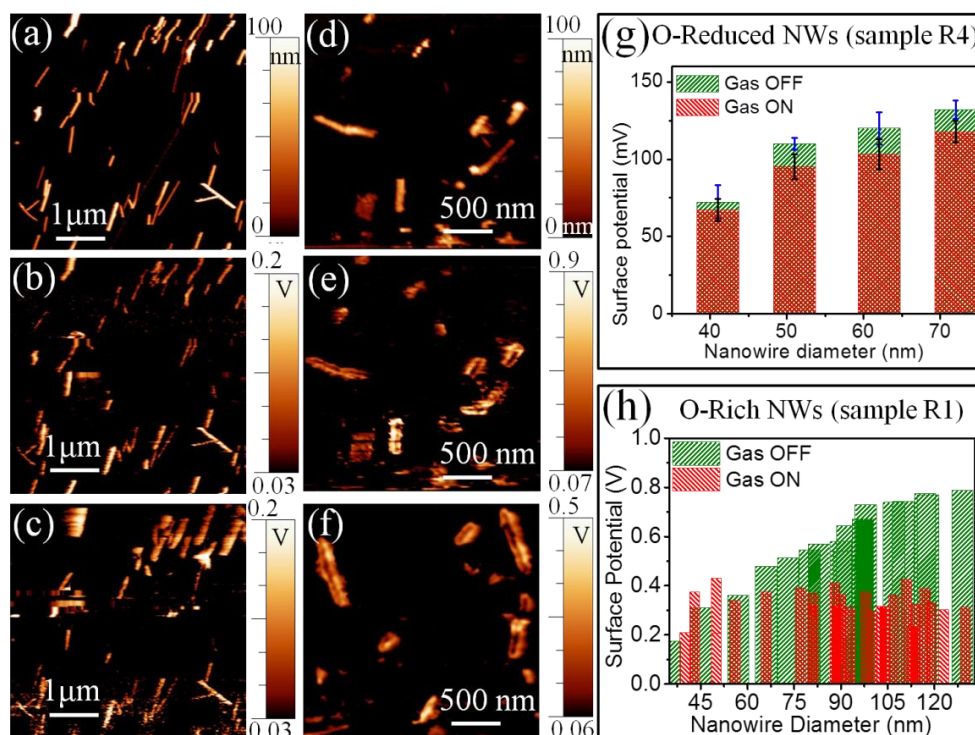


Fig. 5.11 Typical SKPM micrographs of NWs of sample R4 (Left side) and sample R1 (Right side) acquired at 100 °C and 10⁻² mbar. Topography maps of samples (a) R4 and (d) R1. Typical SP maps of samples (b) R4 and (e) R1 before CH₄ exposure. Typical SP maps of samples (c) R4 and (f) R1 during the CH₄ exposure. (g) and (h) NW diameter dependent SP values extracted from the SKPM maps of sample R4 and sample R1 respectively, before (green in color) and during the CH₄ exposure.

A typical topography map of NWs R4 (Fig. 5.11a), and the corresponding CPD maps before (Fig. 5.11b) and during (Fig. 5.11c) the CH₄ exposure are displayed. A statistical analysis of CPD values as a function of the NW diameter, both before and during the CH₄ exposure showed (Fig. 5.11g) that the CPD value increased with the increasing NW diameter. The CPD value, before the CH₄ exposure is found to increase from ~70 to ~130 mV when the diameter of the NW is increased from ~ 40 to ~70 nm. Variation in the CPD values in comparison to the values obtained at room temperature and atmospheric pressure (Fig. 5.8e) are expected due to the difference in work functions of the conducting tips, temperature and

base pressure of the SKPM chamber. However, the change in the CPD values due to CH₄ exposure [$\Delta V_{\text{CPD}} = V_{\text{CPD}} (\text{before}) - V_{\text{CPD}} (\text{during}) \text{CH}_4$], at a particular temperature and a base pressure with a fixed conducting tip was only considered. The CPD values are reduced to a range of ~ 65 - 117 mV, during the CH₄ exposure in the present measurement. It is worth mentioning that the ΔV_{CPD} values are very low (in the range of 5 - 17 mV) during the CH₄ exposure for any size of the NW diameter for the sample R4.

Similarly, a typical topography map of NWs for R1 (Fig. 5.11d), and the corresponding CPD maps before (Fig. 5.11e) and during (Fig. 5.11f) the CH₄ exposure were recorded at 100 °C and 10⁻² mbar. Statistical analysis of CPD values as a function of the NW diameter, before the CH₄ exposure (Fig. 5.11h) showed the similar trend of increase (~ 176 to ~790 mV) with increasing NW diameter (~35 to ~130 nm). Whereas the CPD values, during the CH₄ exposure lost the correlation with NW diameter and fluctuated in the range of ~ 210 - 430 mV with a mean saturation value of about 330 (± 59) mV for the entire range of NW diameter. Considering the saturation mean value of CPD (330 (± 59) mV) during the CH₄ exposure, we obtained the ΔV_{CPD} values before and during the gas exposure. The value of ΔV_{CPD} is found to be positive (+ 460 mV) for higher diameter NWs while it is negative ($\Delta V_{\text{CPD}} = -154 \text{ mV}$) for NWs with the smaller diameter. The changes in the CPD values, during the CH₄ exposure, are in the range of ~ 150 - 460 mV. Thus the ΔV_{CPD} of NWs R1, grown under oxygen rich atmosphere, is one order higher than that of R4 (5 - 17 mV) grown under reduced oxygen atmosphere.

The SBB due to the CH₄ exposure on GaN NWs of R1 was calculated by considering the highest possible amount of oxygen dopants of ~ 10²¹ cm⁻³ in GaN lattice.^[26] The SBB in dark can be written as

$$\Phi_{\text{B}} = \phi_{\text{M}} - qV_{\text{CPD}} + \phi_{\text{off}} - \chi + (E_{\text{c}} - E_{\text{f}}) \quad (5.2)$$

where ϕ_{off} is the offset in work function of the metal tip found by calibration (~ 28 meV) on Au film ($\phi_{\text{M}} = 5.1$ eV) and χ is electron affinity of the GaN (3.2 eV).^[34] E_{c} and E_{f} are positions of conduction band minimum and Fermi level, respectively. The estimated SBB in dark at 100 °C under 10^{-2} mbar base pressure, by measuring V_{CPD} before the CH_4 exposure, is found to be 1.57 - 0.95 eV over a range of NW diameters of 35 - 130 nm (Fig. 5.12a).

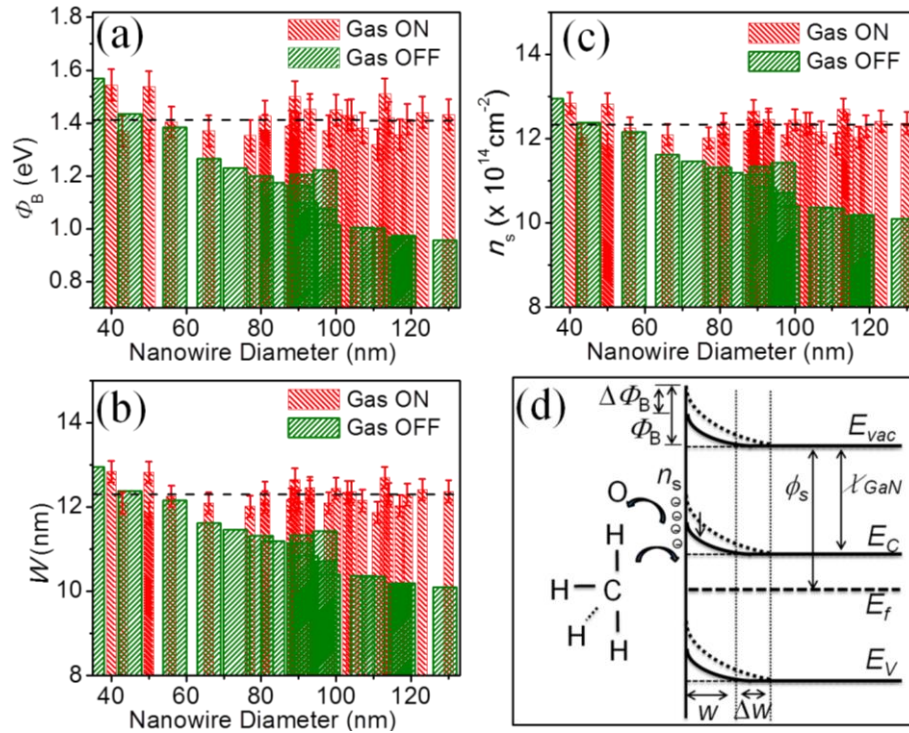


Fig. 5.12 NW diameter dependent (a) SBB (Φ_{B}), (b) depletion width (W) and (c) surface charge density (n_{s}) values extracted from the SKPM maps of sample R1, before (Green) and during (Red) the CH_4 exposure. Horizontal dashed lines indicate the mean saturation values in all the plots. (d) Schematic view of the band diagram of GaN NWs showing SBB (Φ_{B}) and charge transfer process during the chemisorptions of CH_4 .

The space charge region formed due to the SBB is characterized by the depletion width, W . The standard expression assuming the semi-infinite configuration instead of cylindrical geometry is chosen to calculate the depletion width considering the high surface roughness (~ 26 nm) which is a significant fraction of the NW diameter with non-uniform shape and surface morphology.^[42] Therefore,

$$W = (n_{\text{s}} / N_{\text{D}}) = (2 \Phi_{\text{B}} \epsilon_0 / q^2 N_{\text{D}})^{1/2} \quad (5.3)$$

where ϵ is the static dielectric constant of GaN (9.8),^[34] ϵ_0 is the permittivity of free space, N_D is dopant concentration, and n_s is surface charge density.

The calculated depletion width (W) (Fig. 5.12b) and the corresponding surface charge density (n_s) (Fig. 5.12c), before the gas exposure are 12.9 to 10.1 nm and 1.29×10^{15} to $1.01 \times 10^{15} \text{ cm}^{-2}$, respectively. During the CH_4 exposure, the estimated SBB, Φ_B is found to fluctuate and saturate on a mean value of 1.41 (± 0.06) eV over the range of NW diameters of 35 – 130 nm (Fig. 5.12a). Thus, W and n_s saturated at about the mean values of 12.3 (± 0.3) nm and $1.23 \times 10^{15} \text{ cm}^{-2}$, respectively following the eq. 5.3 (Figs. 5.12b,c). The saturated mean values show an increase in Φ_B , W and n_s for NWs with higher diameter when they are compared with the estimated values before the CH_4 exposure. The Φ_B and n_s due to the CH_4 exposure are increased by an amount of 0.46 eV and $2.2 \times 10^{14} \text{ cm}^{-2}$. As the NW diameter is decreased, the change in SBB ($\Delta\Phi_B$), W (ΔW), and n_s (Δn_s) values also get diminished.

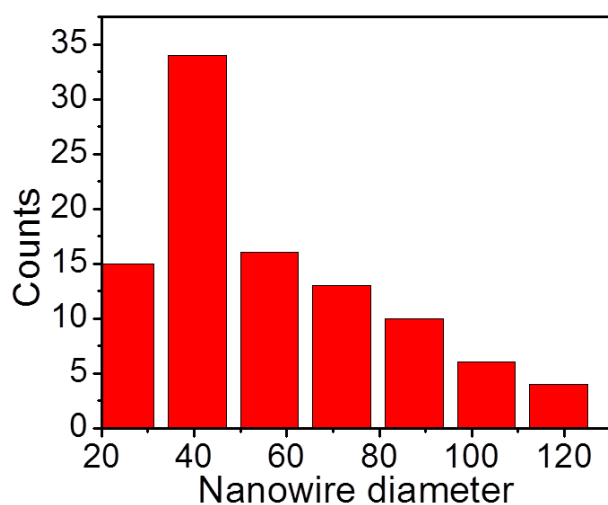


Fig. 5.13 Diameter distribution of NWs sample R1 grown under oxygen rich condition. A large number of NWs having the diameter less than 60 nm are present.

Below a critical diameter of ~ 60 nm, a trend of decrease in the mean values of Φ_B , W , and n_s is observed with respect to the estimated values of those before the CH_4 exposure. The Φ_B and n_s due to the CH_4 exposure are decreased by an amount of 0.16 eV and $6.0 \times 10^{13} \text{ cm}^{-2}$,

for NWs with the smaller diameter. A large number of NWs with small diameter (<60 nm) are present in the oxygen rich sample (R1; Fig. 5.13).

5.6 Charge Transfer and Surface Band Bending in Gas Sensing

The estimated changes in Φ_B , W , and n_s values were analyzed to understand the gas sensing mechanism in our chemiresistive measurements (Fig. 5.5). During the gas exposure, a charge transfer occurs between adsorbed CH_4 and the NW surface (Fig. 5.12d), which have active oxygen defect complexes of $2(\text{O}_\text{N})$ and $\text{V}_{\text{Ga}}-3\text{O}_\text{N}$. As discussed earlier, $2(\text{O}_\text{N})$ defects are more stable than the high energetic $\text{V}_{\text{Ga}}-3\text{O}_\text{N}$ defects.^[38] In such case, the $2(\text{O}_\text{N})$ defects are likely to be prevalent in the NWs with higher diameter (with lower surface-to-volume ratio) than that of the smaller ones. Due to the dominant presence of stable $2(\text{O}_\text{N})$ defects on the surface of the NW with higher diameter, the excess negative charges were therefore transferred by CH_4 accumulated on the surfaces. Thus, the surface charge density, n_s got increased (Fig. 5.12c) and it helped the surface bands to bend further upward from 0.95 to 1.41 (± 0.06) eV (Fig. 5.12a). As a result, the depletion width (W) increased in NWs with higher diameter (Fig. 5.12b).

A large surface energy is expected for the smaller diameter NWs because of their high surface-to-volume ratio in addition to the surface roughness (~26 nm for sample R1), which is a significant fraction for the case of small diameters. Calculated surface-to-volume ratios for the sample with rough (R1 with RMS roughness 26 nm) and smooth (R4 with RMS roughness 8 nm) surfaces for an area of $76 \times 76 \text{ nm}^2$ are found to be ~165 and ~15, respectively. Thus, the high energetic $\text{V}_{\text{Ga}}-3\text{O}_\text{N}$ defect complexes are ubiquitous on the surface of oxygen rich NWs of smaller diameter with high surface roughness as observed for the oxygen rich sample R1. In this context, it should be noted that the surface roughness only contributes to the enhancement of sensitivity of gas sensing by increasing the effective area

and does not contribute for the charge transfer process. Because of the dominant presence of less stable $V_{\text{Ga}}-3\text{O}_{\text{N}}$ defects, the lattice oxygen available in the defect complexes with sufficiently high surface energy participated in the electron transfer process with the CH_4 . Consequently, oxygen from the $V_{\text{Ga}}-3\text{O}_{\text{N}}$ complexes released out after receiving an electron from the CH_4 (Fig. 5.12d). So the net surface charge density, n_s was reduced resulting in the reduction of both SBB and depletion width values (Fig. 5.12). Although the calculated change in the local depletion width of smaller diameter NWs is low, the global change of depletion width is expected to be high due to the effective surfaces exposed to the CH_4 are large for smaller diameter NWs. As a result of the reduction in the depletion width, the conduction path of the majority carriers in the NW was enhanced leading to the improved carrier transportation. This process contributed to the resistive gas sensing measurement by lowering the total resistance during the CH_4 exposure. When the smaller diameter NWs with $V_{\text{Ga}}-3\text{O}_{\text{N}}$ surface defects are large in number, the corresponding resistance due to CH_4 exposure is found to decrease during the gas sensing measurements. The localized charge transfer process involving $V_{\text{Ga}}-3\text{O}_{\text{N}}$ defects, as observed in single NWs, may thus be responsible for controlling the global gas sensing for the oxygen rich ensemble of GaN NWs. Notably a decrease in the resistance is observed (Fig. 5.5) for the oxygen rich sample during the CH_4 exposure. When the CH_4 was switched off, the oxygen atoms present in the sensing atmosphere get adsorbed on the vacant O_{N} site resulting in the increase of the depletion width. As a result, the resistance of the devices recovers to the base level.

5.7 Summary

The resistive gas sensor devices made of GaN NWs with different oxygen impurity concentrations showed the response of reduction in resistance, toward CH_4 exposure. The experimental and the simulation of EELS studies on oxygen impurities in GaN NWs

confirmed the possible presence of $2(O_N)$ and $V_{Ga}-3O_N$ defect complexes. NW diameter dependent SKPM measurements showed a decrease in the SBB value with an increase in the diameter. A reduction in the SBB value is also observed as the oxygen concentration in NWs increases. The observed variations in SBB, depletion width, and surface charge density during the SKPM measurements on NWs exposed to CH_4 confirmed the occurrence of gas adsorption and charge transfer processes in these NWs. A localized charge transfer process, involving $V_{Ga}-3O_N$ defect complex in NWs is attributed to controlling the global gas sensing behavior of the oxygen rich GaN NW ensemble. Thus, by tuning the surface lattice oxygen defects on NWs, modulation of the sensing behavior of GaN NWs is demonstrated. The present results provide an insight for controlling the defects in III-nitride based nanostructures for advanced sensor device applications.

5.8 References

- [1] M.G. Kibria, S. Zhao, F.A. Chowdhury, Q. Wang, H.P. Nguyen, M.L. Trudeau, H. Guo, Z. Mi, *Nat. Commun.* **2014**, 5, 3825.
- [2] B. AlOtaibi, H.P. Nguyen, S. Zhao, M.G. Kibria, S. Fan, Z. Mi, *Nano Lett.* **2013**, 13, 4356.
- [3] D. Wang, A. Pierre, M.G. Kibria, K. Cui, X. Han, K.H. Bevan, H. Guo, S. Paradis, A.R. Hakima, Z. Mi, *Nano Lett.* **2011**, 11, 2353.
- [4] C.P. Chen, A. Ganguly, C.Y. Lu, T.Y. Chen, C.C. Kuo, R.S. Chen, W.H. Tu, W.B. Fischer, K.H. Chen, L.C. Chen, *Anal. Chem.* **2011**, 83, 1938.
- [5] Y. Cui, Q. Wei, H. Park, C.M. Lieber, *Science* **2001**, 293, 1289.
- [6] V. Dobrokhotov, D.N. McIlroy, M.G. Norton, A. Abuzir, W.J. Yeh, I. Stevenson, R. Pouy, J. Bochenek, M. Cartwright, L. Wang, J. Dawson, M. Beaux, C. Berven, *J. Appl. Phys.* **2006**, 99, 104302.
- [7] W. Göpel, K.D. Schierbaum, *Sensors and Actuators B* **1995**, 26, 1.
- [8] M. Bätzill, U. Diebold, *Prog. Surf. Sci.* **2005**, 79, 47.
- [9] V. Bonu, A. Das, A.K. Prasad, N.G. Krishna, S. Dhara, A. Tyagi, *Appl. Phys. Lett.* **2014**, 105, 243102.
- [10] D. Kohl, *Sensors and Actuators B* **1990**, 1, 158.
- [11] A. Hazra, K. Dutta, B. Bhowmik, P. Chattopadhyay, P. Bhattacharyya, *Appl. Phys. Lett.* **2014**, 105, 081604.
- [12] P. Sahoo, S. Dhara, S. Dash, S. Amirthapandian, A.K. Prasad, A. Tyagi, *Int. J. Hydrogen Energy* **2013**, 38, 3513.
- [13] W. Lim, J.S. Wright, B.P. Gila, J.L. Johnson, A. Ural, T. Anderson, F. Ren, S.J. Pearton, *Appl. Phys. Lett.* **2008**, 93, 072109.
- [14] S. Pearton, F. Ren, *Instrumentation & Measurement Magazine, IEEE* **2012**, 15, 16.

- [15] K.H. Baik, H. Kim, S.-N. Lee, E. Lim, S. Pearton, F. Ren, S. Jang, *Appl. Phys. Lett.* **2014**, 104, 072103.
- [16] P. Sahoo, S. Suresh, S. Dhara, G. Saini, S. Rangarajan, A.K. Tyagi, *Biosens. Bioelectron.* **2013**, 44, 164.
- [17] C. Lo, C. Chang, B. Chu, S. Pearton, A. Dabiran, P. Chow, F. Ren, *Appl. Phys. Lett.* **2010**, 96, 232106.
- [18] G.S. Aluri, A. Motayed, A.V. Davydov, V.P. Oleshko, K.A. Bertness, N.A. Sanford, M.V. Rao, *Nanotechnology* **2011**, 22, 295503.
- [19] S.J. Pearton, J.C. Zolper, R.J. Shul, F. Ren, *J. Appl. Phys.* **1999**, 86, 1.
- [20] M. Toth, K. Fleischer, M. Phillips, *Phys. Rev. B* **1999**, 59, 1575.
- [21] J. Wu, *J. Appl. Phys.* **2009**, 106, 011101.
- [22] Z. Zhong, F. Qian, D. Wang, C.M. Lieber, *Nano Lett.* **2003**, 3, 343.
- [23] F. Gonzalez-Posada, R. Songmuang, M. Den Hertog, E. Monroy, *Nano Lett.* **2012**, 12, 172.
- [24] O. Weidemann, M. Hermann, G. Steinhoff, H. Wingbrant, A. Lloyd Spetz, M. Stutzmann, M. Eickhoff, *Appl. Phys. Lett.* **2003**, 83, 773.
- [25] I. Arslan, N.D. Browning, *Phys. Rev. Lett.* **2003**, 91, 165501.
- [26] G.A. Slack, L.J. Schowalter, D. Morelli, J.A. Freitas Jr, *J. Cryst. Growth* **2002**, 246, 287.
- [27] M.A. Reshchikov, H. Morkoç, *J. Appl. Phys.* **2005**, 97, 061301.
- [28] F. Yun, S. Chevtchenko, Y.-T. Moon, H. Morkoç, T.J. Fawcett, J.T. Wolan, *Appl. Phys. Lett.* **2005**, 87, 073507.
- [29] V. Popa, I. Tiginyanu, V. Ursaki, O. Volcius, H. Morkoç, *Semicond. Sci. Technol.* **2006**, 21, 1518.
- [30] Z. Zhang, J.T. Yates Jr, *Chem. Rev.* **2012**, 112, 5520.

- [31] S. Barbet, R. Aubry, M.A. di Forte-Poisson, J.C. Jacquet, D. Deresmes, T. Mélin, D. Théron, *Appl. Phys. Lett.* **2008**, 93, 212107.
- [32] A. Soudi, C.-H. Hsu, Y. Gu, *Nano Lett.* **2012**, 12, 5111.
- [33] S. Chevtchenko, X. Ni, Q. Fan, A. Baski, H. Morkoc, *Appl. Phys. Lett.* **2006**, 88, 122104.
- [34] M. Foussekis, J.D. McNamara, A.A. Baski, M.A. Reshchikov, *Appl. Phys. Lett.* **2012**, 101, 082104.
- [35] G. Yvon-Durocher, A.P. Allen, D. Bastviken, R. Conrad, C. Gudasz, A. St-Pierre, N. Thanh-Duc, P.A. Del Giorgio, *Nature* **2014**, 507, 488.
- [36] A. Prasad, S. Amirthapandian, S. Dhara, S. Dash, N. Murali, A. Tyagi, *Sensors and Actuators B* **2014**, 191, 252.
- [37] P. Sahoo, D.S. Oliveira, M.n.A. Cotta, S. Dhara, S. Dash, A.K. Tyagi, B. Raj, *J. Phys. Chem. C* **2011**, 115, 5863.
- [38] J.E. Northrup, *Phys. Rev. B* **2006**, 73, 115304.
- [39] J. Elsner, R. Jones, M. Haugk, R. Gutierrez, T. Frauenheim, M. Heggie, S. Oberg, P. Briddon, *Appl. Phys. Lett.* **1998**, 73, 3530.
- [40] A. Ptak, L. Holbert, L. Ting, C. Swartz, M. Moldovan, N. Giles, T. Myers, P. Van Lierde, C. Tian, R. Hockett, *Appl. Phys. Lett.* **2001**, 79, 2740.
- [41] Z.-H. Lan, C.-H. Liang, C.-W. Hsu, C.-T. Wu, H.-M. Lin, S. Dhara, K.-H. Chen, L.-C. Chen, C.-C. Chen, *Adv. Funct. Mater.* **2004**, 14, 233.
- [42] R. Calarco, M. Marso, T. Richter, A.I. Aykanat, R. Meijers, V.D.H. A, T. Stoica, H. Luth, *Nano Lett.* **2005**, 5, 981.

CHAPTER 6

ROLE OF Mg DOPANTS IN PHOTORESPONSE OF *p*-GaN NANOWIRES

6.1 Introduction

Combining with other III-nitrides, GaN-based single and ensemble NW photoconductors and photodiodes paved the way for realizing photoresponse for wide wavelength range^[1,2] Besides, the absence of polarization-related electric fields in nonpolar III-nitride-based nanostructures provides a wider range of absorption wavelengths along with higher absorption probability compared to polar components.^[3,4] UV photodetectors with ultrahigh photocurrent gains up to 10^5 are demonstrated with nonpolar GaN and GaN/AlN single NWs.^[5-7] Further improvements on the functionalities of the NW devices could be achieved by forming heterojunctions with other electronic and optoelectronic materials. Earlier studies showed the feasibility of integrating GaN NW devices with other semiconducting materials such as Si and ZnO.^[8-13] There is also a report on the optoelectronic property of heterojunction devices (GaN/ZnO) that can be controlled by the interface polarity.^[8] The recent reports on integration of III-V nanostructures on Si show the possibility of vertical electronic and optoelectronic nano devices.^[14] However, electrical and optical characteristics of such heterojunction devices can be influenced by several device processing parameters which enhance the integration complexity.

Generally GaN based *p-n* junctions are found to have high diode ideality factors deviating from normal range of 1-2 according to Sah–Noyce–Shockley model.^[15,16] Such high values are attributed to various origins including quantum barriers in GaInN/GaN LEDs,^[16] sum of ideality factors of individual rectifying junctions in *p-n* junctions of GaN

and AlGaIn/GaN superlattice,^[17] and bandgap states formed by crystalline imperfections.^[18] A comparative study made between *p-n* diodes composed of GaN thin film and nanostructures revealed that the ideality factor could reach values as high as 20.^[19] Since it is possible that heterojunctions of GaN NWs can influence the carrier transport mechanism, ideality factors of the devices are therefore expected to vary. However, there is hardly any report on the variations in electrical and optical characteristics of such heterojunction devices.

In this chapter, a comparative study on ensemble and single nonpolar Mg-doped *p*-GaN NW and *n*-Si heterojunctions is presented. Particularly, photovoltaic and photoconducting mode characteristics of uniform-sized *p*-GaN NWs grown on *n*-Si(111) by APCVD method are analyzed and the key parameters including ideality factors, fill factors and responsivity of ensemble and single NW heterojunction devices are estimated for comparison.

6.2 Nanowire Synthesis, Characterization and Device Fabrication of Ensemble and Single *p*-GaN Nanowire and their Heterojunctions with *n*-Si

6.2.1 Mg Doped *p*-GaN Nanowires Synthesis:

Mg-doped nonpolar GaN NWs were synthesized by APCVD technique via the catalytic VLS process. The growth process as described in the Chapter 4, was followed to grow the NW.^[20] In brief, Ga metal (99.999%, Alfa Aesar), NH₃ gas (99.999%), and Mg₃N₂ (Alfa Aesar) were used for synthesizing Mg-doped GaN NWs. Nanowires were grown at 900 °C for one hour by purging 10 sccm of NH₃ (reactant gas) and 20 sccm of Ar (carrier gas) on *n*-Si(111) substrates containing Au nanoparticles. Mg dopants, for *p*-type conduction in GaN NWs, were activated by thermal annealing of the as-grown samples in UHP N₂ atmosphere at

750 °C for 30 minutes. Samples of undoped GaN NWs (*i*-GaN) on *n*-Si were also synthesized for comparison.

6.2.2 Morphological and Photoluminescence Characterizations of *p*-GaN Nanowires:

The FESEM (SUPRA 55 Zeiss) micrographs show the size distribution and arrangement of NWs (Fig. 6.1). Average diameter of the NWs was estimated to be 70 (± 10) nm. Particles at the tips of NWs confirm the growth involving VLS process (inset in Fig. 6.1). Our earlier studies on structural analysis by HRTEM revealed the predominant growth direction of [10-10] for Mg-doped GaN NWs in the wurtzite phase (Figs. 4.4b,c in Chapter 4).^[20]

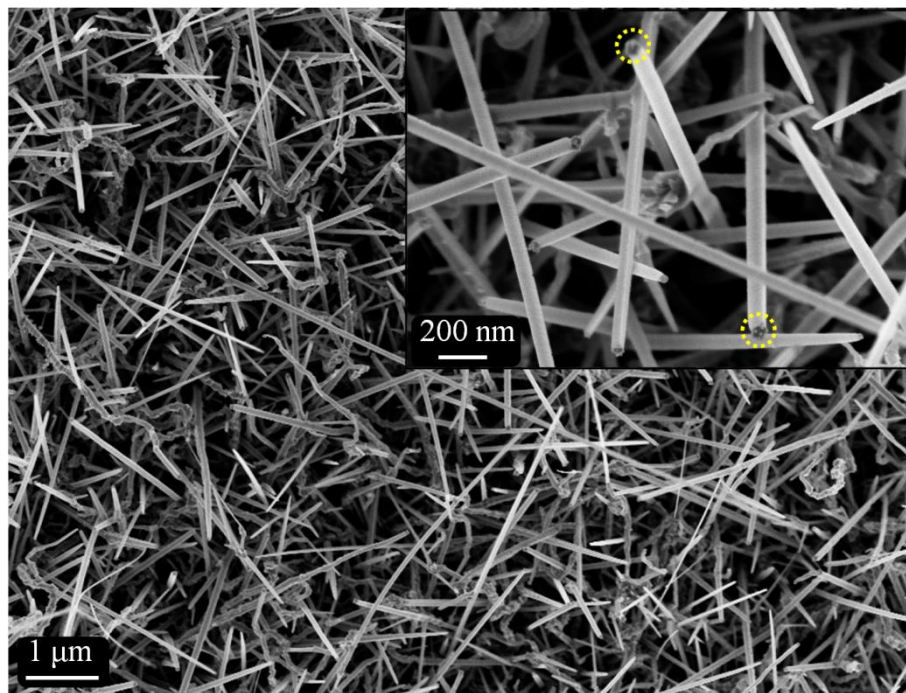


Fig. 6.1 FESEM image of Mg-doped *p*-GaN NWs on *n*-Si(111) substrate. Inset shows Au catalyst particles (encircled) at the tip of the wire.

The PL studies of ensemble *p*-GaN NWs were carried out at 80 K with an excitation wavelength of 325 nm of the He–Cd laser. The spectra were collected at different locations on the NWs sample. The spectra at 80 K show the UVL band around 3.0-3.3 eV and low intensity BL peak around 2.85 eV (Fig. 6.2). Both UVL and BL peaks are characteristics of

Mg doped GaN.^[21] The BL peak is assigned to transitions between shallow acceptors (Mg_{Ga}) and deep donors (V_N). The UVL band is due to DAP transitions involving shallow acceptors (Mg_{Ga}) and shallow donors. Intensity variations in BL peak and shift in the UVL position (Fig. 6.2) show the inhomogeneous dopant distribution in ensemble p -GaN NWs of the sample.

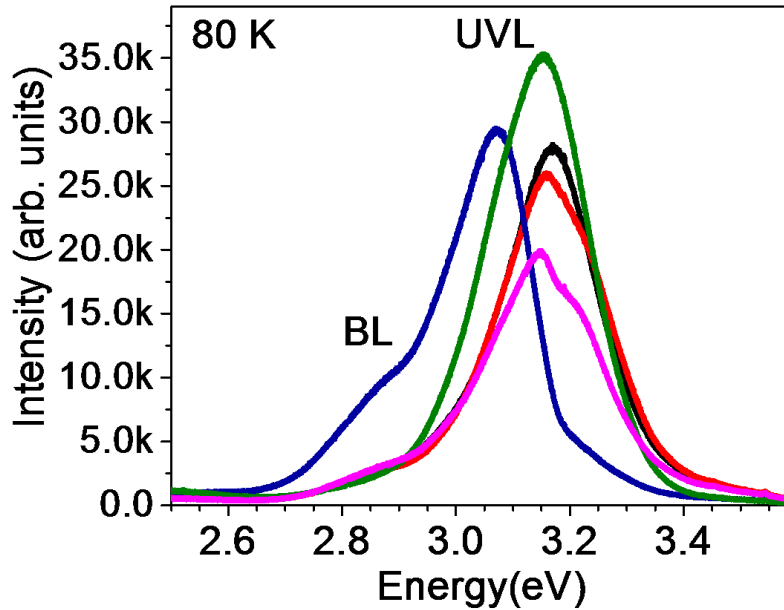


Fig. 6.2 The PL spectra of ensemble p -GaN NWs recorded at different locations on the sample at 80 K.

6.2.3 Ensemble and Single Nanowire device Fabrication:

Ensemble p -type GaN NW/ n -Si heterostructure devices were fabricated by depositing Au (100 nm)/Ni (25 nm) interdigitated electrodes (active area of 12 nm^2) onto the NWs using thermal evaporation and establishing an electrical contact with Si substrate by GaIn eutectic. Prior to the deposition of interdigitated electrodes, the substrate of ensemble NWs was coated with PMMA and then the top surface was exposed to acetone to remove a certain thickness of the PMMA layer to expose the NW tops. After depositing Au (100 nm)/Ni (25 nm) contacts on NWs, the PMMA was completely removed by dissolving in acetone. The electrode materials were chosen based on the work function of the metals and the semiconductor

material. The devices were annealed at 400 °C for 5 min in inert atmosphere to ensure Ohmic contacts. Similarly, ensemble NW devices consisting of *i*-GaN on *n*-Si were also fabricated by depositing Au/Ti/Al/Ti interdigitated electrodes for the reference purpose. The schematic (cross-sectional and 3D) views of the heterojunction device with interdigitated electrodes on ensemble NWs, in forward bias configuration are shown (Fig. 6.3).

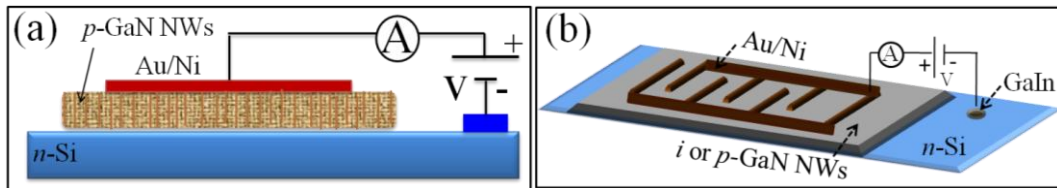


Fig. 6.3 (a) Cross-sectional and (b) 3D schematic views of the heterojunction device of *p*-GaN/*n*-Si in forward bias configuration

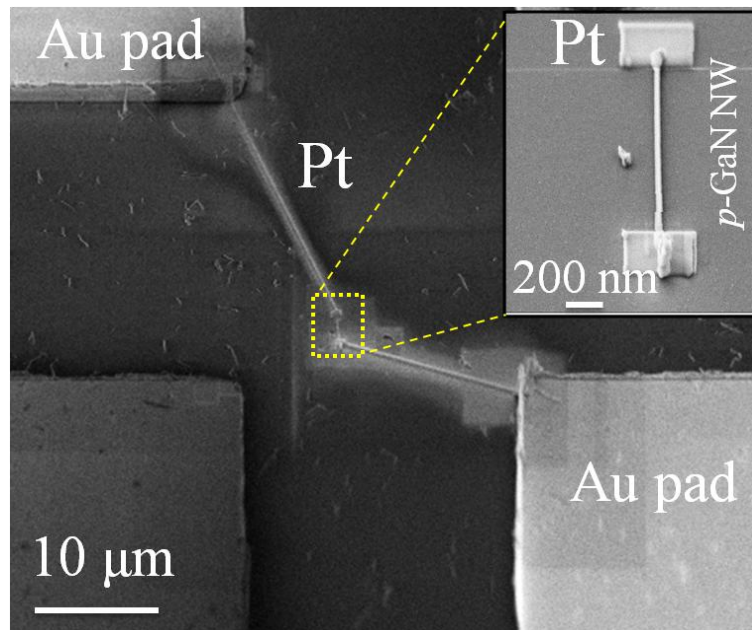


Fig. 6.4 FESEM micrograph of single *p*-GaN NW/*n*-Si heterojunction device. Inset shows the magnified view of *p*-GaN NW with electron beam deposited Pt (primary layer) electrodes.

A single *p*-type GaN NW/*n*-Si heterostructure device was fabricated by dual-beam FIB-SEM (AURIGA, Zeiss) technique on SiO₂ (300 nm) substrate patterned with Au/Cr pads (200 μm²). NWs were separated from the growth substrate and transferred to another SiO₂ (300

nm) coated Si substrate which contained pre-patterned 200 square microns Au/Cr pads. The NW was electrically connected to Au/Cr pads by Pt nano-strips deposited by FIB technique. Prior to the FIB deposition, small pads (1 X 0.6 μm) of Pt were deposited on both ends of the NW by electron beam in order to avoid the possible damage of the NWs by Ga^+ ion beam. Care was taken to minimize the spread of Pt out of the marked region, and for that a minimum possible ion current (5 pA at 30 kV) was used for deposition. A selective removal of SiO_2 just beneath the centre of NW was performed by ion beam to allow junction formation between p -GaN and n -Si. The FESEM micrograph of the single p -GaN NW/Si heterojunction device is shown in Fig. 6.4.

6.3 Electrical Characteristics of Nanowire Devices

6.3.1 Electrodes to n -Si, Ensemble and Single P -GaN Nanowire:

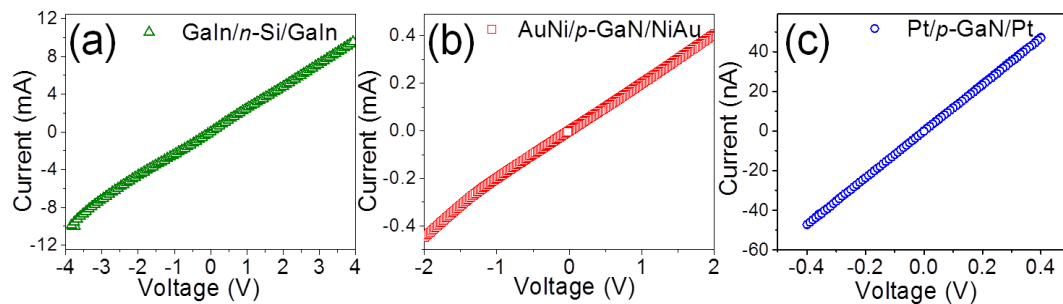


Fig. 6.5 I - V characteristics of (a) GaIn/ n -Si/GaIn, (b) AuNi/ p -GaN/NiAu and (c) Pt/ p -GaN/Pt under dark at 300 K showing Ohmic nature of the contacts.

Agilent source measure units (B2902A and B2911A) were used to record the I - V characteristics of all fabricated devices. The I - V characteristics of metal-semiconductor junctions were studied for individual semiconductors of n -Si, ensemble and single p -GaN NW. The study shows that the junctions GaIn/ n -Si/GaIn (Fig. 6.5a), AuNi/ p -GaN/NiAu (Fig. 6.5b) and Pt/ p -GaN/Pt (Fig. 6.5c) are Ohmic in nature. In general, Pt metal forms Schottky

junctions with GaN films, however, the FIB-deposited Pt contact is reported to be Ohmic for GaN NW with diameter below 100 nm.^[22]

6.3.2 Ensemble *p*-GaN NW/ *n*-Si Heterojunction Device:

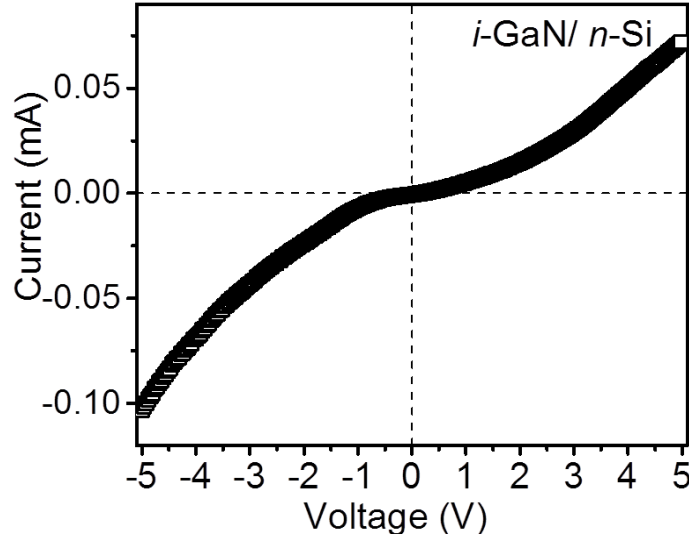


Fig. 6.6 Typical *I-V* characteristics undoped GaN NWs on *n*-type Si (*i*-GaN/*n*-Si) heterojunction device under dark.

The *I-V* characteristics of undoped GaN (*i*-GaN) NWs on *n*-type Si (*i*-GaN/*n*-Si) heterojunction show a typical Schottky behavior under -4 to +4 V bias (Fig. 6.6). A simple schematic band diagram could depict the formation of heterojunction between *p*-GaN/*n*-Si (Fig. 6.7). On applying -4 to +4 V bias, the *I-V* characteristics of *p*-GaN/*n*-Si device showed a *p-n* diode behavior under dark (Fig. 6.8a). In the forward bias, threshold voltage of the device is found to be ~ 0.7 V and rectification ratio under dark is found to be ~ 10^4 at ± 4 V. The *I-V* characteristics of a *p-n* heterojunction can be described by the equation, $I = I_0 [\exp (\frac{qV}{nk_B T}) - 1]$, where I_0 is reverse current, q is electron charge, k_B is Boltzmann constant, T is temperature and n is ideality factor.^[23] In low forward bias range of 0.2-0.5 V (Fig. 6.8a), calculated ideality factor is found to be 2. This shows that carrier transport is limited by generation-recombination processes.^[15] Reverse current in this region is about 10^{-9}

A. In the voltage range of 0.5-1.0 V, a very high ideality factor value of 10 is obtained and the reverse current is about 10^{-6} A.

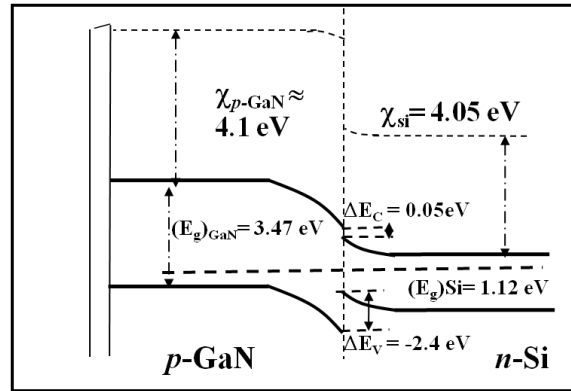


Fig. 6.7 A schematic band diagram for heterojunction between *p*-GaN NWs and *n*-Si.

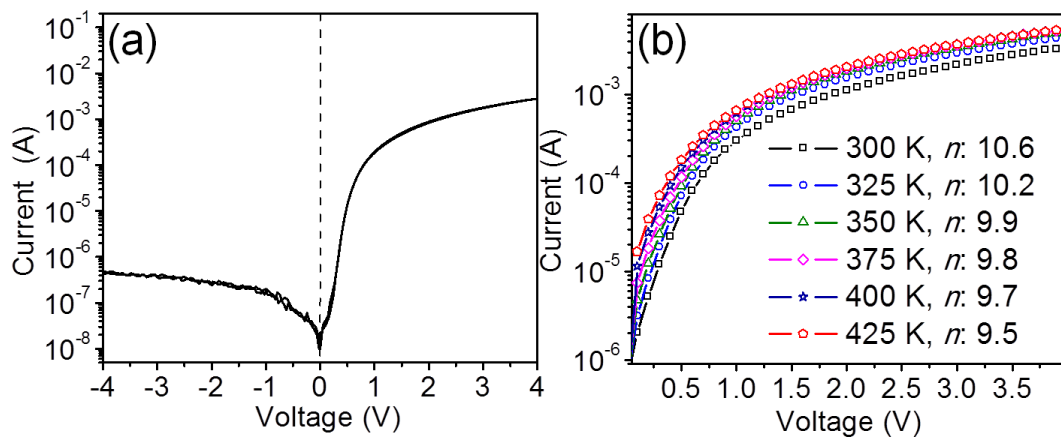


Fig. 6.8 (a) *I-V* characteristics of ensemble NW of *p*-GaN /*n*-Si heterojunction device under dark condition. (b) Temperature dependent forward bias *I-V* characteristics of the device under dark.

In general, deviation of *n* values from 1-2 of ideal *p-n* diodes can be understood by studying the temperature dependence of *n* and behavior of metal-semiconductor contacts. In present study, contacts for both *p*-GaN and *n*-Si were carefully formed with appropriate metals for individual semiconductors and the *I-V* characteristics of metal-semiconductor junctions (Figs. 6.5a,b) were found to be Ohmic in nature. Hence the contribution of metal-semiconductor junctions to *n* values is expected to be the minimum. High concentrations of Mg dopants could also reduce the series resistance of *p*-GaN NWs used for heterojunction

device. However, carrier diffusion through interfaces between NWs influencing the ideality factor cannot be ruled out because of the random orientations of *p*-GaN NWs. Dependence of *n* values on temperature was studied for ensemble *p*-GaN/*n*-Si heterojunction under dark condition (Fig. 6.8b). The *I*-*V* characteristics showed a decrease in the *n* value from 10.6 to 9.5 while increasing temperature from 300 to 425 K. Small reduction in the *n* value indicates that the measured electrical parameters are independent of the contacts and further confirms the Ohmic nature of the contacts.

Unusually high ideality factors in GaN *p*-*n* diodes are suggested to originate from bandgap states formed by deep-level impurities such as hydrogen complexes with Mg or native defects like V_N . In III-nitride based AlGaIn/GaN,^[17] and GaInN/GaN multiple quantum well LEDs,^[16] the origin was found to be GaN quantum barriers and individual rectifying junctions. In the present study, ensemble *p*-GaN/*n*-Si heterojunctions were fabricated in-situ during the growth of Mg-doped *p*-GaN NWs on *n*-Si. Therefore any excess and inhomogeneous incorporation of Mg dopants, while growing GaN NWs on Si, could modify the electrical properties of heterojunction. In fact, PL study at different locations of *p*-GaN NWs used in ensemble NW device showed shift in the donor DAP peak position (Fig. 6.2) indicating the inhomogeneity in Mg doping. Thus apart from deep-level impurities formed by Mg in *p*-GaN NWs,^[18] defect states due to inhomogeneity in doping of different GaN NWs can also increase the ideality factor of ensemble NW device consisted of large junctions.

6.3.3 Single *p*-GaN NW/ *n*-Si Heterojunction Device:

The electrical characteristics of ensemble *p*-GaN/*n*-Si heterojunction device were compared with single *p*-GaN NW/*n*-Si heterojunction device (Fig. 6.4). A cross-sectional schematic view of the device connected in a forward bias is depicted in Fig. 6.9. With an applied bias of -1 to +1 V between (one of the) Au/Cr contact pads of *p*-GaN NW and top-contact of *n*-Si,

the I - V characteristics of single NW device showed a p - n diode behavior under dark (Fig. 6.10a). Forward bias current was limited (with a maximum value of $3 \mu\text{A}$) to avoid any accidental breakdown of the device due to joule heating and/or spurious electrical spikes. In forward bias, turn-on voltage of the device is found to be $\sim 0.3 \text{ V}$ and rectification ratio under dark is higher than 10^4 at $\pm 1 \text{ V}$.



Fig. 6.9 A schematic cross-sectional side-view (along the NW) of a single NW p - GaN/n - Si heterojunction device in the forward bias configuration. Inset shows the cross-sectional (across the NW) front-view of the device.

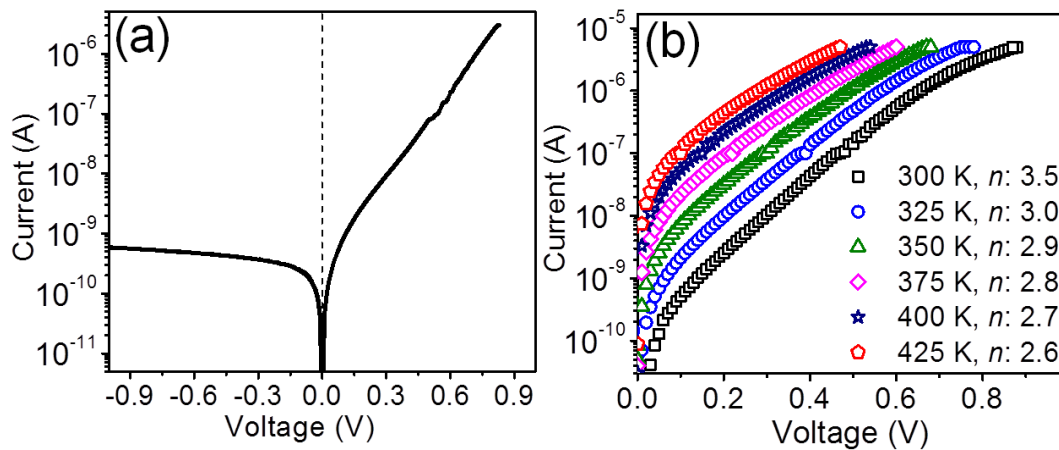


Fig. 6.10 (a) I - V characteristics of a single p - GaN NW/ n - Si heterojunction device under dark condition. (b) Temperature dependent forward bias I - V characteristics of the device under dark.

Using the diode equation, ideality factors were calculated for the single NW device with forward bias between 0.1 and 0.5 V under dark. In low bias range, 0.1-0.2 V, the ideality factor is 2.8 and reverse bias current is $2 \times 10^{-10} \text{ A}$ (Fig. 6.10a). The magnitude of ideality factor indicated the deviation of carrier transport from recombination processes. In high bias range, 0.2-1 V, the ideality factor is ~ 3.7 and reverse current is $\sim 3 \times 10^{-10} \text{ A}$. The ideality

factor of a single NW heterojunction device is significantly lower than the ensemble NW device in high bias range. The contribution of contacts for the ideality factor greater than 2 is ruled out, as the Ohmic contact is confirmed for Pt/*p*-GaN NW (Fig. 6.5c). Temperature dependence of the ideality factor of the single NW device was also studied under dark (Fig. 6.10b). The calculated n values show a decreasing trend from 3.5 to 2.6 with an increase in temperature from 300 to 425 K. A little decrease in n value could be due to slight improvement in Pt/*p*-GaN contact while increasing the temperature. In single NW device, role of defect states due to the inhomogeneity in dopant could be negligible. However, deviation of n value (>2) could be due to deep-level impurities formed by Mg in *p*-GaN NW as mentioned earlier. Reduction in the magnitude of ideality factor in single NW heterojunction compared to ensemble NW device could be due to the reduction in number of NWs with defect states caused by inhomogeneously doped *p*-GaN NW.

6.4 Photoresponse Properties of Nanowire Devices

6.4.1 Photodiode Characteristics of Ensemble *p*-GaN NW/*n*-Si Heterojunction

Device:

Ensemble nonpolar *p*-GaN NW/*n*-Si heterojunction device was examined to probe its photodiode characteristics. Photoresponse characteristics were studied under the illumination of 470 and 530 nm wavelengths with a bias voltage of -4 to +4 V. When the device is operated in the photovoltaic (PV) mode, the observed open circuit voltage (V_{oc}), short circuit current (I_{sc}) and fill factor (FF) for exposure with $\lambda = 470$ nm are 300 mV, 1 μ A and 54 %, respectively. While for exposure with $\lambda = 530$ nm, V_{oc} , I_{sc} , and FF are 310 mV, 0.8 μ A and 56% respectively (Fig. 6.11a). When the device was operated in the photoconducting (PC) mode in reverse bias, a change in reverse bias current was observed for both the wavelengths (Fig. 6.11a). Temporal response of the device (Fig. 6.11b) showed that the maximum

responsivity (R_λ) is 69 mA/W at 470 nm whereas 18 mA/W at 530 nm. The corresponding external quantum efficiencies were 18.2 % and 4.2 % for 470 and 530 nm, respectively.

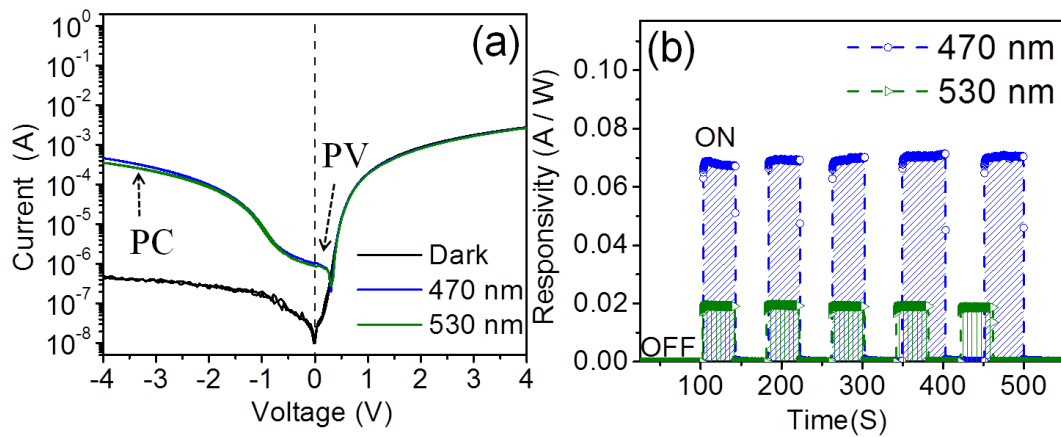


Fig. 6.11 (a) I - V characteristics of ensemble NW of p -GaN/ n -Si heterojunction device under dark and illumination of different wavelengths. (b) Temporal photoresponse of the ensemble NW device under the illumination of 470 and 530 nm with light ON and OFF.

All data corresponding to electrical and photodiode characteristics are tabulated for comparison (Table 6.1). Under the equilibrium condition, the energy bands of both the semiconductors get aligned such that the Fermi levels coincide on both sides of the heterojunction (see schematic band diagram Fig. 6.7). PV effect at zero bias showed separation of photogenerated carriers due to built-in potential at the junction between p -GaN NWs ($E_g = 3.47$ eV) and n -Si ($E_g = 1.12$ eV).^[10] Carrier generation with photon energies less than the bandgap of GaN (3.47 eV ≈ 357 nm) indicates the possible injection of charge carriers from n -Si. Whereas the enhanced photoresponse for exposure of 470 nm as compared to that of 530 nm (Fig. 6.11a), when the device was operated in the PC mode at a reverse voltage of 4 V, showed the possibility of larger photocurrent generation due to sub-bandgap states formed by Mg doping in p -GaN NWs. Earlier studies on spectral response of PC measurements on GaN NWs revealed similar defect related photocurrent for sub-bandgap excitations.^[24] In fact, PL studies on p -GaN NWs used in present study, showed the available electronic states which might be responsible for photocurrent (Fig. 6.2). With increased

reverse bias voltage in the PC mode, the enhanced collection of photo generated carriers in *p*-GaN NWs due to sub-bandgap states could enhance the responsivity.

6.4.2 Photodiode Characteristics of Single *p*-GaN NW/*n*-Si Heterojunction Device:

Single *p*-GaN NW/*n*-Si heterojunction device (active area of $\sim 7 \times 10^4 \text{ nm}^2$) was analyzed to explore its photodiode characteristics. Similar to ensemble NW device, the photoresponse was tested under the illumination of 470 and 530 nm wavelengths. When the device was operated in the PV mode (Fig. 6.12a), maximum V_{oc} of 100 mV was observed for 470 nm while for 530 nm, V_{oc} was 70 mV. I_{sc} under the exposure of 470 and 530 nm were found to be 3.5 and 1.1 nA, respectively. Fill factors of 32 and 31 % were calculated for 470 and 530 nm, respectively. These values are comparable to the reported values of $\sim 38\%$ for ensemble *p*-GaN NW/*n*-Si devices.^[10] When the device was operated in the PC mode, a change in reverse bias current was observed for both wavelengths (Fig. 6.12a). Temporal response of the device shows (Fig. 6.12b) the maximum responsivity of 1675 A/W at 470 nm and 197 A/W at 530 nm. These high responsivity values yield high photocurrent gains. All the data for single NW device are tabulated in Table 6.1 to compare with the ensemble NW device.

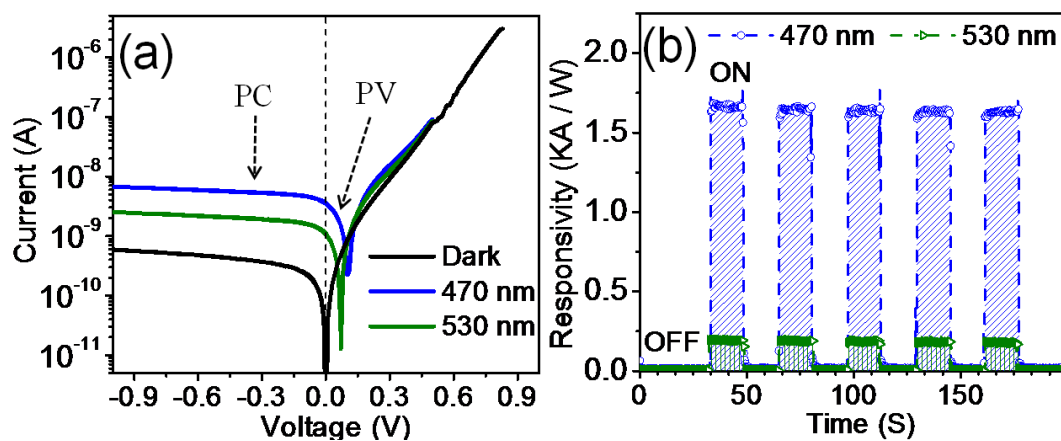


Fig. 6.12 (a) *I-V* characteristics of single *p*-GaN NW/*n*-Si heterojunction device under dark and illumination of different wavelengths. (b) Temporal photoresponse of the device under illumination of 470 and 530 nm wavelengths.

Table 6.1 Comparison of electrical and photodiode characteristics of ensemble and single *p*-GaN NW/*n*-Si heterojunctions.

Measured parameters	Ensemble NWs device	Single NW device
Electrical characteristics:		
Threshold voltage (V_{th})	0.7 V	0.3 V
Rectification ratio	10^4	10^4
Ideality factors (n)	2 for 0.2 - 0.5 V range 10 for 0.5 - 1 V range	2.8 for 0.1 - 0.2 V range 3.7 for 0.2 - 1 V range
Photovoltaic mode: (At $\lambda = 470$ and 530 nm)		
Open circuit voltage (V_{oc})	300 and 310 mV	100 and 70 mV
Short circuit current (I_{sc})	1.0 and 0.8 μ A	3.48 and 1.06 nA
Fill Factor (FF)	56 % and 64%	32 % and 31 %
Photoconducting mode: (At $\lambda = 470$ and 530 nm)		
Responsivity (R_{λ})	0.069 and 0.018 A/W	1675 and 197 A/W
External quantum efficiency (or) Photocurrent gain	18.2 % and 4.2 %	4.4×10^3 and 4.6×10^2

High responsivity and photocurrent gain values for above bandgap excitation energies are reported earlier for single GaN NW photoconductors,^[5-7] as well as for photodiodes.^[10] In present study, however the excitation energies were less than the bandgap energy of GaN. Besides, the geometry of single NW device could also allow *p*-GaN NW to be fully exposed to incident photons and contribute for surface conduction, therefore enhancing the photoresponse in the PC mode.^[10] As mentioned in case of ensemble NW device, high photoresponse for below sub-bandgap excitation energies could be due to the carriers generated by Mg-doping-induced sub-bandgap states in *p*-GaN NWs.^[24] Besides, the geometry of single NW device can also allow *p*-GaN NW to be fully exposed to incident photons, therefore enhancing the photoresponse in the PC mode. A drastic increase in the

responsivity of the single NW device compared to ensemble NW device confirms the role of sub-bandgap states in the carrier conduction mechanism.

6.5 Summary

In conclusion, ensemble and single Mg-doped nonpolar *p*-GaN NW/*n*-Si heterojunction devices were fabricated and their electrical and photodiode characteristics were compared. High ideality factor of 10 is observed for an ensemble *p*-GaN NW/*n*-Si device. The defect states due to deep-levels and inhomogeneity in Mg dopants are attributed to the increase in ideality factor. Photovoltaic mode of ensemble NW device showed an improvement in the fill-factors up to 60 % over the single NW device with fill-factors up to 30 %. Responsivity of the single NW device in photoconducting mode is found to be enhanced by five orders. The enhanced photoresponse of the single NW device also confirms the photoconduction due to the presence of sub-bandgap states in *p*-GaN NWs.

6.6 References

- [1] A.D.L. Bugallo, L. Rigutti, G. Jacopin, F.H. Julien, C. Durand, X.J. Chen, D. Salomon, J. Eymery, M. Tchernycheva, *Appl. Phys. Lett.* **2011**, 98, 233107.
- [2] M.d. Hertog, R. Songmuang, F. Gonzalez-Posada, E. Monroy, *Jpn. J. Appl. Phys.* **2013**, 52, 11NG01.
- [3] P. Waltereit, O. Brandt, A. Trampert, H. Grahn, J. Menniger, M. Ramsteiner, M. Reiche, K. Ploog, *Nature* **2000**, 406, 865.
- [4] D. Feezell, Y. Sharma, S. Krishna, *J. Appl. Phys.* **2013**, 113, 133103.
- [5] R.-S. Chen, H.-Y. Chen, C.-Y. Lu, K.-H. Chen, C.-P. Chen, L.-C. Chen, Y.-J. Yang, *Appl. Phys. Lett.* **2007**, 91, 223106.
- [6] R.S. Chen, H.Y. Tsai, Y.S. Huang, Y.T. Chen, L.C. Chen, K.H. Chen, *Appl. Phys. Lett.* **2012**, 101, 113109.
- [7] L. Rigutti, M. Tchernycheva, A. De Luna Bugallo, G. Jacopin, F.H. Julien, L.F. Zagonel, K. March, O. Stephan, M. Kociak, R. Songmuang, *Nano Lett.* **2010**, 10, 2939.
- [8] F. Furtmayr, M. Vielemeyer, M. Stutzmann, A. Laufer, B.K. Meyer, M. Eickhoff, *J. Appl. Phys.* **2008**, 104, 074309.
- [9] F. Schuster, B. Laumer, R.R. Zamani, C. Magén, J.R. Morante, J. Arbiol, M. Stutzmann, *ACS nano* **2014**, 8, 4376.
- [10] G. Jacopin, A. De Luna Bugallo, L. Rigutti, P. Lavenus, F.H. Julien, Y.-T. Lin, L.-W. Tu, M. Tchernycheva, *Appl. Phys. Lett.* **2014**, 104, 023116.
- [11] M. Tchernycheva, A. Messanvi, A. de Luna Bugallo, G. Jacopin, P. Lavenus, L. Rigutti, H. Zhang, Y. Halioua, F.H. Julien, J. Eymery, C. Durand, *Nano Lett.* **2014**, 14, 3515.
- [12] Y. Tang, Z. Chen, H. Song, C. Lee, H. Cong, H. Cheng, W. Zhang, I. Bello, S. Lee, *Nano Lett.* **2008**, 8, 4191.

- [13] Y.Q. Bie, Z.M. Liao, H.Z. Zhang, G.R. Li, Y. Ye, Y.B. Zhou, J. Xu, Z.X. Qin, L. Dai, D.P. Yu, *Adv. Mater.* **2011**, 23, 649.
- [14] K. Tomioka, T. Fukui, *J. Phys. D: Appl. Phys.* **2014**, 47, 394001.
- [15] R.-Y. Sah, R.N. Noyce, W. Shockley, *Proc. IRE* **1957**, 45, 1228.
- [16] D. Zhu, J. Xu, A.N. Noemaun, J.K. Kim, E.F. Schubert, M.H. Crawford, D.D. Koleske, *Appl. Phys. Lett.* **2009**, 94, 081113.
- [17] J.M. Shah, Y.L. Li, T. Gessmann, E.F. Schubert, *J. Appl. Phys.* **2003**, 94, 2627.
- [18] J.B. Fedison, T.P. Chow, H. Lu, I.B. Bhat, *Appl. Phys. Lett.* **1998**, 72, 2841.
- [19] P. Deb, H. Kim, Y. Qin, R. Lahiji, M. Oliver, R. Reifenberger, T. Sands, *Nano Lett.* **2006**, 6, 2893.
- [20] A. Patsha, S. Amirthapandian, R. Pandian, S. Bera, A. Bhattacharya, S. Dhara, *J. Phys. Chem. C* **2014**, 118, 24165.
- [21] M.A. Reshchikov, H. Morkoç, *J. Appl. Phys.* **2005**, 97, 061301.
- [22] C.Y. Nam, J.Y. Kim, J.E. Fischer, *Appl. Phys. Lett.* **2005**, 86, 193112.
- [23] S.M. Sze, *Physics of semiconductor devices*, New York: Wiley, **1981**.
- [24] L. Polenta, M. Rossi, A. Cavallini, R. Calarco, M. Marso, R. Meijers, T. Richter, T. Stoica, H. Luth, *ACS Nano* **2008**, 2, 287.

CHAPTER 7

BRIEF SUMMARY OF THESIS AND SCOPE FOR FUTURE WORK

The present thesis reports the effect of oxygen and Mg impurities on growth and physicochemical properties of nonpolar GaN NWs grown in APCVD technique. A brief, chapter wise summary of the thesis along with the scope for future study, is outlined as follows,

A brief literature review about the GaN NW growth, properties, applications, effect of different type of impurities in GaN and the challenging issues are outlined in the Chapter 1. The motivation and objective of the study on the effect of impurities on GaN NWs are briefed in this chapter.

The experimental techniques carried out for material synthesis and characterization are briefed in the Chapter 2, with basic principle of operation and the major components of the instruments. The in-house custom-built APCVD system developed in the present studies for GaN NW growth and *in situ* doping, can be further extended to grow the other III-nitride NWs with minor modification in the design of precursors delivery system.

Manipulation of surface architecture of semiconducting NWs with a control on surface polarity is one of the important objectives for NW based electronic and optoelectronic devices. In this context, the effect of unintentional incorporation of oxygen (O) on the growth, size and the surface morphology of nonpolar GaN NWs, with the possible mechanism involved, are studied in the Chapter 3. The study showed that the excessive incorporation of oxygen into the GaN during the NW synthesis could lead to the uncontrollable growth rate and inhomogeneous surface morphologies along with degradation in optical properties. By reducing the O concentration to background level, we could grow

the reproducible and size selective nonpolar wurtzite GaN NWs with uniform surface morphology and high optical quality. The results pave the way for the growth of GaN NWs in large scale, using a cost effective CVD growth technique.

Knowledge of the dopant incorporation and its pathways in NWs is highly demanding to have control over the dopant distribution in precise locations of the NW, which is limited by the growth methods. In this context, effect of Mg dopants (an intentional *p*-type impurity) at the liquid/solid interface (Au-Ga/GaN) in the axial growth of GaN NWs is studied in the Chapter 4. Morphological and structural studies showed the profound effects on Mg doped GaN NWs. This study also provides the direct evidence of incorporation of the Mg atoms through the Au-Ga/GaN interface. Local distortion and twining of atomic planes between catalyst particle and the NW confirm the interface as Mg incorporation pathway. Photoluminescence studies carried out on different concentrations of Mg doped GaN NWs confirm the activation of Mg atoms as *p*-type dopants in nonpolar GaN NWs. The growth methodology applied in the *in situ* Mg doping of GaN NWs can be further applied to dope the other III-nitride NWs in a controlled fashion. The Mg dopant distribution in GaN as well as other III-nitride NWs can be further probed with enhanced spatial resolution, using scanning probe techniques such as scanning photocurrent microscopy and scanning photo-voltage microscopy which are already proved to be the powerful tools for these studies.

The physicochemical processes at the surfaces of semiconductor nanostructures involved in electrochemical and sensing devices are strongly influenced by the presence of intrinsic or extrinsic defects. In this context, role of oxygen defect complexes, incorporated in nonpolar GaN NWs on methane (CH₄) sensing, is reported in the Chapter 5. The experiments and DFT based simulations of EELS studies are performed to understand the type of possible oxygen defects present in the impurity incorporated GaN NWs. The study shows possible presence of 2(O_N) and V_{Ga}-3O_N defect complexes in GaN NWs. The resistive gas sensor

devices made of GaN NWs with different oxygen impurity concentrations, showed the higher response toward CH₄ exposure by the device of O-rich NWs as compared to the response by device of O-reduced NWs. The possible mechanism of charge transfer process responsible for the gas sensing is studied locally on NWs, by *in situ* scanning Kelvin probe microscopy. A localized charge transfer process, involving V_{Ga}-3O_N defect complex in NWs is attributed to controlling the global gas sensing behavior of the oxygen rich GaN NW ensemble. The present results provide an insight for controlling the defects in III-nitride based NWs for advanced sensor device applications.

The functionalities of the GaN NW devices can further enhance by integrating them with other electronic and optoelectronic materials. In this context, ensemble and single Mg-doped nonpolar *p*-GaN NW/*n*-Si heterojunction devices are fabricated and their electrical and photodiode characteristics are compared in the Chapter 6. The defect states due to deep-levels and inhomogeneity in Mg dopants in *p*-GaN NWs resulted in the high ideality factor of ~10 for an ensemble *p*-GaN NW/*n*-Si device. Photovoltaic mode of ensemble NW device showed an improvement in the fill-factors up to 60 % over the single NW device with fill-factors up to 30 %. The observed enhanced (five orders) photoresponse of the single NW device over ensemble NW device confirms the photoconduction due to the presence of sub-bandgap states in *p*-GaN NW. The effect of impurity related defects on electrical properties can be further studied by fabricating field effect transistors.